UNIVERSITÀ DEGLI STUDI DI PARMA
FACOLTÀ DI SCIENZE MATEMATICHE, FISICHE E NATURALI
Dipartimento di Fisica

Disorder and frustration effects on the metal insulator transition in the $Y_{1-x}A_xBa_2Cu_3O_{6+y}$ system (A=Eu,Nd,Ca) from the clean to the dirty limit.

Francesco Coneri

Thesis submitted for the award of the degree of Ph.D. in Physics

Dottorato di ricerca in Fisica

Supervisors: Prof. Roberto De Renzi

Dott. Samuele Sanna

XXII Ciclo - Gennaio 2010

This document was typeset in Adobe® Utopia and Computer Modern Roman
by the author using the LaTeX2ε software.
The file in Portable Document Format was generated with pdfTeX version 13c.

Contents

List of Figures

Introduction

Copper perovskites give rise to one of the most surprising phenomena in solid state physics, that is the highest-temperature known superconductivity (up to 140 K) in a material on the verge of becoming an insulator. Since their discovery in 1986, they have attracted the attention of the scientific community both for the possibility of applications, and from the point of view of the fundamental physics. After 25 years the applications exist, although they are fewer than one hoped, and many properties have been clarified, including the non conventional origin of superconductivity. Nowadays cuprates are among the best known materials in condensed matter and yet the detailed nature of the high-T_c superconductivity is elusive.

The cuprate properties are determined by the electronic behaviour of the CuO_2 planes, characteristic of their structures. One of the distinctive features of these compounds is that it is possible to vary their properties by acting on their stoichiometry. Starting from an antiferromagnetic (AF) Mott-Hubbard insulating parent compound (T_N $\sim$400 K) it is possible to reach a high-T_c superconducting phase (T_c $\sim$100 K) in an almost continuous fashion. This is accomplished by doping charge carriers into the CuO_2 planes.

All cuprates show a long range AF phase in the parent compound. Their Néel temperature T_N is reduced upon doping, in a way that is dependent on the specific compound. When the Néel order is fully suppressed, a so called cluster spin glass phase (CSG) sets in, characterized by very low order temperatures (T_g <30 K) and short magnetic correlation length. The CSG phase gives way to the strongly correlated superconductor (SC), and these two orders coexist nanoscopically for a sizeable range of doping. The passage from the AF to the SC phase through the CSG corresponds to a metal to insulator transition (MIT), and understanding how doping and disorder influence this transition may help to unveil the high-T_c superconductivity mechanism. In particular in the literature disorder on the CuO_2 planes appears to have a strongly influence on the MIT, and on the CSG phase, whose nature is actually debated. Disorder on the CuO_2 planes can be varied by the controlled substitution of an adjacent cation with another of different valence and size, providing two independent parameter to control the MI transition: disorder by localized Coulomb impurities and random localized distortions.

In this work we decided to investigate extensively the low-doping range, starting from the undistorted clean limit case of $YBa_2Cu_3O_{6+y}$, where the charge doping on the CuO_2 layers is obtained by the introduction of oxygen atoms farther removed from such planes. Besides pure $YBa_2Cu_3O_{6+y}$ (Y100% in the following) we addressed other compositions. In particular two additional compositions were chosen to investigate the effect of small lattice distortions on the magnetic phase diagram by substitution of Y with a rare earth: $Y_{0.92}Eu_{0.08}Ba_2Cu_3O_{6+y}$ (Eu8%), yielding a very small mismatch of the cation radii, and $Y_{0.925}Nd_{0.075}Ba_2Cu_3O_{6+y}$ (Nd7.5%), yielding equivalent mismatch to that of the $Y_{0.95}Ca_{0.05}Ba_2Cu_3O_{6+y}$ (Ca5%) substitution.

We further chose to investigate increasing Ca compositions in the $Y_{1-x}Ca_xBa_2Cu_3O_{6+y}$ compound (x= 0.01, 0.05, 0.065, 0.08, 0.11, 0.14 and 0.18). Differently from the Y^{3+}-isovalent Eu and Nd substitutions, Ca^{2+} introduces a strong Coulomb disordered perturbation. For each Ca content (i.e. fixed disorder) we spanned several dopings by varying the oxygen content, therefore isolating the disorder from the doping effects.

We selected muon spin spectroscopy (μSR) as a local probe sensitive both to static magnetic order and to the presence of a flux-lattice in the superconducting state. This technique reveals a number of evident trends, showing that the isovalent substitution affects negligibly both the magnetic behavior and the MI transition, while Ca replacement has a marked influence on both the magnetic and superconductive behaviour, suggesting this influence to be specifically linked to the introduction of a charged impurity.
One of our main conclusions is that the low temperature magnetic order present for a wide range of doping, even in nanoscopic dispersion (coexistence) in the superconducting phase, is very different from the antiferromagnetic phase observed at high temperature and low doping. We call the first a quenched antiferromagnet (QAF) and the second a thermally activated antiferromagnet (TAAF). Our results indicate that whereas the quenched antiferromagnet can clearly coexist with the superconductor, the thermally activated antiferromagnet competes with the superconducting state around a hidden quantum critical point.

The thesis is structured as follows. Chapter 1 is introductory on the main properties of cuprates, more focused on the aspects that have been central to my experimental work. In particular I review the properties of the antiferromagnetic compound, both from an experimental and a theoretical point of view, and I introduce the concept of disorder, the key feature of this work. The following three chapters are devoted to the basics of the experimental techniques that I exploited in this work: x-ray diffraction, SQUID magnetometry and μSR (respectively in Ch. 2, Ch. 3 and Ch. 4). The experimental results are presented in Ch. 5; they include the sample production, their basic characterizations, and the main results of three groups of μSR experimental runs. In Ch. 6 the interpretation of the experimental result is presented.

Chapter 1

Cuprates

Cuprates represent the breakthrough of superconductivity from the low temperature physics to the high temperatures. The extraordinary superconducting properties of copper perovskites were first discovered in $La_{2-x}Sr_xCuO_4$, in 1986, by K. Alexander Müller and J. Georg Bednorz [1], who reported a record critical temperature of 38 K, nearly doubling the previous record T_c, in the metallic A15 $NbGe_3$ [2]. The discovery was soon followed by reports of larger transition temperatures in $YBa_2Cu_3O_{6+y}$, marking a huge jump in the time-line of superconducting critical temperatures (Fig. 1). The 1987 Nobel prize assigned to Bednorz and Müller is justified both by this jump and by the hopes of technological developments that it raised, and by the renewed interest to the unconventional properties that solids develop close to the metal-insulator transition. Up to date, cuprates show the highest T_c among several different superconducting materials which have been discovered in the last 25 years, such us many organic systems, new heavy fermions, MgB_2 and the latest Fe-based compounds.

In this chapter I will briefly sketch the main experimental features of these materials, focusing on the aspects that are central to my experimental work. In Sec. 1.1 I will describe cuprates from a structural and physico-chemical point of view; In Sec. 1.2 a phenomenological description of their phase diagram is outlined; In Sec. 1.3 the main properties of the antiferromagnetic compounds are reviewed; In Sec. 1.4 the concept of disorder is introduced; In Sec. 1.5 the basic phenomenology of type-II superconductors is outlined.

1.1 Copper perovskites and the doping mechanism

Cuprates are highly anisotropic, layered materials characterized by the presence of copper oxide CuO_2 planes. I show three typical examples of these materials in Fig. 2. From the left to the right $La_{2-x}Sr_xCuO_4$, $YBa_2Cu_3O_7$ and $TlBa_2Ca_2Cu_3O_{9+\delta}$ are characterized respectively by one, two, or three CuO_2 layers in the unit cell, and increasing optimal superconducting transition temperatures T_c=38, 92 and 123 K respectively. These three structures are

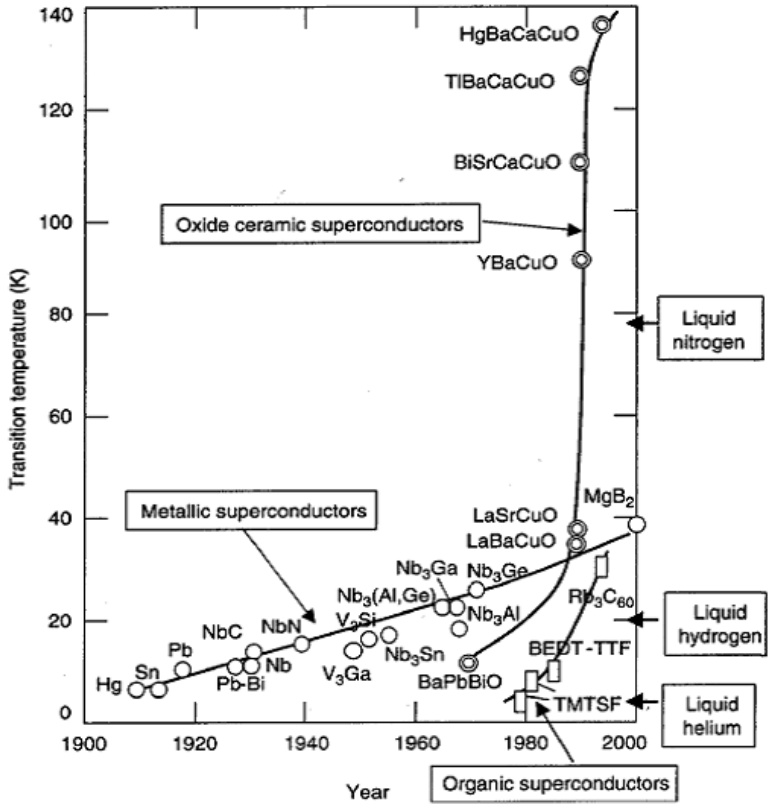

Figure 1: The evolution of the maximum T_c in the years and its huge jump in 1986.

derived from the basic cubic perovskite (prototype $CaTiO_3$), in which the di-valent Ca and tetravalent Ti occupy respectively the cube center and the vertexes, while O ions lie in the middle of each cube side. A defective $ACuO_3$ perovskite block may be recognized in all the three materials of Fig. 2. It features a trivalent A cation and a formally mixed valence Cu. The full cells are either tetragonal or orthorhombic and more complex than a cubic perovskite. The copper perovskite block is intercalated by other perovskitic, or, more generically, pseudo-cubic blocks.

Two key features characterize all these materials. The first is the formal mixed valence of Cu. The second is that the intercalated blocks, of ionic insulating nature, can be altered chemically either controlling their oxygen occupancy, or by substitutions of divalent with trivalent cations. The resulting charge unbalance is (partially) transferred to the CuO_2 layer, exploiting the mixed Cu valence. This is actually a naive picture, since Cu^{3+} does not exist in these compounds and the extra hole is partially shared by neighbor oxygens. The charge transfer provides a doping mechanism, that controls a metal-insulator transition in the copper oxide subsystem.

In the following I shall concentrate on the $YBa_2Cu_3O_{6+y}$ structure, synthesized for the

first time in 1987 [4, 5]. It is composed of three perovskite blocks stacked along the c axis; Fig. 3 shows more details of the $YBa_2Cu_3O_{6+y}$ cell. Here the different ions are labeled with subscripts, but, to avoid confusion with stoichiometry, in the following we retain the label-in-parenthesis scheme. The compound displayed on the left, $YBa_2Cu_3O_6$, is the so-called parent compound. There are two inequivalent Cu ions in this structure. One is identified as

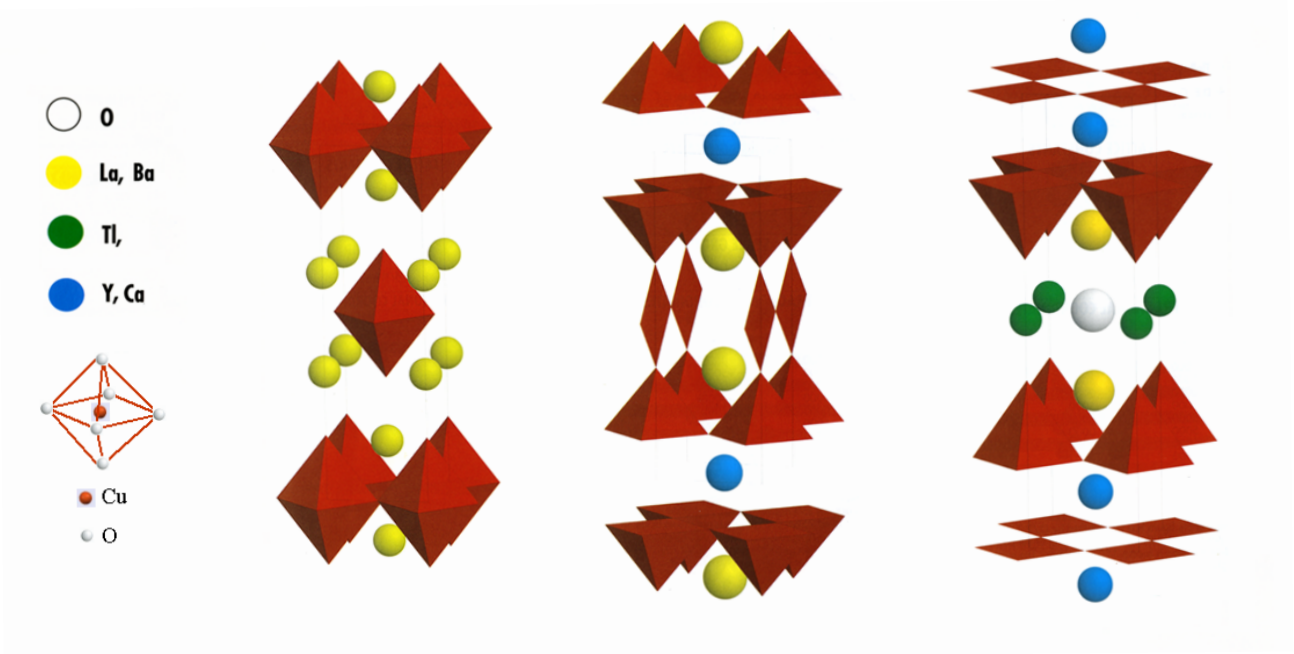

Figure 2: From left to the right: $La_{2-x}CuO_4$, $YBa_2Cu_3O_7$ and $TlBa_2Ca_2Cu_3O_{9+\delta}$. The legend on the left includes an explicit view of a Cu atom and its coordination in a dumb-bell [3].

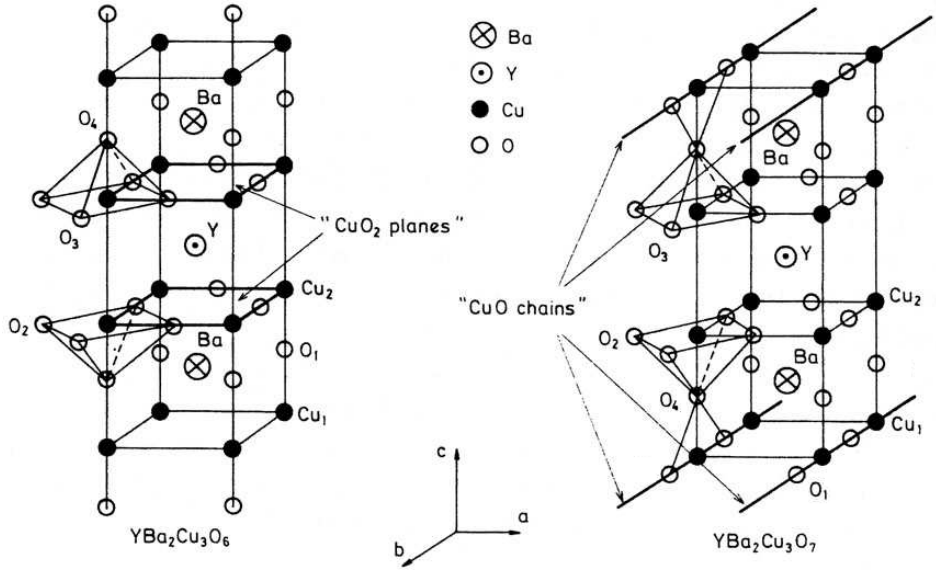

Figure 3: Tetragonal (left) **T** insulating compound $YBa_2Cu_3O_6$ and orthorombic **O** (right) $YBa_2Cu_3O_7$. The **T**$\rightarrow$ **O** structural transition takes place for $y \sim 0.3$.

Cu(1), and it appears in the top and bottom layers, which are totally oxygen-defective. The second, identified as Cu(2), appears in the central defective $YCuO_3$ block (also the Y layer is missing its oxygens). Cu(2) defines a bi-layer of squares, of CuO_2 composition.

The structure may be viewed as a defective $YCuO_3$ central block surrounded by two defective $BaCuO_3$ basal blocks. In this parent compound additional oxygen ions easily occupy the defective basal sites. These sites are however occupied preferentially along one of the two tethragonally equivalent directions, giving rise to the formation of Cu(1)O(1) chains, and to a tetragonal to orthorhombic transition at $y = 0.3$. These chains are fully formed in the ideal $YBa_2Cu_3O_7$ compound, shown on the right of Fig. 3. Actually the optimal superconductor is obtained for $y = 0.92$.

The Cu(2) site is coordinated with five oxygen: two O(2) ions, two O(3) ions and one O(4), in a square based pyramidal configuration with apex on the O(4) site; the Cu(2)O(4) bond distance is always greater than that with the coplanar oxygens.
Actually the O(2) and O(3) sites are not perfectly coplanar with the Cu(2); this determines a buckling of the CuO_2 planes, which changes slightly when replacing the Y atom with a trivalent rare earth (R=Eu, Er, Gd, Nd, et cetera). as it is characteristic of transition metal oxides [6] this isovalent modification does not alter the main electronic features of the cuprate phase diagram, which are dominantly determined by charge doping. Subtler effects may arise because mismatching of bond lengths along the a and b lattice directions, among the (Y,RE), Ba and Cu layers.

It should be noted that oxygen addition does not produce charge transfer at first, since Cu(1) is monovalent in the parent compound and the formation of an isolated Cu(1)-O-Cu(1) dimer provides a perfect charge balance according to:

$$2\mathrm{Cu(1)}^{+} + \mathrm{O} \rightarrow 2\mathrm{Cu(1)}^{2+} + \mathrm{O}^{2-}. \tag{1}$$

Formation of chains longer that this, i.e. more than one cell unit, are required to provide a net charge transfer to the Cu(2) block.

1.2 The phase diagram of cuprates

Figure 4 shows the typical features of the cuprates phase diagram, where the transition temperatures are presented as a function of the hole content h. Let me start with discussing the characteristics common to all families of cuprates. Starting from the left, at $h = 0$, the so called parent compound is an antiferromagnetic (AF) insulator, however in a naive picture this material should be a metal. As a matter of fact, considering the square plaquette shown in Fig. 5b, one Cu^{+2} per cell corresponds to a $3d^9$ configuration. The presence of a hole per cell should give rise to a metallic state. Actually the parent compound is a strongly

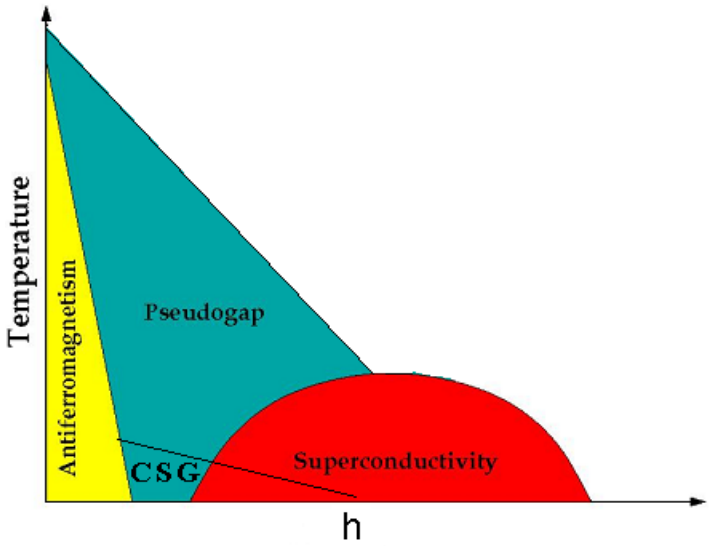

Figure 4: A sketch reflecting the most relevant features of a cuprate phase diagram. The antiferromagnetic, cluster spin glass, superconducting and pseudo-gap temperatures behaviour are described in the tex.

correlated system, where a gap is opened by the Hubbard mechanism: the on-site repulsion between electrons makes double occupancy energetically unfavourable, the ground state has antiferromagnetic spin structure, and plain hole hopping can happen only up to nearest neighbours, as schematically shown in Fig. 5c.
This is a half-filled Mott-Hubbard insulator of the charge transfer [7] type, in the sense that the energy of the Lower Hubbard Band (LHB) falls below the doubly occupied O_{2p} levels. This implies that the lowest energy excited states involve a hole on the O_{2p} level instead of in the LHB. Therefore doping will similarly populate these states. The peculiar hole wave function, mostly delocalized on the four O(2) and O(3) around a given Cu(2), is called Zhang-Rice singlet [8].

The parent cuprates are prototypes of the two-dimensional Heisenberg antiferromagnet (2DHAF), i.e. isotropic exchange is very strong in the plane of the plaquettes, and extremely weak between different layers. Actually the bilayer cuprates like YBCO (and a fortiori trilayer compounds) have a strong intra-bilayer exchange, but their bi-dimensionality is not affected. I will discuss further details of the magnetic properties in the next section.

Doping the compound as described in the previous section determines an abrupt reduction of the Néel temperature T_N, followed by the appearance of a metallic behaviour, which is accompanied by the onset of non conventional superconductivity. The transition temperatures describe a dome with a maximum that ranges from 38 K in $La_{2-x}Sr_xCuO_4$ to 140 K in Hg based compounds, well above BCS limits. The optimal T_c corresponds to a hole density $h = 0.16$. The $h < 0.16$ and $h > 0.16$ ranges are conventionally called underdoped and

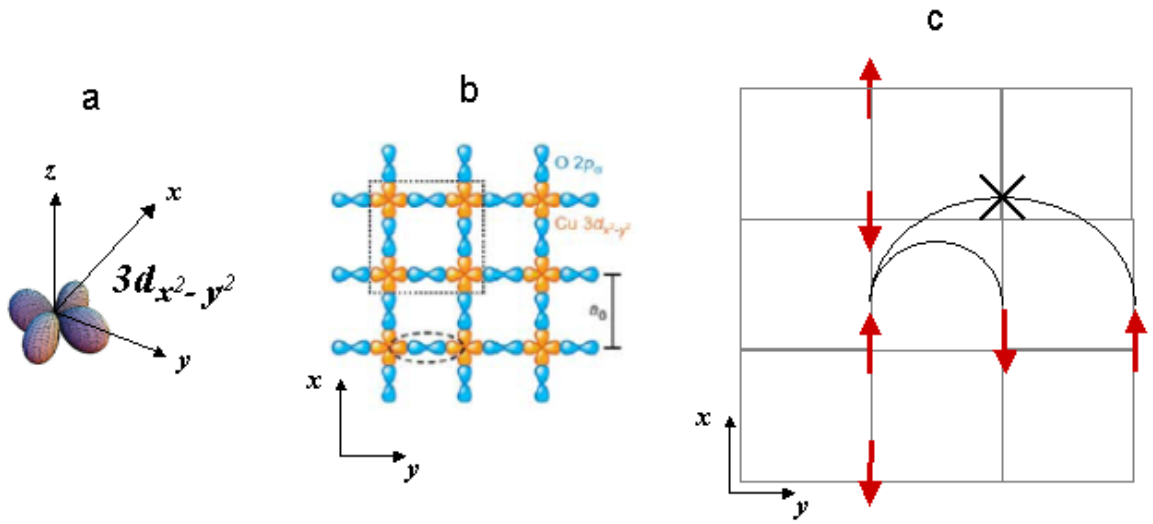

Figure 5: a: The Cu $3d_{x^2-y^2}$ orbital responsible for the electronic behaviour of the CuO_2 plaquettes. b: In the plaquettes the super-exchange interaction between Cu is mediated by the O_{2p} orbitals. c: In AF phase double occupancy (first neighbour hopping) is possible, but energetically unfavourable; the second neighbour hopping is avoided by the exclusion principle.

overdoped regions, respectively.

In the strongly overdoped region the effect of electronic correlation should decrease, approaching the conditions of normal Fermi liquids. In the opposite underdoped regime the effects of correlation dominate. Here phonons alone cannot mediate the superconducting pairing, and excitations of magnetic nature are the possible alternative candidates for the mechanism of high-T_c superconductivity.

A picture that is often discussed invokes the competition between two different ground states, each associated with a specific order parameter or energy scale. An example of this kind is the Fermi liquid competing with the characteristic order parameter of the insulating phase [6]. In this example doping controls the competition by suppressing one order parameter and then favouring the second one. A quantum critical point (QCP) is predicted when the characteristic energy scale of both states are suppressed, and quantum fluctuations dominate at low temperatures, since no energy gap exists. These fluctuations could replace phonons in the mechanism of superconductivity, justifying the dome shape as the border of a region where they dominate, centered at the QCP.

The prevailing opinion is that the competing order parameter characterizing the undoped-to-light-doped phase cannot be the AF one, since it disappears long before optimal doping in many compounds. In Ch. 5 and 6 I will show evidence of the presence of a different QCP, around the suppression of AF order. Experimentally another energy scale has been detected by several spectroscopies (ARPES, NMR, Raman, tunnelling, etc. [9] and references therein) between zero and optimal doping. This energy scale corresponds to a (pseudo)gap

Δ_p, anisotropic in **k**-space, larger than the superconducting one, and with different symmetry (it is maximum in the **k** directions where the latter has nodes). The pseudogap line in Fig. 4 represents Δ_p/k_B, that is the temperature below which the excitation spectrum measured by the above mentioned techniques is depleted.

The exact nature of the pseudogap state is elusive, and still debated. Candidates are represented by charge or spin density waves (CDW/SDW), or even more exotic orbitally ordered states, where the anisotropic Cu orbitals are differently oriented, in a periodic pattern, at crystallographically equivalent lattice sites. A peculiar version of coupled CDW and SDW is represented by the so called stripes, where antiferromagnetic Cu spins are separated by periodically spaced domain walls, to which the holes segregate (Fig. 8a). These were predicted by Emery and Kievelson [10], and observed by Tranquada [11] in a particular compound ($La_{1.6-x}Nd_{0.4}Sr_xCuO_4$, with $x = 1/8$) by neutron diffraction. Since these stripes cannot be directly associated with the pseudogap (too low ordering temperatures and linked only to specific compositions), many authors speculate whether dynamic fluctuations of this order may play a role. No conclusive evidence has been provided until now.

Figure 4 actually shows a schematic diagram reflecting the $La_{2-x}Sr_xCuO_4$ behaviour (see left panel in Fig. 6), where the suppression of T_N and the onset of T_c are separated by a sizeable doping range, corresponding to a low temperature magnetic state. This state differs from the pure Néel order, and has been identified in the past as an unconventional spin glass, often called cluster spin glass (CSG). The main motivation for this identification lies in the low transition temperatures of order 10 K (much less than $T_N \approx 400$ K). Our data dispute the glassiness of this state.

In a recent paper our group showed [12] that the CSG h range is much narrower, if not absent, in $YBa_2Cu_3O_{6+y}$ (see right panel in Fig. 6). This and other μSR works [13, 14] further demonstrated that low temperature magnetism and superconductivity coexist in the extreme underdoped regime, both in $YBa_2Cu_3O_{6+y}$ and in $La_{2-x}Sr_xCuO_4$. This coexistence takes place in a sizeable range of doping, much larger than the uncertainty due to chemical inhomogeneity. Furthermore all muons detect, in separate experiments, both internal AF fields and diamagnetism: this demonstrates that the two order parameters coexist at least nanoscopically (mean distance between AF and SC domains of the order of 2 nm), if not at the atomic level.

In the rest of this chapter I shall limit myself to the cuprate families stemming from the two parents La_2CuO_4 and $YBa_2Cu_3O_6$. The most relevant difference between $YBa_2Cu_3O_{6+y}$ and $La_{2-x}Sr_xCuO_4$ is therefore the presence of a window of pure CSG phase, as evident by comparing the two panels in Fig. 6. Many authors relate the developing of this low temperature magnetic state with intrinsic disorder, via frustration effects. In fact Y-

$Ba_2Cu_3O_{6+y}$, where the charge reservoir is farther removed from the CuO_2 layer, represents the closest physical system to the clean limit, i.e. the pure, idealized undistorted periodic lattice [12, 15, 16, 17, 18]. On the contrary randomly placed divalent cations provide the doping mechanism in $La_{2-x}Sr_xCuO_4$ and in $Y_{1-x}Ca_xBa_2Cu_3O_6$. The heterovalent substitution $Sr^{+2} \rightarrow La^{3+}$ and $Ca^{+2} \rightarrow Y^{3+}$ takes place in the cation planes, nearest neighbours to the ones of the magnetic and/or superconducting CuO_2. This places $La_{2-x}Sr_xCuO_4$ and $Y_{1-x}Ca_xBa_2Cu_3O_6$ in the dirty limit case, where disorder, increasing with doping, actively modifies the scenario [16, 17]. This aspect will be better clarified in Sec. 1.4.

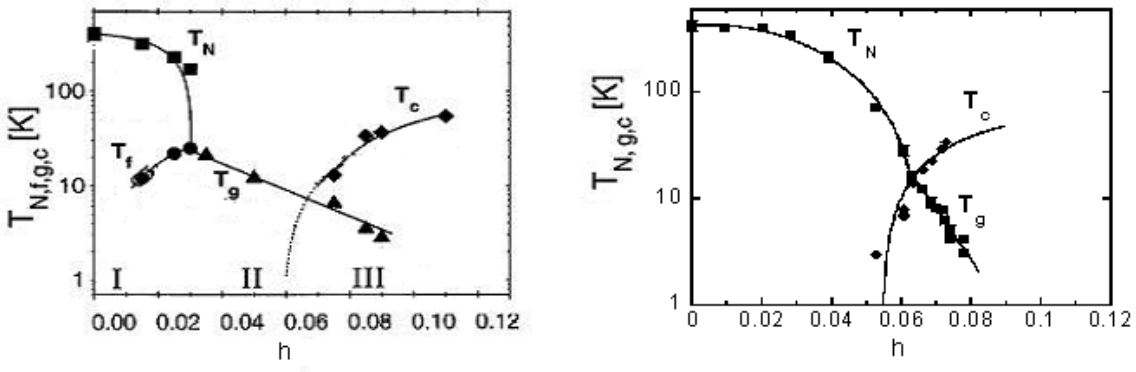

Figure 6: Left: $La_{2-x}Sr_xCuO_4$ phase diagram, where a window of pure CSG phase is present for a sizeable doping range (adapted from [19]). Right: in $YBa_2Cu_3O_{6+y}$ the solely CSG window is absent (adapted from [12]).

1.3 The 2DHAF and its behaviour upon light doping

The cuprate parent compounds are half-filled Mott-Hubbard insulator of the charge transfer [7] type. Their observed transitions are $T_N = 310, 420$ K for La_2CuO_4 and $YBa_2Cu_3O_6$ respectively, but very large in-plane correlation lengths [20] persist far above T_N. Neutron scattering experiments [20] determine a very large isotropic antiferromagnetic (AF) exchange $J < 0$ along the in-plane bonds, with a much reduced coupling J' along the c axis. This is quite typical of quasi-2D systems, such as the fluorite perovskites [21], prototypical examples of localized spin systems. The cubic system with the same J along all three directions (3D) would be rather large ($T_{N0} \approx 1500$ K), whereas in the ideal 2D isotropic (Heisenberg) antiferromagnets the Mermin-Wagner theorem [22] predicts $T_N = 0$. Deviations from the ideal case produce finite temperature order, scaling roughly as $1/\log(A/J)$. In $YBa_2Cu_3O_6$ $A = J'$ is the residual inter-bilayer interaction and in $La_{2-x}Sr_xCuO_4$ $A = J_x - J_y$ is the in-plane anisotropy, since in this case J' vanishes by symmetry, due to the $(a/2\, a/2)$ shift between consecutive CuO_2 layers.

The high temperature behaviour is described by the 2D Heisenberg model, where the exchange interaction can be calculated from the Hubbard model at half-filling in the t-J approach. The ideal 2D behaviour is still a good description below T_N with its large quantum spin

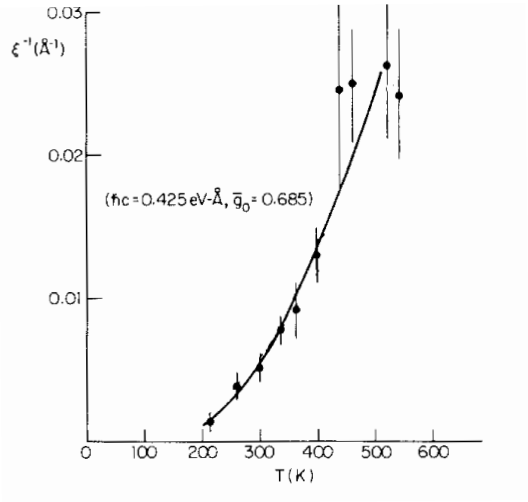

Figure 7: Agreement between NLσM and the inverse correlation length detected by neutrons above T_N, as a function of temperature. The $LaCuO_4$ sample is characterized by a $T_N \approx 200$ K. (Adapted from [23]).

reduction for $S = 1/2$, $\mu = 0.6\,\mu_B$ [24]. The high temperature correlations are quantitatively described [23] in the non linear sigma model (NLσM) long-wavelength approximation. The coupling constant g places cuprates in the renormalized classical regime, i.e. with a Néel state at $T = 0$, as opposed to the quantum disordered regime, where fluctuations kill the order parameter even at zero temperature. It successfully provided a description of the finite correlation lengths detected by neutron scattering [25] above the transition to three dimensional (3D) order. In Fig. 7 the agreement between the NLσM calculation and the correlation length detected by neutrons [20] in a $LaCuO_4$ single crystal is shown.
Departing from half-filling, i.e. doping the parent compound with a holes density h, the measured magnetic transition $T_N(h)$ drops rapidly, until the CSG phase, characterized by an onset temperature T_g, is established. The qualitative understanding of the magnetic hole-doped ground state is that holes localize on oxygen at low temperature, leading to a local spin singlet [8] (i.e. neutralizing a Cu spin), but their dynamical effect reduces the ordering temperature T_N rather more effectively than a mere magnetic site dilution. The abrupt reduction of the ordering temperature T_N is then the effect of a magnetic frustration [26]. Experimentally it has been detected very early on by implanted muons [27], and it corresponds also to a drop of the static magnetic moment [20, 28, 29] at $Q = \left(\frac{1}{2}\,\frac{1}{2}\right)$.

The strong frustrating effect of doped holes in the 2DHAF background may be understood in several ways. As mentioned in the previous section, stripes have been predicted, [10]

detected [11] in specific doping and distortive conditions ($La_{1.6-x}Nd_{0.4}Sr_xCuO_4$ x=0.12), and are possibly present also as correlated fluctuations. In fact a qualitative argument to reconcile stripes with reduced order temperatures is to consider that they lead to the formation of finite size domains [30]. Figure 8a shows their static version.

In addition alternative disordered spin spiral states have been predicted [31,32], and their hole density dependence reproduces the incommensurate magnetic scattering [33] detected in $La_{2-x}Sr_xCuO_4$. This description considers that at low temperature ($T < 100$) K and at doping $p < 0.055$, each hole is trapped in a hydrogen-like bound state close to the Sr ion, and delocalized over several Cu plaquettes. Under these assumptions [34] the local distortion of the spin fabric is shown in Fig. 8b and c, where the small arrows represent staggered Cu spins $\mathbf{n}$, i.e. the real spin direction alternates from one site to the next. The static spin distortion decays as $1/r$ at large distances. A finite concentration of Sr-hole bound states gives a ground state shown in Fig. 8d. It is worth to stress that the outlined models leads only to partial, qualitative agreement with experimental data.

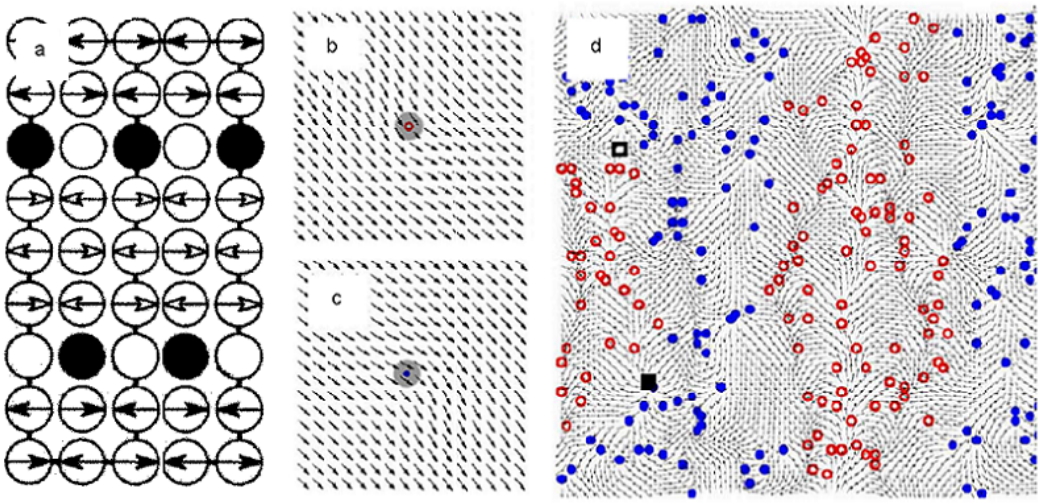

Figure 8: a: The stripe pattern of $La_{1.6-x}Nd_{0.4}Sr_xCuO_4$ with x=0.12. Arrows indicate the orientation of magnetic moments on the metal atoms. Holes (filled circles) are located at the anti-phase domain boundaries. (Adapted from [11]). b and c: The local distortion of the fabric of the staggered spin $\mathbf{n}$. Shaded areas corresponds to the hole localization regions. d: A particular random realization of Sr positions in $La_{2-x}Sr_xCuO_4$ with concentration $x = 0.05$ (Adapted from [32]).

1.3.1 Reentrance

A peculiar feature of the AF low doping region is the crossover between two thermal regimes, identified by the re-entrant behaviour of the magnetic moment in $La_{2-x}Sr_xCuO_4$, $YBa_2Cu_3O_{6+y}$ and $Y_{1-x}Ca_yBa_2Cu_3O_6$. ^{139}La Nuclear Quadrupole Resonance (NQR) [30] and

muons experiments [12,19,35,30,36,37] identify a thermally activated regime where the static moment is strongly reduced proportionally to holes density, and a re-entrant regime where the moment recovers a nearly holes-independent zero temperature value. Two examples from different techniques are reported in Fig. 9. In the left panel the the splitting of the quadrupole frequency ν_Q, which is a measure of the static effective local magnetic field at the La site, shows an upturn for low temperatures ($T < 30$ K) in $La_{2-x}Sr_xCuO_4$. In the right panel the muon spin precession frequency, determined by the staggered internal magnetic moments acting at the muon site (see Sec. 5.5.1) has an analogous upturn in $Y_{1-x}Ca_xBa_2Cu_3O_6$. In both cases the low temperature behaviour looks like a crossover. The crossover temperatures qualitatively agree with the onset of spin dynamics freezing, detected e.g. by Cu NQR [38] and muons, [19,35] but also with the activation temperatures of the variable range hopping regime in transport [15, 39, 40]. Neutrons observe a decreasing static moment at $(\frac{1}{2}\,\frac{1}{2}\,l)$ in the re-entrant state, associated with an increase of the rod $(\frac{1}{2}\,\frac{1}{2}\,q)$ *elastic* intensity [20] that matches the muon moment recovery. It is worth stressing that in these conditions it is improper to consider only the moment deduced from the Bragg peak intensity at $(\frac{1}{2}\,\frac{1}{2})$, as if a simple Néel state were present. Partial and full sum rules [41] are hard to implement and imply very large errorbars, whereas local probes offer a more direct, almost model independent way of determining the full static moment.

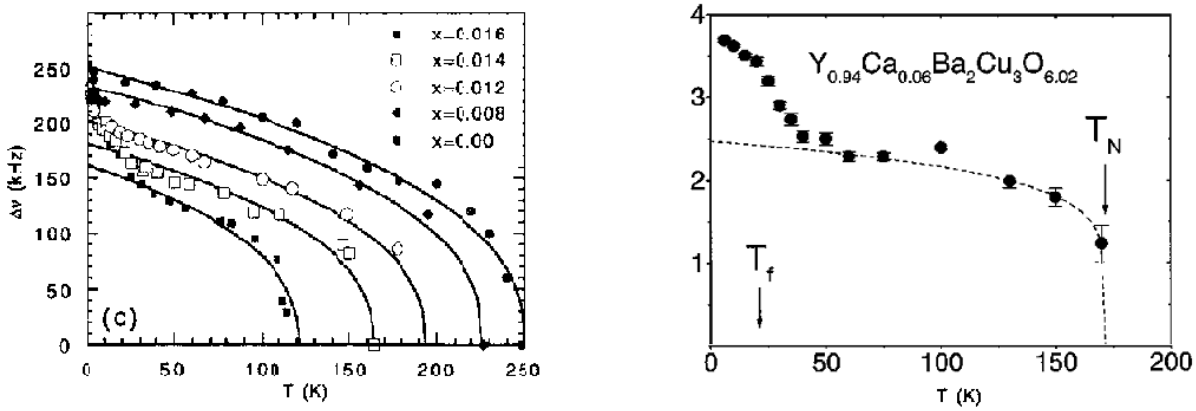

Figure 9: Low temperature re-entrant magnetic regimes as seen by NQR [42] in $La_{2-x}Sr_xCuO_4$ (left) and by μSR [19] in $Y_{1-x}Ca_xBa_2Cu_3O_6$ (right). (Adapted from [43] and [19]).

For increasing h, the CSG phase is the close precursor of the metal insulator transition, giving rise to the superconducting (SC) phase at a critical density h_s. It is a precursor both in the trivial sense that it lies in between the AF and the SC phases, and because increasing the temperature at any small finite density h leads to metallic transport properties [15].

The glassy nature of the CSG state [44] is however controversial, since magnetic structure coexists with disorder [33,45] and the observed features [43,46] are not exclusive of a true spin glass state. We simply acknowledge that increasing hole density, hence frustration, leads to a

more disordered state, whose experimental signature is the abrupt flattening of the magnetic transition dependence on hole density, i.e. $dT_g/dh \ll dT_N/dh$.

All cuprates share these main features, with the addition of intrinsic inhomogeneities around the MI transition, evidenced as the presence of static magnetism [12,14,19,30,36,42] at low temperatures, well inside the superconducting phase.

1.4 From the clean to the dirty limit

Besides all the commonalities described in the previous sections, remarkable differences are experimentally detected among the cuprates. I focus here on a few relevant points, (the values in parentheses refer to the two parents La_2CuO_4 and $YBa_2Cu_3O_6$ in this order, unless otherwise specified):

i) Distinct T_N;
ii) Distinct critical densities for the suppression of T_N ($h_c \approx 0.02, 0.06$);
iii) A region of pure CSG behaviour, without superconductivity, sizeable [26] in $La_{2-x}Sr_x$-CuO_4, almost vanishing in $YBa_2Cu_3O_{6+y}$;
iv) Distinct critical densities for the onset of the superconducting T_c ($h_s \approx 0.05, 0.06$); these two values are rather close to each other, but clearly different, [32] as it is confirmed also by Ca doping in $YBa_2Cu_3O_{6+y}$, leading to $h_s = 0.075$ for 8% Ca, (see [47] and Sec. 5.5.2).

These main points originate from the strong influence of the disordered heterovalent substituents (Sr^{2+}, Ca^{2+}), which intrinsically place $La_{2-x}Sr_xCuO_4$ at the dirty limit (disorder and doping are intrinsically linked each other), differently form the clean $YBa_2Cu_3O_{6+y}$ [16,17], as already pointed out in Sec. 1.2.

The influence of disorder on metal-insulator phase transitions is a classical topic in condensed matter, dating back to the work of P. W. Anderson and Sir Neville Mott, that granted them the 1977 Nobel prize for Physics. A vast review on transition metal oxide [6] provides the general framework, although high temperature superconductivity in cuprates is rather unique. Heuristic models were recently proposed [16, 17], showing that the phase diagram is indeed influenced by disorder and that phase coexistence appears in certain conditions. The introduction of disorder and of a phenomenological local parameter linking it to the free energy of the superconducting and magnetic phases produces the phase diagrams of Fig. 10 were, in qualitative agreement with experiments they display AF, disordered, or SC regions, as well as regions where two order parameters coexist (phase separation). They also show that the phase diagram is strongly influenced by this simple phenomenological parameter, hence an accurate experimental determination of the diagram may help to clarify the nature

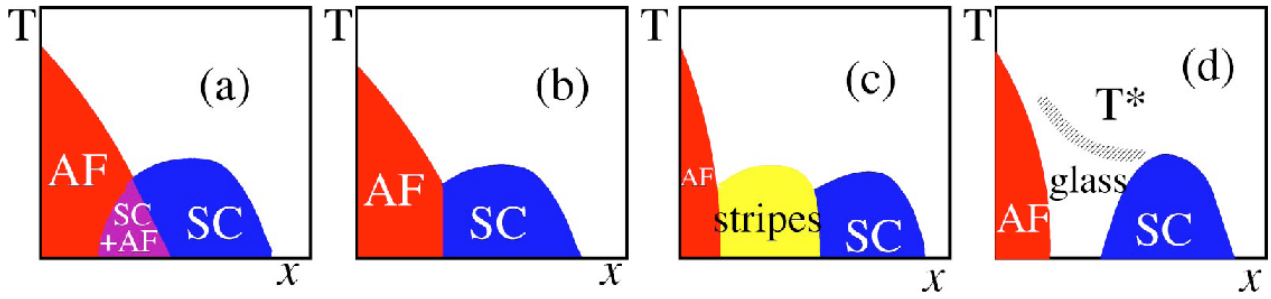

Figure 10: Schematic representation of the obtained phase diagrams in the clean (a,b,and c) and dirty (d) limits. The main point is that the CSG phase exists only in presence of quenched disorder. (Adapted from [17]).

of high temperature superconductivity. A qualitative experimental phase diagram was also drawn by Rullier-Albenque *et al.* [48] and it was discussed in a recent review [18] on disorder at metal-insulator transitions. Their figure is replicated in Fig. 11. The main problem lies in the calibration of the disorder axis, which is here just a guess. As better clarified in Sec. 1.6, the work of my thesis can be summarized exactly as the attempt to quantify this axis and thus gain important insight on the cuprates at the metal-insulator transition.

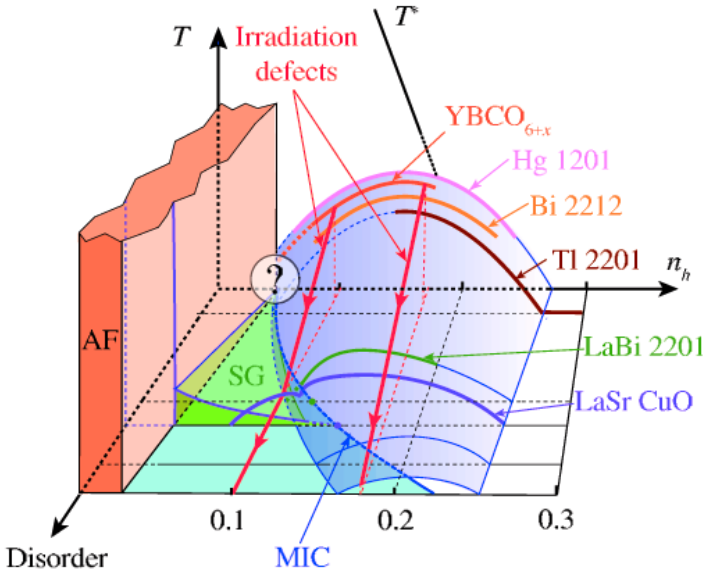

Figure 11: The phase diagram proposed by Rullier-Albenque *et al.* [48]. The disorder axis seems to contribute to the appearance of a glassy window (SG).

1.5 Extreme type II superconductors

In this short section I intend to discuss the strong type-II character of cuprates, therefore I briefly recall the meaning of the London penetration depth λ_L and of the the coherence length ξ, that determine such a character.

The coherence length ξ is the direct consequence of the macroscopic quantum nature of the superconducting state. It represents the length over which the order parameter $\psi(\mathbf{r})$ describing the superconducting state varies, for instance when a boundary to a normal metal appears (superconducting-normal junction). Therefore it can be viewed as the characteristic length of the wave function associated to a Cooper pair or, simplistically, as the mean distance between two charge carriers of a pair. In BCS theory the following relation is found [49]:

$$\xi_0 \sim \frac{\hbar v_F}{k_B T_c}, \tag{2}$$

where v_F is the Fermi velocity, k_B the Boltzmann constant and T_c the critical temperature. For a typical metal $v_F \sim 10^6$ m/s. For $T_c \sim 10$ K this means $\xi \sim 1800$ Å.

The London penetration depth λ_L is the length inside a superconductor across which the value of an applied field is reduced, because of the Meissner effect, by a factor $1/e$. It is given by

$$\lambda_L^2 = \frac{m^*}{\mu_0 e^2 n_s}, \tag{3}$$

where μ_0 is the free space permeability, e is the electron charge, n_s is the supercarrier density, and m^* is the electron effective mass. It actually corresponds to the depth of the flowing currents that shield the external field.

The Ginzburg-Landau parameter $\kappa = \lambda/\xi$ is of great importance in the thermodynamical calculation of the free energy of a superconductor. If $\kappa < 1/\sqrt{2}$ an applied field is entirely expelled from the superconductor (type-I), while if $\kappa > 1/\sqrt{2}$ the minimum condition for the free energy corresponds to the penetration of the field in the superconducting volume (type-II). In this case the penetration takes place in the form of fluxoids, forming the so called Abrikosov flux-lattice. An example is shown in Fig. 12, where it is imaged in $NbSe_2$ by a low temperature scanning-tunnelling microscope. The spatial field distribution in this regime will be analyzed in Sec. 4.3 (see Figs. 39 and 40).

Cuprates are non BCS extreme type-II superconductors, characterized by very short coherence length, as extracted by upper critical field measurements (and estimations). Moreover

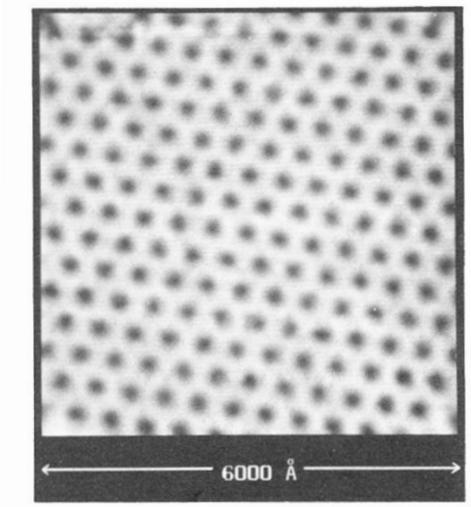

Figure 12: The Abrikosov flux lattice produced by 1T magnetic field in $NbSe_2$ at 1.8 K, imaged by a low temperature scanning-tunnelling microscope [50].

their large anisotropy results in tensorial expressions for λ_L and ξ, as opposed to standard metals. In $YBa_2Cu_3O_{6+y}$ $\xi_c(0) \sim 4\,\text{Å}$, and $\xi_{ab}(0) \sim 15\,\text{Å}$. The former is practically equal to the spacing between adjacent conducting CuO_2 planes, which indicates a two dimensional nature also for superconductivity. Here I list the indicative values of these parameters for three of the most studied compounds, $La_{2-x}Sr_xCuO_4$, $YBa_2Cu_3O_6$ and $Bi_2Sr_2Ca_2Cu_3O_{10}$.

Compound	T_c	$\lambda_{ab}(\mathring{A})$	$\lambda_c(\mathring{A})$	$\xi_{ab}(\mathring{A})$	$\xi_c(\mathring{A})$	$B_{c2}^{ab}(T)$	$B_{c2}^{c}(T)$
$La_{1.96}Sr_{0.04}CuO_4$	38	800	4000	35	7	80	15
$YBa_2Cu_3O_{6+y}$	92	1500	6000	15	4	150	40
$Bi_2Sr_2Ca_2Cu_3O_{10}$	110	2000	10000	13	2	250	30

Table 1: Indicative values for the London penetration depth λ_i, coherence length ξ_i, and upper citical field B_{c2}^i for three High-T_c oxides (i=ab or c). (From [49]).

A *linear sistematic dependence* between the zero temperature extrapolation of the muon relaxation rate $\sigma(T \to 0)$ and the critical temperature T_c is observed in all cuprate compounds [51,52], and is shown in Fig. 13, where the Uemura plot [53] of many compounds is reported. The muon relaxation rate σ is proportional to the width ΔB of the inhomogeneous internal magnetic field, and consequently to $1/\lambda_L^2$ when $T < T_c$ (see Sec. 4.2.4, 4.3, and in particular Eq. 49). The following relation holds:

$$\sigma \propto 1/\lambda_L^2 = \frac{\mu_0 e^2 n_s}{m^*}. \tag{4}$$

Equation 4 and the experimental data of Fig. 13 define an energy scale for the superconductivity that is proportional to the quantity n_s/m^*.

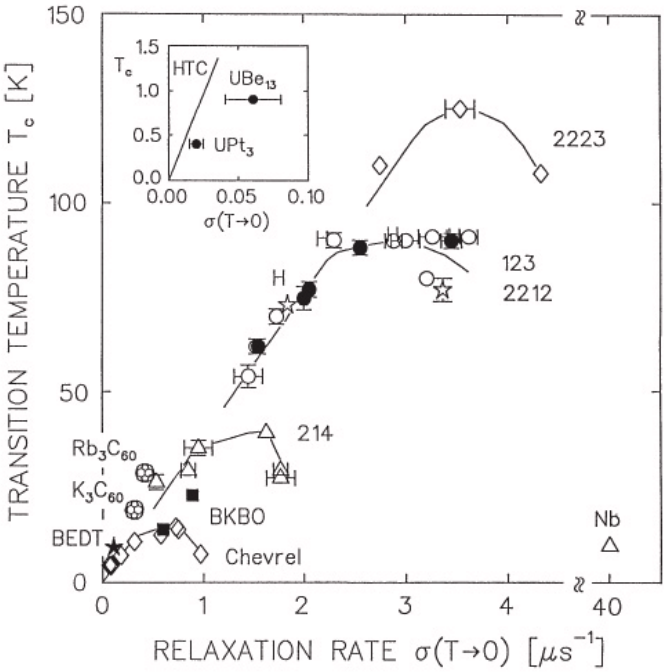

Figure 13: The so called Uemura plot. The relation between T_c and $\sigma(T \rightarrow 0)$ is linear in the underdoped region, and slope is common to most of the cuprates. With further carrier doping T_c shows a saturation around the optimum doping region (i.e. the maximum T_c for a given compound), followed by a suppression in the weakly overdoped region [52].

1.6 Methodology and main purposes of this work

In order to gain understanding of the correlation between disorder and doping with the electronic behaviour at the metal insulator transition (see Sec. 1.4), we decided to extensively investigate the low-doping range, starting from the clean limit case, disentangling the effect of these two control parameters.

Figure 14 provides the variance of the cationic radii, a measure of the mismatch introduced by the substituents as a function of doping. For the generic compound $Y_{1-x}A_xBa_2Cu_3O_{6+y}$ this quantity is simply calculated by the formula $\sigma^2 = (1-x)R_Y^2 + xR_A^2 - \langle R_M \rangle^2$, where $R_{Y,A}$ is the radius of each cationic species and $R_M = (1-x)R_Y + xR_A$ is the average cationic radius of the compound. The oblique red line highlights the already stressed intrinsic association between disorder and doping in the $La_{2-x}Sr_xCuO_4$ compound. The blue line represents the pure $YBa_2Cu_3O_6$ (Y100% in the following) clean compound (i.e. variance = 0, small residual charge disorder). All the other horizontal lines represent disorder values that are doping independent.

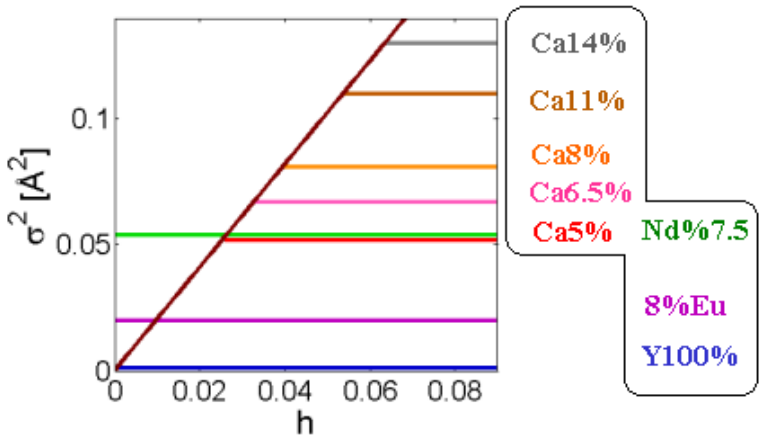

Figure 14: Cationic radiii variance as a function of doping. The effects of disorder and doping are disentangled.

Chemical Formula	Label
$YBa_2Cu_3O_{6+y}$	Y100%
$Y_{0.92}Eu_{0.08}Ba_2Cu_3O_{6+y}$	Eu8%
$Y_{0.925}Nd_{0.075}Ba_2Cu_3O_{6+y}$	Nd7.5%
$Y_{0.99}Ca_{0.01}Ba_2Cu_3O_{6+y}$	Ca1%
$Y_{0.95}Ca_{0.05}Ba_2Cu_3O_{6+y}$	Ca5%
$Y_{0.935}Ca_{0.065}Ba_2Cu_3O_{6+y}$	Ca6.5%
$Y_{0.92}Ca_{0.08}Ba_2Cu_3O_{6+y}$	Ca8%
$Y_{0.89}Ca_{0.11}Ba_2Cu_3O_{6+y}$	Ca11%
$Y_{0.86}Ca_{0.14}Ba_2Cu_3O_{6+y}$	Ca14%
$Y_{1-z}Eu_zBa_2Cu_3O_{6.35}$	Eu35%
(z=0, 0.2, 0.4, 0.5, 0.6, 0.7, 0.85, 1)	

Table 2: Chemical formulas of the synthesized samples and relative labels. The oxygen range is $0 \leq y \leq 0.5$.

Besides Y100% we chose two additional compositions, to investigate the effect of small lattice distortion on the magnetic phase diagram by substitution of Y with a rare earth. We chose $Y_{0.92}Eu_{0.08}Ba_2Cu_3O_{6+y}$ (Eu8%), yielding a very small mismatch of the cation radii, and $Y_{0.925}Nd_{0.075}Ba_2Cu_3O_{6+y}$ (Nd7.5%), yielding equivalent mismatch to that of the heterovalent $Y_{0.95}Ca_{0.05}Ba_2Cu_3O_{6+y}$ (Ca5%) substitution. It will be shown that isovalent substitution affects negligibly both the magnetic behaviour and the MI transition.

We further chose to investigate increasing Ca compositions that introduces a strong

Coulomb disordered perturbation. For each Ca content (i.e. fixed disorder) we spanned several dopings by varying the oxygen content.

Many complementary techniques have been exploited to study the synthesized compounds. X-ray diffraction and neutron scattering for structural analysis, resistivity and thermopower for transport, iodometric titration for chemistry, SQUID magnetometry and μSR for magnetism and superconductivity. As it is clarified in Ch. 5 I have been directly involved only in some of them.

I gather up in the previous table all the stoichiometries we studied, together with the sample labels. The samples with variable Eu content z are only marginally included in this thesis and are the subject of a separate study that will be presented elsewhere.

Chapter 2

X-rays and diffraction techniques

X-rays were discovered by Wilhelm Röntgen in 1895, for which he was awarded the first Nobel Prize in Physics in 1901. Successively in 1911 Bragg and von Laue suggested the x-rays to be the natural probe to analyze the crystal structures, being their wavelengths comparable with the interatomic spacing in crystals, and in the following years they provided the crystallographic description of NaCl and some other simple compounds starting from the analysis of their x-rays patterns; therefore they posed the main bases for crystallography about one hundred years ago.
In the following I will focus on the use of x-ray diffraction in solid state physics, that is a widespread tool that provides the identification of crystalline compounds by their diffraction patterns. After a brief recalling of some theoretical basics of x-ray diffraction in Secs. 2.1 and 2.2, some aspects linked on the standard laboratory equipment will be presented in Sec. 2.3. In Sec. 2.4 I concentrate on some practical aspects related to the diffraction from polycrystalline materials, that is the technique exploited in the present work.

2.1 X-ray diffraction

When we perform a diffraction experiment we are primarily interested with determining the unit cell parameters, the nuclei positions and the electron distribution inside the cell, thus with solving the crystal structure; this is often accomplished by the x-ray powder diffraction. Let us now point out a couple of essential features of the x radiation ($10\,\text{nm} < \lambda < 1\,\text{pm}$). First of all its wavelengths are comparable with the interatomic spacing of crystals $\sim 1\mathring{A}$. Since the energy of an electromagnetic radiation with $\lambda \sim 1\mathring{A}$ is

$$\lambda(\mathring{A}) = \frac{12.4}{E(keV)}; \tag{5}$$

of order 10 keV, it can be commonly obtained by striking a metallic target with high energy electrons; the inelastic excitations of the core electrons of the target provide the required

energy for the photons.
When the atoms of the crystal are exposed to a coherent and monochromatic electromagnetic radiation the two main effects are the Thomson scattering and the Compton scattering. The former process is elastic and is responsible for the diffraction phenomenon, because the elastic condition grants a simple kinematic relation between emission angles and the set of crystalline planes coherently contributing to the scattering. The Compton scattering inelastically contributes to the process; the incident beam looses part of its energy during the interaction with the electrons, and contributes to the incoherent scattering.

The Laue calculation for the amplitude of the elastically diffused wave from a regular and periodic arrangement of scattering units (physically the lattice) is a standard argument that can be found in many textbooks [54, 55, 56, 57]. It is rather interesting to note how the monochromatic diffraction could be treated geometrically like reflection. L. Bragg and his father W.H. Bragg gave a simple interpretation of the coherent diffraction by a crystal [58]. Let us consider a series of parallel planes of a crystal lattice identified by the Miller indexes (h, k, l), being d the interlayer spacing, and being each plane only partially reflecting the incoming radiation. Under the hypothesis of symmetrical reflection, the difference in optical path for beams reflected by adjacent planes is $2d_{(h,k,l)} \sin\theta$, according to Fig. 15. The interference of the radiation reflected by each plane is constructive every time the difference in optical path equals a full value of wavelengths λ, thus the diffraction condition is simply

$$2d_{(h,k,l)} \sin\theta = n\lambda, \tag{6}$$

where θ is the diffraction angle and n is an integer. This means that only for some θ the reflections arising from a set of parallel planes will sum with the same phase and will contribute to an intense reflected (diffracted) beam. The position of the diffraction peaks and the d-spacings that they represent provide informations about the distances between lattice planes in the crystal structure; each peak measures a d-spacing that represents a family of

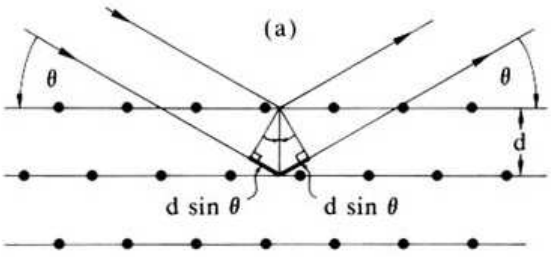

Figure 15: Graphical visualization of the Bragg's calculation for interference: d is the interlayer spacing between two adjacent planes of a set of parallel planes, θ is the diffraction angle. The difference in optical path is equal to $2d_{(h,k,l)} \sin\theta$ and is underlined in figure by thick segments; when this quantity is equal to a full number of wavelength the interference of the reflected beams is constructive.

lattice planes identified by the Miller indexes (h, k, l). Even if Eq. 6 does not take into account the relative intensity in the diffraction pattern, it reproduces the Laue results.

2.2 Scattering processes causing X-ray diffraction

Let us now briefly analyze how the intensity of the diffraction peaks and its variation is related to the chemical species and their arrangement in the crystal structure; this step is essential to fully define the diffraction process from a crystal.

2.2.1 Scattering by an electron

In diffraction we are concerned with coherent scattering, where each atom that is struck by radiation becomes a secondary point source of x-rays with the same wavelength of the incident beam, and holds a well defined phase relation with the incident radiation. The intensity of the outcoming radiation was calculated by J.J. Thompson in 1906 [55]

$$I(r) = \frac{I_0}{r^2}\left[\frac{e^2}{m_e c^2}\right]^2 \frac{1 + cos^2(2\theta)}{2}, \tag{7}$$

where r is the distance from the oscillating electron, I_0 is the intensity of the incident beam, e is the electron charge, m_e is its mass, c the speed of light and θ measures the angle between the outcoming and incoming wave vectors. The factor $(1 + cos^2 2\theta)/2$ is called polarization factor because it reflects the fact that an incoming non polarized incident beam is partially polarized by the scattering process (the moving particle radiates most strongly in a direction perpendicular to its motion and the radiation will be polarized along the direction of its motion). As a consequence the intensity of the diffuse radiation is maximum along the incident wave vector and minimum in the orthogonal direction.

2.2.2 Scattering by an atom (atomic factor)

The electronic distribution inside an atom contributes to the intensities of the diffraction peaks via the so called atomic form factor. The scattering by an atom is the result of the interference among waves generated by single electron scattering processes inside one atom. To take into account this interference effect one can write the total amplitude of waves scattered by one atom in the form

$$f_0 = \int_{dV} n(\mathbf{r}) exp(-i\mathbf{r}\cdot\mathbf{q})\mathrm{d}V, \tag{8}$$

where $\mathbf{r}$ is the internal coordinate of the atom, $\mathbf{q} = \mathbf{k}'$ - $\mathbf{k}$ is the difference between the diffused and incident wave vector, $n(\mathbf{r})$ is the charge density and the integration takes place

over the electron distribution around the atom. Mathematically it is the Fourier Transform of the density of the scattering object $n(\mathbf{r})$, from the real to $\mathbf{q}$-space. Its calculation yields a constant characteristic of each chemical element. These constants are compiled in the International Tables for Crystallography ($Vol.3$), *pp.* (201-207).

2.2.3 Scattering by an unit cell (structure factor)

Equation 6 provides all the reflections (h, k, l) associated to a given crystal lattice. Hence the atomic arrangement inside an unit cell is the other parameter affecting the relative intensities of the diffracted peaks. The contribution to the total amplitude of a scattered wave at the position $\mathbf{R}$ inside the crystal can be written as usual as

$$\mathbf{A} = \sum_{\mathbf{R}} exp(-i\mathbf{R} \cdot \mathbf{q}). \tag{9}$$

If we consider an unit cell containing s atoms which coordinates inside the cell are $\mathbf{r}_j = \alpha_j\mathbf{a} + \beta_j\mathbf{b} + \gamma_j\mathbf{c}$ we can replace the coordinate $\mathbf{R}$ with $\mathbf{R} + \mathbf{r_j}$ in the previous equation obtaining

$$\mathbf{A} = \sum_{\mathbf{R}} exp(-i\mathbf{R} \cdot \mathbf{q}) \cdot \sum_{j} f_j \, exp(-i\mathbf{r}_j \cdot \mathbf{q}).; \tag{10}$$

where we introduce the atomic form factor for the j-th atom f_j and define the second term as the geometric structure factor $\mathbf{S}$. Introducing the Bragg condition $\mathbf{q} = \mathbf{G}(hkl)$ we have

$$\mathbf{S}_{(hkl)}^{(\alpha_j\beta_j\gamma_j)} = \sum_{j} f_j \, exp(-i\mathbf{r}_j \cdot \mathbf{G}) = \sum_{j} f_j \, exp\left[-i2\pi(\alpha_j h + \beta_j k + \gamma_j l)\right]. \tag{11}$$

This quantity has to be computed for each atom j and for each reflection (hkl).

2.2.4 Scattering in presence of thermal motion

In a real crystal, atoms lying in their crystallographic positions are not fixed, but the thermal excitations make them moving around their equilibrium point that corresponds to the minimum of their potential energy. This give rise to modifications of the intensity of the scattered waves through the so called Debye-Waller factor.

Let us suppose that the coordinate of an atom at finite temperature could be expressed by the relation $\mathbf{R}(t) = \mathbf{R}_0 + \mathbf{u}(t)$, being the fluctuations of each atom not related to the others. It is very simple to show [54] that the intensity of the Bragg peaks will be approximately reduced by a factor proportional to the quadratic average shift of the atom from its equilibrium position following the relation

$$I = I_0 exp\left[-\frac{1}{3} < u^2 > q^2\right], \tag{12}$$

where I_0 is the intensity diffused by the rigid lattice and the exponential factor, known as the Debye-Waller factor, is the thermal reduction. The average potential energy $<U>$ of an harmonic oscillator is related to the absolute temperature and to the quadratic average shift by the equation

$$< U >= \frac{1}{2}k_B T = \frac{1}{2}C < u^2 >, \tag{13}$$

where C is the spring constant. This relation allows to write Eq. 12 as

$$I(hkl) = I_0 exp\left[-\frac{k_B T}{3C}q^2\right] \tag{14}$$

with (hkl) indexes of the vector $\mathbf{q} = h\mathbf{A} + k\mathbf{B} + l\mathbf{C}$. This result is a good approximation at high temperatures, when the atomic oscillations are randomly distributed, thus not correlated; for low temperatures a quantum calculation involving phonons is needed. Equation 14 shows that the intensity of the diffracted peak is weakly depressed by increasing temperature, and that a reflection with small q is less influenced than an higher one.

Taking into account all the factors affecting the relative intensity diffractions produced by a lattice plane of a crystal structure it is possible to calculate a theoretical diffraction pattern for virtually any crystalline material. The ICDD (International Center for Diffraction Data) database contains over 70.000 patterns which calculations have been based on these factors, and the ICSD (Inorganic Crystal Structure Database) includes the calculated patterns and all of the detailed crystal structure data used as a base for pattern refinements done on experimental data.

2.3 X-ray conventional generators

Conventional x-rays diffractometers have moderate dimension, so they are quite suitable as a standard laboratory equipment. Leaving out the non conventional generators (syncrotrons), in this section will be briefly analyzed the generation and the selection of the radiation, and an overview of the most common detectors is presented. Further specific informations can be found in many books (see for example [59, 60, 61]).

2.3.1 X-rays generation

Striking a pure anode of a particular metal with high energy electrons in a sealed vacuum tube generates x-rays that may be used for diffraction. They are conventionally produced by sealed tubes or rotating-anode generators, both based on the same process; a schematic of a sealed tube is shown in Fig. 16. Referring to this figure, in the sealed tube electrons are emitted by a cathode, which is a hot filament maintained at high potential difference

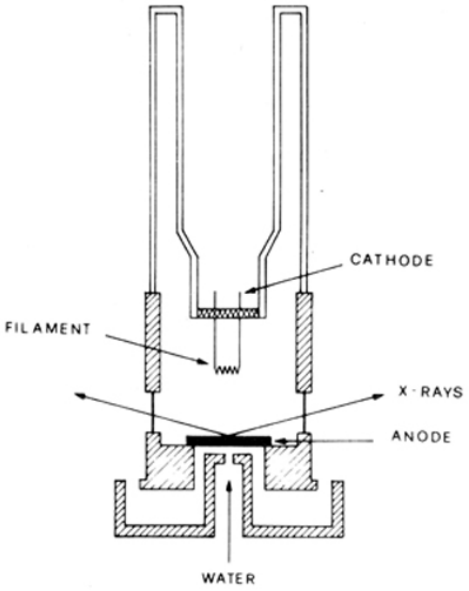

Figure 16: Schematic representation of a sealed tube generator. The electrons emitted by the filament are abruptly accelerated by a potential of some kV; they strike the anode and produce the spectrum of Fig. 17. The tube is under high vacuum to preserve the x-rays emission efficiency. The exiting arrows represent the outcoming x-rays that passes not altered through a thin Be slab.

(typically 30 or 40 KeV) with respect to the anode. The electronics is usually designed so that the anode is grounded and the cathode is at high negative potential, so that the generated electrons are strongly accelerated toward the anode, which consists of a metallic target usually cooled by water. Once they strike the anode they are quickly decelerated and give rise to the brehmstrahlung, but if their kinetic energy is high enough they can also ionize the atoms of the target and induce electronic transitions of the inner shells, thus generating a characteristic spectrum (Fig. 17). This process requires high vacuum inside the tube, otherwise electrons are strongly absorbed. The x-rays emitted by the anode reach the focusing optics and then the sample, through a very thin beryllium window; beryllium is a very toxic element, but due to its small atomic number it is almost transparent to x-rays.

The broad spectrum in the left panel of Fig. 17 depends on the potential applied between the electrodes. The much more intense characteristic lines are named K,L,M... and correspond to the electronic transitions from higher energy orbitals to respectively n=1,2,3... shells; α, β... label the starting L,M....state, while 1,2,3...label the different orbitals involved in the transition. Selection rules exclude some of them; in the right panel of Fig. 17 the first 5 permitted transitions $K\alpha_i$ and $K\beta_j$ are shown as a blow up of the left panel.

Depending on the wavelengths that we want to select we can use different metals for the anode (target); the wavelength of the strongest Cu radiation ($K\alpha$) is approximately 1.54 $\mathring{A}$, while for the same $K\alpha$ transition is about 2.29 $\mathring{A}$ for Cr, 1.94 $\mathring{A}$ for Fe, 1.79 $\mathring{A}$ for Co, 0.71

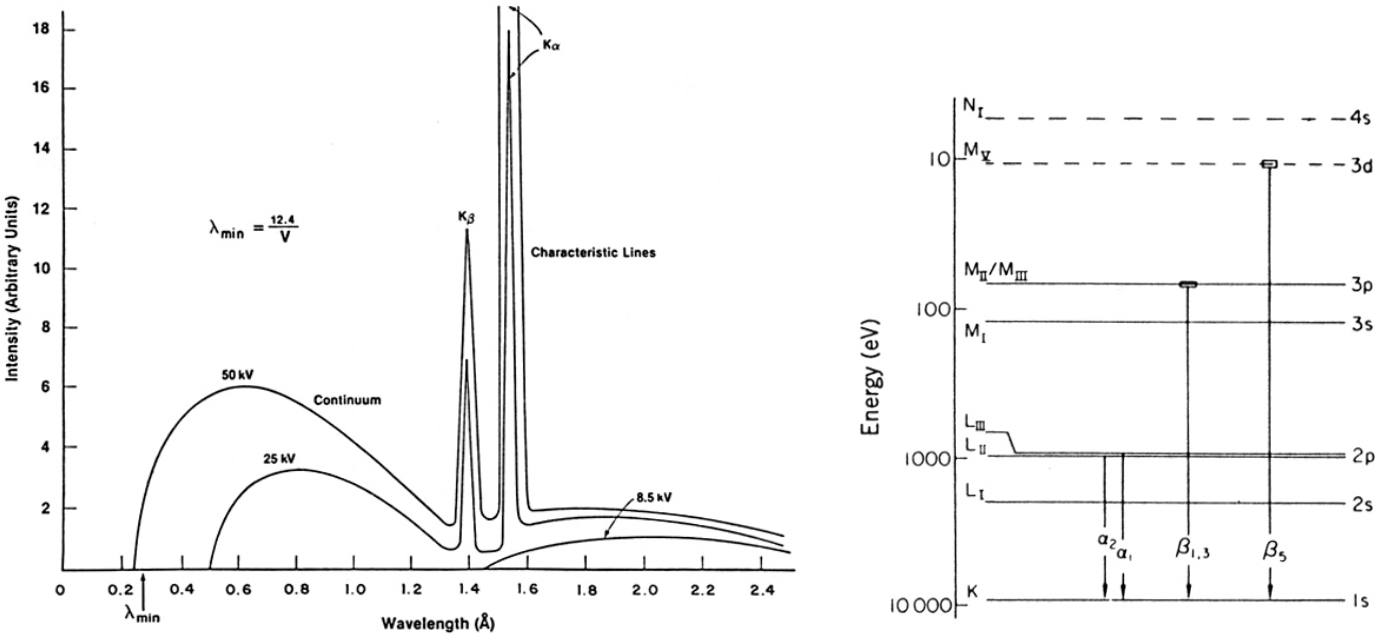

Figure 17: Continuous and characteristic radiation for copper (leftpanel) and electronic transitions that give rise to the various emission lines (right panel). From the left panel it is evident that the accelerating potential should be included between 25 and 50 KV in order to obtain an enhancement of the characteristic part of the radiation. The values of the indexes $i = 1, 2$ and $j = 1, 2, 3$ are not resolved on this scale (note the logarithmic scale in the right panel).

$\mathring{A}$ for Mo. The frequency of this emission is described by the well known Moosley's law

$$\nu = C(Z - \sigma)^2, \tag{15}$$

where, C and σ are constants and Z is the atomic number of the atomic species undergoing the emission. The intensity of a characteristic K line is described by the equation

$$I_K = Bi(V - V_K)^{1.5}, \tag{16}$$

where B is a constant, i is the electron current, V the working potential and V_K the excitation potential of the K series, strictly related to the ionization energy of the atom. By defining I_B as the total brehmstrahlung intensity, it is possible to show that the highest value for the ratio I_K/I_B is reached when $V = 4V_K$; for copper $V_K = 8.981KV$, thus the best choice for the potential of a Cu X-ray generator is about $40V_K$.
The choice of the type of radiation is dictated to avoid frequencies strongly absorbed by undesired atoms sometimes present in the specimen.

2.3.2 Making monochromatic X-rays

Monochromatic radiation is required to match the Bragg condition, thus the characteristic emission must be filtered by means of an absorption filter, a crystal monochromator, a

wavelength-selective detector or a combination of these devices.
There is no effective way to remove the K_{α_2} peak from the spectrum. Sometimes software corrections (digital filtering) are available; they are based on the knowledge of the angular dispersion of the $K_{\alpha_{1,2}}$ doublet (which increases with increasing angle), and on its intensity relationship.
Exploiting the strong non linearity of the photoelectric absorption is it possible to set up a β filter; essentially one needs to find an element with an absorption edge that lies between the characteristic K_α and K_β wavelengths. The latter radiation will be greatly attenuated, even if a significant amount of the high energy portion of the continuous spectrum will be transmitted.
The most common way to filter the radiation in a diffractometer is by use of a crystal monochromator. Each component wavelength of a polychromatic beam directed on a single crystal of known orientation and d-spacing will be diffracted at a specific angle, following the Bragg's law; thus by choosing a single crystal with the right d spacing it is possible to cut off all the undesired wavelengths. Pyrolitic graphite curved crystals are the most suitable, being sufficiently mechanically strong to withstand large deformations during the x-ray exposition; their bending permits to both monochromatize and focus the incident beam. The mosaicity of the crystal must be very low, in order to minimize the dispersions of the beam.

2.3.3 X-rays detection

Different kinds of detectors are nowadays available. In principle an ideal detector should provide good spatial and energy resolution and should cover a large area in order to capture as many x-rays as possible. In practice, detectors are optimized for one of these qualities. Proportional, scintillation, and PSD (Position Sensitive) detectors are extensively utilized in crystallography .
A proportional detector provides an output voltage which is proportional to the energy of the x-ray photon; it consists of a gas characterized by a high cross-section for x-rays, sealed in a tube in the presence of two electrodes under and applied voltage. The incoming x-ray strikes the atoms of the gas, producing photoionization electrons. The electrons are accelerated by the voltage and, after an avalanche process, a current proportional to the number of initial electrons (thus to the energy of the incident photon) is produced, hence a voltage drop across a resistance is measured. This kind of detector is usually characterized by an high energy resolution.
A scintillation detector exploits the luminescence of certain materials (scintillators) when they are struck by ionizing radiation. It converts the energy deposited by the x-rays into light, usually in the near ultraviolet or blue region of the visible spectrum. The scintillator is coupled to a light sensor such as a photomultiplier where a photocathode absorbs the light

of the scintillator and emits a cascade of dynodes electrons by the photoelectric effect. The subsequent multiplication of the photoelectrons results in a final electrical pulse which can then be measured. This kind of detector have a good counting efficiency.
A relatively new class of detectors is represented by the Position Sensitive Detectors (PSD); these provide not only the number of counting, but also the spatial position of the single event. The early versions were formed by an array of proportional counters able to subtend an angle of $\sim 10°$; now two dimensional detectors are available as well. Of course, the main advantage of a PSD is the improvement in the acquisition rate; on the other hand they generally show a lower resolution compared to a point detector.

2.4 X-ray diffraction from polycrystalline materials

It is now worth to have a quick overview on some practical aspects related to our work. The most exploited experimental setup in powder diffraction are the Deby-Sherrer camera [62] and the Bragg-Brentano configuration. In the following section I shall describe the latter, being the geometrical setup of our instrument. In Sec. 2.4.2 I show the porpouse of our analysis; Sec. 2.4.3 is devoted to a presentation of the GSAS suite, and Sec. 2.4.4 is a very introducing overview on the *Rietveld method*, the basis of any quantitative analysis of diffraction patterns.

2.4.1 The Bragg-Brentano configuration

The Bragg-Brentano geometry [63] exploits a Seemann-Bohlin parafocusing arrangement, improving the intensity and resolution of the diffraction maxima. A Seemann-Bohlin ar-

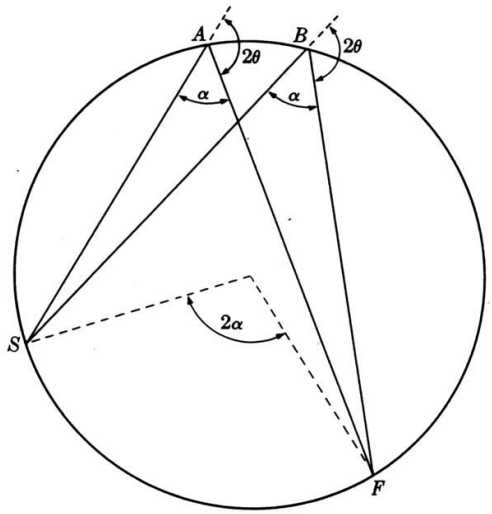

Figure 18: Seemann-Bohlin focusing geometry. The focusing circle is the geometrical locus where the reflections from all the planes of different (hkl) are focused. In the figure only one (hkl) reflection is shown (Adapted from [56]).

rangement is shown in Fig. 18; it is based on the following geometrical theorem: all angles inscribed in a circle based on the same arc SF (S is the source, F is the focusing point) are equal to each other and equal to half the angle subtended at the center by the same arc. Suppose that x-rays proceeding in the directions SA and SB encounter a powder specimen located on the arc AB, thus defocusing on the sample. Then the x-ray diffracted by the (hkl) planes at points A and B will be deviated through the same angle 2θ=180°- α, which means that the diffracted rays must proceed along AF and BF, and come to a focus at F where a detector will be placed. The circle defined by points A, B, S (and F) is the focusing circle. In practice diffracted rays originating from an extended region of the specimen all converge to one focusing point. It is possible to take advantage of this focusing action by using a flat specimen in the Bragg-Brentano geometry, as shown in Fig. 19. In this geometry the detector moves at different angles about the sample keeping a constant distance equal to the radius of the diffractometer circle, thus is necessary to ensure that the parafocusing effect is also produced at a constant distance form the sample. Being the radius of the focusing circle dependent on the incidence angle of the incoming radiation, the focusing condition is held by moving by $\Delta\theta$ the specimen and by $2\Delta\theta$ the detector D, thanks to a mechanical coupling. Because of this motion the normal to the specimen's surface will bisect the incoming and diffracted beams and the radius of the focusing circle decreases with increasing θ, keeping F always located on the detector D that now lies at the intersection between the diffractometer circle with the focusing circle.

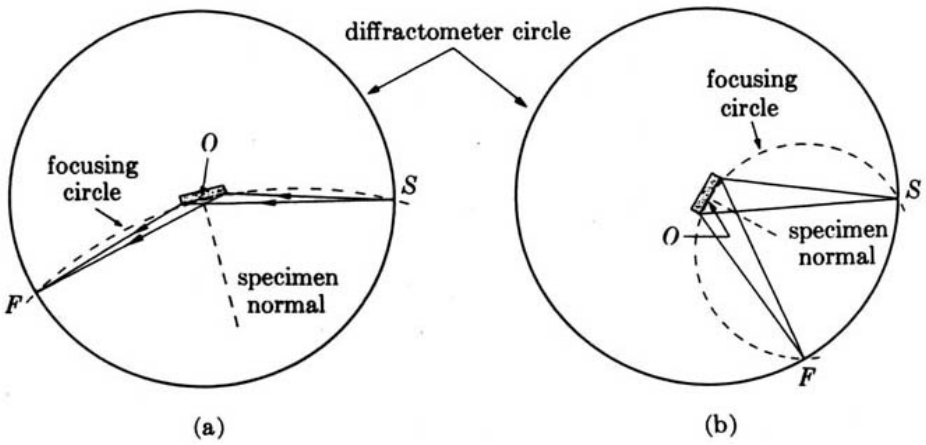

Figure 19: Bragg-Brentano focusing geometry for a flat specimen. The focusing circle is drawn by a dashed line; the focusing condition is preserved only if the detector and the sample (or alternatively the detector and the x-ray source) rotate together by the angles $\Delta\theta$ and $2\Delta\theta$. (Adapted from [57]).

2.4.2 Our application of powder diffraction

Here I show the task I accomplished by collecting x-ray diffraction patterns. The first has been a *qualitative* aim of the analysis, to roughly check the phase purity of the materials during the various synthesis steps (see Sec.5.1). In our case the structure of the compound is supposed to be well known. A crystallographic information file (.cif) provides to the software all the required structural items; this file is based on the informations collected in the International Tables for Crystallography.
Based on the Rietveld method, the *quantitative* refinement of the structure has been systematically performed on the compounds after the last synthesis step. Even if the resolution of our measurements did not permit some fine evaluations such as the atomic position and occupation, by the full profile analysis it has been possible to extract the lattice parameters and to relate theme to the oxygen content and to the holes density on the CuO_2 planes, as explained in Sec. 5.2.

The x-ray diffraction patterns have been collected at the Chemistry Department of our university. The instrument utilized is a Philips PW1050 powder diffractometer in Bragg-Brentano θ-2θ vertical configuration. The HT-PW1830-generator works at 40 kV and 25 mA, and the radiation exploited is Cu-K_α. The PW3011 Xe-gas proportional detector has an efficiency of 93% for the mantioned radiation, and the PW3020 vertical goniometer is separately driven in θ-2θ by two step-motors ($\pm 0.0001°$). A good compromise between the measuring time and signal to noise ratio has been found for $\Delta\theta$=0.03°, τ=5 sec and a total excursion $20° < 2\theta < 80°$.

2.4.3 Software utility: GSAS/EXPGUI

The fit of the powder diffraction patterns were carried on thanks to the *General Structure Analysis System* (*GSAS*) suite, created by Allen C. Larson and Robert B. Von Dreele of Los Alamos National Laboratory (LANL) in 1985. It is a set of programs for the processing and analysis of both single crystal and powder diffraction data obtained with x-rays or neutrons; it is possible to fit data either from constant wavelength (CW) or from time-of-flight and energy dispersive x-ray experiments. Up to 99 different datasets can be used in combination, and for a single sample a maximum of 9 crystallographic phases can be refined. Other than phase identification, GSAS is also used for texture analysis, lattice constant determination and simulation of powder diffraction data; it is a powerful and free program package, easily downloadable from the web [64], and available for a series of operating systems (Windows, Unix, Macintosh, VMS).
GSAS is organized in several (about 50) main programs each designed for specific types of

tasks or types of crystallographic calculations. The data input is done through EXPEDT, an interactive editor based on several levels of shell dialog; even if it is still possible to enter each shell, from 2001 the data input became more user friendly thanks to the introduction of a General User Interface (GUI) called EXPGUI by its compiler, Bryan H. Toby of NIST (National Institute of Standards and Technology). The GSAS/EXPGUI routine needs an input consisting in two files: the data, in gsa format, and an ascii instrumental file. The former can be simply obtained by converting the raw data by the use of many freely available conversion routines, while the latter concerns the starting values of parameters characteristic of the instrument, and for commercial instruments is supplied by the seller.

2.4.4 Rietveld refinement

The Rietveld method was proposed by Hugo Rietveld in two seminal papers in 1967 [65] and 1969 [66]. It optimizes user-selected parameters to minimize the difference between an experimental pattern, that is the observed data, and a model (containing the parameters) based on the hypothesized crystal structure and instrumental parameters, that is the calculated pattern. A structure model that makes physical and chemical sense, the peak shape and the background shape functions are therefore needed. The procedure is based on the least squares method, and starting from a powder diffraction data-set it can refine lattice parameters, atomic positions, fractional occupancy, and thermal parameters.
The powder diffraction experiment yields a diffractogram which consists of an array of i observed values y_{io} of the x-ray intensity, equally spaced by increments δx of the independent variable x; in our experiment this parameter is the angle 2θ. Each observed value contains the contributions of the background, of the specimen (the sum of the contributions from Bragg reflection), and of the instrument (optics). Assuming an isotropic powder distribution, the mathematical model that is assumed to represent the physical pattern [67] that will be compared with the data is

$$y_{ic} = y_{ib} + s \sum_k m_k I_k A |F_k|^2 G(\Delta\theta_{ik}) \tag{17}$$

where y_{ib} is the background intensity at the $i\text{-}th$ step, s is a scale factor, m_k the multiplycity factor for the k reflection, I_k an instrument dependent factor, A an absorption factor, F_k the structure factor, and $G(\Delta\theta_{ik})$=$G(\theta_i - \theta_k)$ is the reflection profile function, where the argument is the difference between observed and calculated positions of the Bragg peak, being θ_k corrected for the zero-point shift of the detector.
The best agreement between the observed y_{io} and calculated y_{ic} data is obtained by the well known least square method. It consists of a routine procedure based on the minimization of

the chi square function

$$\chi^2 = \sum_i \frac{1}{\sigma_i^2} |y_{io} - y_{ic}|^2 \tag{18}$$

by the variation of several parameters in the calculated intensity function of Eq. 17. Here $\sigma_i^2 = \sigma_{ip}^2 + \sigma_{ib}^2$, where σ_{ip}^2 is the standard deviation associated with the peak and σ_{ib}^2 is that associated with the background intensity y_{ib}.

Among all the parameters previously listed that in general can be refined, this work has been limited in identifying a suitable background function and the best profile function $G(\Delta\theta_{ik})$ for the peak's shape and the unit cell parameters. The background contribution arise from diffuse or incoherent scattering, amorphous phases in the sample and electronic noise in the detector system, and is usually defined by a power series in 2θ, whose coefficients are parameters of the refinement. The analytical expressions of the more useful peak-shape functions for the pattern profiling can be found on many books of crystallography [55] and/or Rietveld analysis [67]; in general they can be Gaussian or Lorentzian shaped functions, or better a convolution; the main parameter to be refined is the $FWHM_k$, that is the Full Width Half Maximum of the k-th reflection.

Chapter 3

Magnetometry and others physical characterizations

The physical properties of the samples subject of this work were investigated by several techniques: magnetization, transport (resistivity and thermopower) and neutron diffraction experiments, plus iodometric titration for evaluating the oxygen content. Among them I mainly dealt with magnetometry, that will be described here in more detail. The others techniques will be briefly mentioned at the end of this chapter.

Magnetometers are scientific instruments designed to measure the bulk magnetic response of a sample. I will limit my description to the basics of the technique I used, the SQUID magnetometry, starting from its physical principle (Sec. 3.1), and its application to the Superconductor QUantum Interference Device (SQUID), in the relevant experimental configuration and methodology (Sec. 3.2 and 3.3).
A SQUID magnetometer is essentially a magnetic flux-to-voltage transducer, that is a voltage value is associated with a measure of magnetic flux variation; under appropriate hypothesis a software turns this value into a magnetization value. This kind of magnetometer is largely exploited in research laboratories, mostly because it provides a very high sensitivity (up to $10^{-}8$ emu).

3.1 Josephson junction

A schematic view of a Josephson junction is shown in Fig. 20. It is a Superconductor-Insulator-Superconductor (SIS) junction, thus a piece of superconducting material interrupted by a "thin" insulating slab, that is a barrier potential. The real meaning of the word "thin" is determined by the possibility for the charge carriers, thus the Cooper pairs, to tunnel across the junction. The operation of a SQUID exploits a couple of Josephson

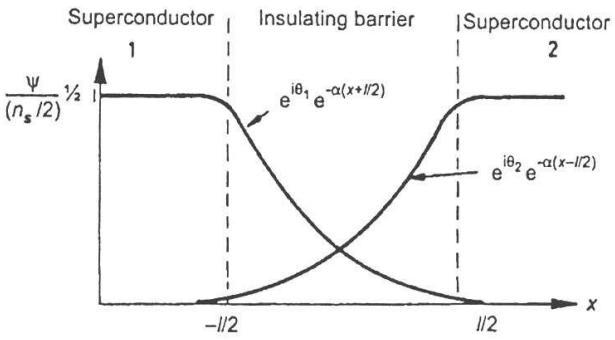

Figure 20: Josephson junction: a schematic view of the order parameters superimposition inside a thin barrier potential.

junctions, and will be described in Sec. 3.2: let us begin describing the single junction.

Following the Ginzburg−Landau theory [49,68], the charge carriers in a superconducting system can be described by a single complex order parameter, the macroscopic wave function $\psi = \psi_0 e^{i\theta}$, identified by an amplitude ψ_0 and a phase θ; this superconducting state can be considered a macroscopic quantum state. If two identical superconductors are placed far enough from each other, they do not interact, so their relative order parameters are described by independent phase values θ. If they are placed close enough each other, but not in contact, the two superconducting states are "linked" and there is a well-defined relation between their phase values, based on the probability of carriers to tunnel from one to the other, that determines the current density J across the junction. In this case they form a so called "weak-link".

If we consider the barrier potential of thickness l centered around $x = 0$ in Fig. 20, we can simply write the wave function at the generic position x as the sum of the contributions of the two superconducting wave functions

$$\psi(x) = \psi_0[e^{i\theta_1 - \alpha(x+l/2)} + e^{i\theta_2 - \alpha(-x+l/2)}] \tag{19}$$

where ${\psi_0}^2 = n_s/2$, and $n_s/2$ describes the number of superconducting Cooper pairs. The supercurrent density across the junction can be evaluated thanks to the Ginzburg−Landau equation

$$j(\mathbf{r}) = \frac{i\hbar e}{2m_e}(\psi^*\nabla\psi - \psi\nabla\psi^*) - \frac{2e^2}{m_e}\psi^*\mathbf{A}\psi, \tag{20}$$

where m_e is the electronic mass, and $\mathbf{A}$ is the potential vector that originates the magnetic field $\mathbf{B} = \nabla \times \mathbf{A}$. In the simple case $\mathbf{A} = 0$ we obtain the equation

$$I = j_0 A sin(\theta_1 - \theta_2) \tag{21}$$

where j_0 is the maximum density current for the junction, A is the junction area, and the argument of the sin function is the phase difference between the order parameters ψ in two

regions. Besides, the potential drop across the junction can be calculated [69] thanks to the equation

$$V = \frac{\hbar}{2e}\frac{\mathrm{d}(\theta_1 - \theta_2)}{\mathrm{d}t}. \tag{22}$$

Therefore, when inside a Josephson junction a certain supercurrent is flowing, the phases of the order parameters in the two regions change to satisfy Eq. 21; if the difference between these quantities is stationary, the supercurrent flows without a potential drop by equation Eq. 22, thus the junction shows zero resistance.
If a magnetic field **B** is producing a flux across the junction area, the critical current density is a function of the flux concatenated to the border of this area, and assumes the form [49]

$$I(\Phi/\Phi_0) = j_0 A \frac{sin(\pi\Phi/\Phi_0)}{\pi\Phi/\Phi_0} sin(\theta_1 - \theta_2) \;\; = \;\; I_0 sin(\theta_1 - \theta_2) \tag{23}$$

where A is the junction area, Φ is the total flux that threads the junction and Φ_0 is the flux quantum. The quantity $I_0(\Phi/\Phi_0)$ is shown in Fig. 21 vs. applied field (flux): note the diffraction-like bahaviour of the single junction, and the characteristic periodicity given by a flux quantum. This extremely high sensitivity of the Josephson current to the magnetic field is the key point to many important applications of the Josephson effect, first of all the SQUID, that will be briefly discussed in the next chapter.

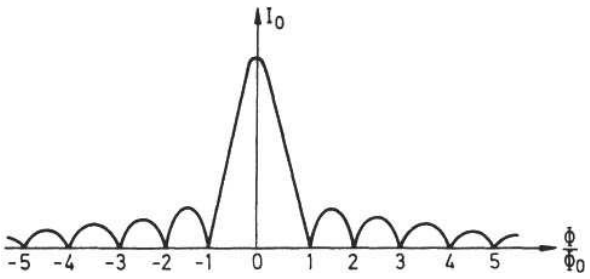

Figure 21: The magnetic field dependence of the maximum supercurrent for a Josephson junction in the applied magnetic field; note the single-slit diffraction-like behaviour, typical of wave optics; this is due to the phase change along a direction perpendicular to the junction axis [49].

3.2 dc-SQUID

A dc SQUID is a weakly-connected superconducting loop containing two Josephson junctions, as shown in Fig. 22. This loop is allowed to contain flux only in multiples of the flux quantum Φ_0. Thus a change in the external contribution to the flux concatenated with the loop will cause currents to flow to compensate that change, corresponding to a phase difference across the junction, giving rise to a voltage across the loop which we may detect.

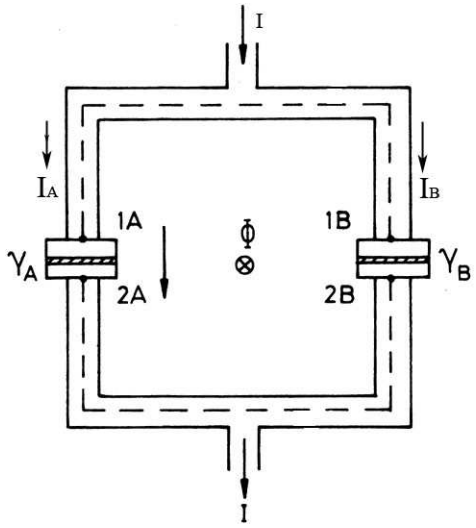

Figure 22: Schematic diagram of a dc SQUID: the phase difference between the entering and exiting supercurrent is strongly dependent on the external magnetic flux concatenated with the superconducting loop [49].

The ring is thermalized at $\sim 2\,\mathrm{K}$, and is biased by a constant current I_{bias}; the bias current is shared in to the components I_A and I_B, between the two SQUID branches, and each component encounters a junction. The I_{bias} current in the "zone 1" (thus upstream with respect to the junctions) before the distribution, has to be the same in the "zone 2" (thus downstream with respect to the junctions) after the recombination, except for the phase shift introduced by the barriers potential in the "links" (that in principle could be different, so $\gamma_A = \theta_{2A} - \theta_{1A} \neq \gamma_B = \theta_{2B} - \theta_{1B}$).

Tankig into account the junction equations, the inductance of the superconducting loop and the presence of a vector potential due to any external field which influences the phase values in the superconducting regions, the value of the overall critical current density can be calculated [69]; neglecting the magnetic flux contribution across the junction, the stronger dependence in the equation describing the current of the device is on the external magnetic flux concatenated with the superconducting loop, that can be expressed by the equation

$$I(\Phi/\Phi_0) = 2j_0 A cos(\pi\Phi/\Phi_0) sin\gamma_0 = I_0 sin\gamma_0 \tag{24}$$

with $\gamma_0 = \gamma_A - \pi(\Phi/\Phi_0) = \gamma_B + \pi(\Phi/\Phi_0)$ and $\gamma_A = \theta_{1A} - \theta_{2A}$ $\gamma_B = \theta_{1B} - \theta_{2B}$. The dependence of I_0 on flux is graphically shown in Fig. 23. As long as the current flowing in the device is smaller than I_{max} the phase γ_0 adjusts itself so the current flows without dissipation; I_0 is in fact the maximum current which can flow in the device without dissipation. It is very interesting to note that I_0 reaches its maximum for an integer number of flux quanta enclosed within the loop, while it goes to zero whenever the number of flux quanta is half integer; this periodicity is analytically expressed by the cosine dependence. This behaviour provides the

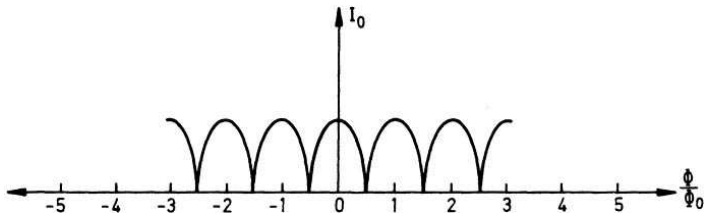

Figure 23: Dependence of the maximum supercurrent I_{max} on flux for a dc SQUID, expressed in equation (24), [49]. The periodicity corresponds to a magnetic field $B = 2 \cdot 10^{-11}$ T, and its value goes to zero whenever the number of enclosed quanta is an half-integer.

basis for the operation of the dc SQUID magnetometer and permits us to measure extremely small fields: as an example, if the ring area is $1\,\mathrm{cm}^2$, since $\Phi_0 = h/2e = 2 \cdot 10^{-15}\,\mathrm{Tm}^2$, the flux periodicity corresponds to a field $B = 2 \cdot 10^{-11}$ T. Actually the sensitivity of the instrument is higher than the one associated to the previous periodicity, as it is clarified in the next section.

3.3 dc-SQUID operation and measurements methodology

Let us consider the $I_0(\Phi/\Phi_0)$ dependence expressed in equation (24) and graphically visualized in Fig. 23. Let us set our attention, for example, on the value that the curve assumes for $\Phi = 0$, thus the central maximum. If the bias current is high enough, the junctions are driven to the normal state, and a potential drop appears across the SQUID; if the bias current is lower than the critical current, the SQUID is in the superconducting state; so that if an external variation of the concatenated flux lowers the critical current (thus leads the critical current under the bias value), a voltage drop appears once again across the SQUID. This voltage, say V_s, turns out to be periodic itself with the same periodicity of I_0 of Fig. 23; it is the output signal from the device, and can be detected thanks to an appropriate solution. Therefore, in practice, the dc-SQUID operates with a constant biasing current slightly greater than the critical current; it is always resistive, and the voltage one measures across turns out to be periodic in the magnetic flux with a period of one quantum. The output voltage V_s is not directly detected, in order to minimize the signal-to-noise ratio and to linearize the response. It is fed to the so called "flux−locked−loop" (FLL), shown in Fig. 24. In this configuration a slow external modulation ($\sim 1 - 100\,\mathrm{Khz}$) of amplitude $\sim \Phi_0/2$ and a feedback circuit (amplifier-lock in-integrator), inductively coupled with the SQUID, keep the system at one of the extrema of the $V_s(\Phi/\Phi_0)$ curve linearizing the response. The output signal of the FLL circuit turns out to be proportional to the feedback signal [69].
It is usually necessary to measure a magnetic moment induced by an external field, which interferes with the SQUID measurement. To minimize this effect the SQUID is inductively coupled to the sample thanks to a specifically designed pick-up superconducting circuit (rep-

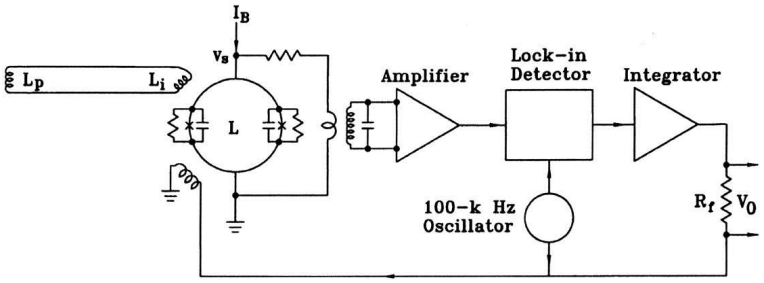

Figure 24: Circuit with pick-up coil (L_p), input coil (L_i), SQUID and flux-locked loop. A change in the magnetic field at the pick-up coil (inductance L_p) induces a change in the field at the input coil (inductance L_i). The SQUID is inductively coupled to the input coil and detects a change in magnetic flux. The voltage response V_s is the input for the flux-locked loop, which uses a modulation flux scheme [69] to hold the SQUID at an extreme of the $V_s(\Phi/\Phi_0)$ curve. The user measures a change in V_0, which is proportional to the feedback from the loop and hence to the change in magnetic field at the pick-up coil [70].

resented by L_p in Fig. 24), hence the SQUID can be shielded from external not desired fields. The sample space with its related hardware controls and the pick-up circuit geometry are shown in Figs. 25 and 26. The signal detection circuit adopts the second-order gradiometer configuration shown in Fig. 26, usually called pick-up coil. It consists in four identical coils, the two central ones wound clockwise and the external ones wound counterclockwise in symmetrical position from the center; in this way the pick-up coil produces a current which is proportional to the external field gradient, rather than to the field itself. This configuration is not optimized for the signal detection, but it shows the very important advantage of being in principle not sensible to the variations of the external field, so it can reduce the noise due to its fluctuations [71].

By moving the sample through the symmetry axis of the pick-up coil its magnetic moment couples inductively (L_p in Fig. 24) and produces a current variation in the superconducting circuit, which is proportional to the total flux amount across the four coils. The same current is then coupled to the SQUID loop (the inductive coupling is represented by L_i in Fig. 24), being its input signal, and produces a final voltage output V_0 form the FLL, as one can gather from the figure. In the point-like approximation of a magnetic moment **m** lying along the gradiometer axis at distance x from the center of a coil, the concatenated flux can be simply calculated thanks to the following relation

$$\Phi_B(x) = \frac{\mu_0 m}{2} \cdot \frac{R^2}{(R^2 + x^2)^{\frac{3}{2}}}. \tag{25}$$

where μ_0 is the Bohr magneton, R the coil radius. Since the pick-up takes place thanks to a four coil series (as shown in Fig. 26), the total flux amount will be the algebraic sum of the

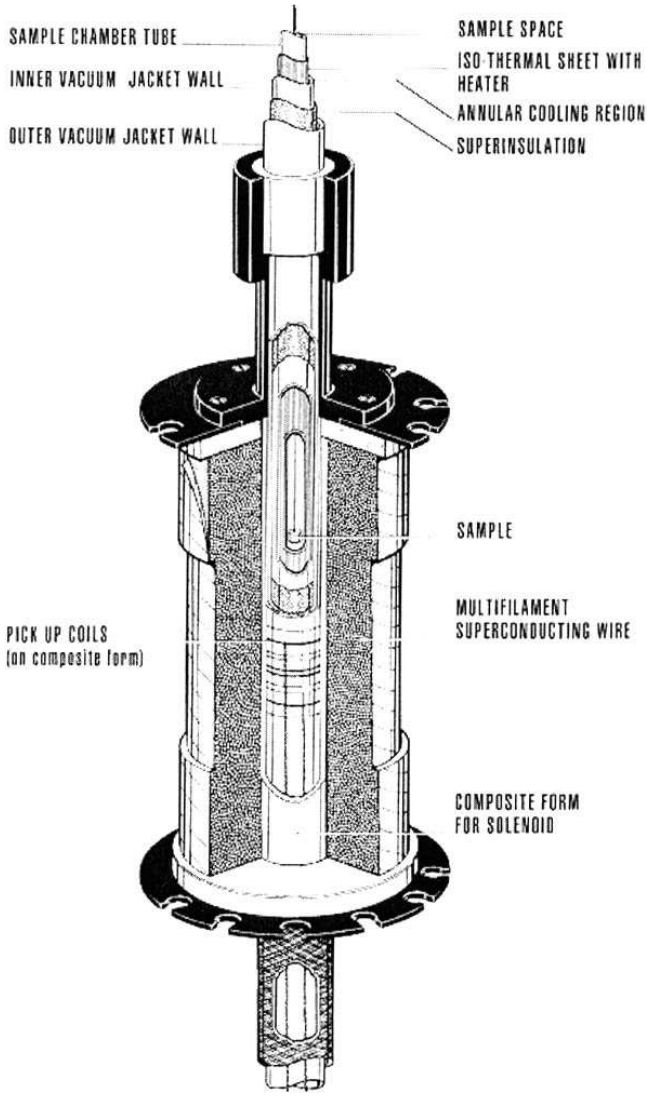

Figure 25: Longitudinal section of the sample space and its related hardware controls, including the location of the second order gradiometer superconducting detection coil and the external superconducting main coil for external field (up to $5\,\mathrm{T}$) application [71]. The sample is drop into a vacuum chamber which temperature can be varied from $2\,\mathrm{K}$ to $400\,\mathrm{K}$.

four contributions; thus the overall calculated voltage vs. sample position is

$$\Phi_B(x) = \frac{\mu_0 m R^2}{2} \sum_{i=1}^{4} [(x + d_i)^2 + R^2]^{-\frac{3}{2}}, \tag{26}$$

where d_i is the axial distance from the center of the gradiometer of the i-th coil. A measure consists in an average of several scans of the sample position to reduce the noise (from two to six, depending on the signal to noise ratio); finally the software fits the measure values to the function of equation 26 to extract the value of of the magnetic moment. The conversion factor from voltage to magnetic moment needs a separate calibration performed with a reference sample (a small Palladium cylinder of known mass and susceptibility in the case of the SQUID

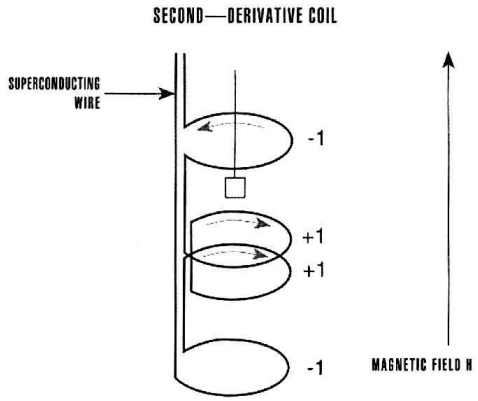

Figure 26: Configuration of the second order gradiometer superconducting detection coil. The current induced in the central windings flow opposite to that induced in the external ones. This configuration is pretty low dependent on external field variation, thus the measured signal can be totally ascribed to the sample. [71]

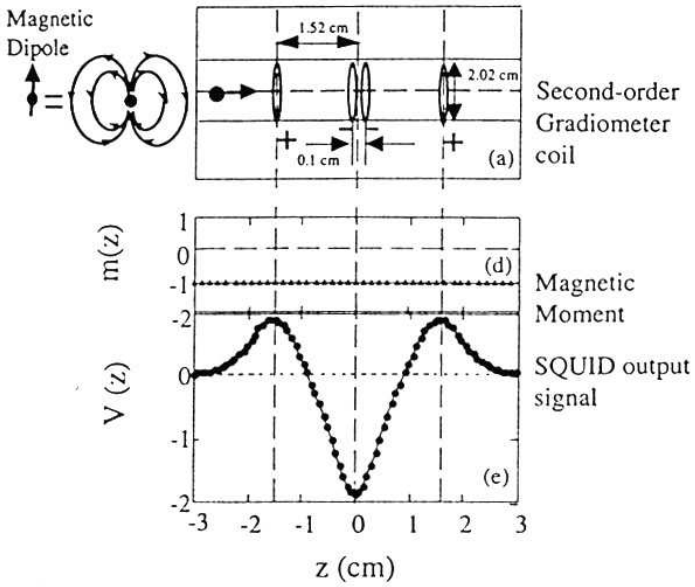

Figure 27: Raw diamagnetic output SQUID signal, amplified by the FLL circuit of Fig. 24, as a function of the sample position along the gradiometer axis. The gradiometer geometry is shown in Fig. 26. From the best fit curve (continuous line) one gathers the sample magnetization value **m** [71].

used for this work). Further practical aspects of the measure will be better explained in the following section.

3.4 Some practical aspects in the SQUID measurement

We performed the bulk superconducting characterization at our physics department by using a Quantum Design SQUID MPMSXL-5 magnetometer, equipped to perform DC susceptibility measurements in the temperature range 1.8 K<T<400 K and up to an applied field of

5T. we evaluated the transition temperatures as the linear extrapolation of the 90% to 10% diamagnetic drop of suscebtibility, in a field $\mu_0 H = 0.2$ mT. It is worth to do some useful practical consideration keeping in mind when performing a SQUID measurement.

Residual field presence.
As already discussed our interest was mainly focused on the determination of both the transition onset and width, so we choose the very low field =(2 Oe) to reduce pinning effects. Keeping in mind that the whole system is shielded from the external world, it is possible that a previous high field measurement gives a not desired small residual magnetization of the shield which could introduce artifacts in low-field or zero-field measurements. The same happens for the field given by flux quanta trapped in the magnet superconducting coil. For these reasons some options to minimize the trapped flux are available.

First of all a magnet reset option is usable. It assures that no flux quanta were trapped in the superconducting coil by heating the same over the transition temperature; the winding is so guided in the normal state before the subsequent measurements. Actually it is possible to evaluate the average residual field by an $M(H)$ measurement on a magnetic sample. We performed a series of four low field (10 Oe, -10 Oe, 5 Oe, -5 Oe) ZFC measurements on the slightly overdoped $Y_{0.95}Ca_xBa_2Cu_3O_7$ sample. The result is shown in figure, where a residual averaged field equal to ∼-0.5Oe is present for M=0; this is mainly due to the magnetization of the external permalloy shield that produces this significant residual field ($-1/4$ of the standard field utilized in our measurements). In any case one needs a better control on the real residual field value, which is achieved by a degauss shield and a subsequent ultra low field options.

Degaussing the permalloy shield surrounding the dewar may not be necessary if the MPMS superconducting solenoid has not been energized to fields high enough to magnetize the shield: typically, this is a field > 200 Oe. Starting from 5000 Oe the shield undergoes series of narrower and narrower hysteresis cycles toward zero. The field profile after the magnet reset and degauss shield options in shown in blue in Fig. 29, where the field value is now directly measured by an hall probe.

The ultra low field option guaranteed a very high precision (~ 0.02 Oe) in the field nulling procedure. It adjusts the magnetic field basing on readings from the flux-gate sensor, so the option sets the field to zero at the position of the sensor one can specify. Nulling consists of the following operations: the system performs a zero-field quench of the magnet to release the trapped flux that remains in the magnet, than it reads the remnant field at the location of the flux-gate sensor. A compensation field is now applied by driving a current in the low-field coil; the compensation field is opposite in direction to the remanent field, so it cancels the remnant field. The system quenches the magnet again while the low-field

coil holds the compensation field and then removes the compensation field and then reads the remnant field at the location of the flux-gate sensor. As last step the system applies the compensation field again and adjusts the current in the low-field coil to further null the field. This process is repeated for the maximum number of iterations or until the residual field read by the flux-gate sensor is less than the remnant tolerance parameter. The residual field is 20 mOe for our 5T magnet, and is shown in red in Fig. 29; the ultra low field option turns out the lowest possible residual field.

Sample holder

Of course, each sample needs its own sample holder; thus an unwanted contribution to the final magnetization amount may rise from the sample holder, which is moving together with the sample across the pick-up circuit. To reduce this effect one can employ radial symmetric sample holders quite longer than the distance between the two external coils, so they do not produce any flux variation in the pick-up coils as the scan is performed. We used to employ a plastic drinking straw for our measurements, which shows a very low diamagnetic contribution definitly negligible by comparison with typical superconducting signals.

Point-like approximation.

In chapter 3.3 we explained how the SQUID extracts the magnetization values from a linear regression curve which considers point-like samples on the gradiometer axis. If the sample

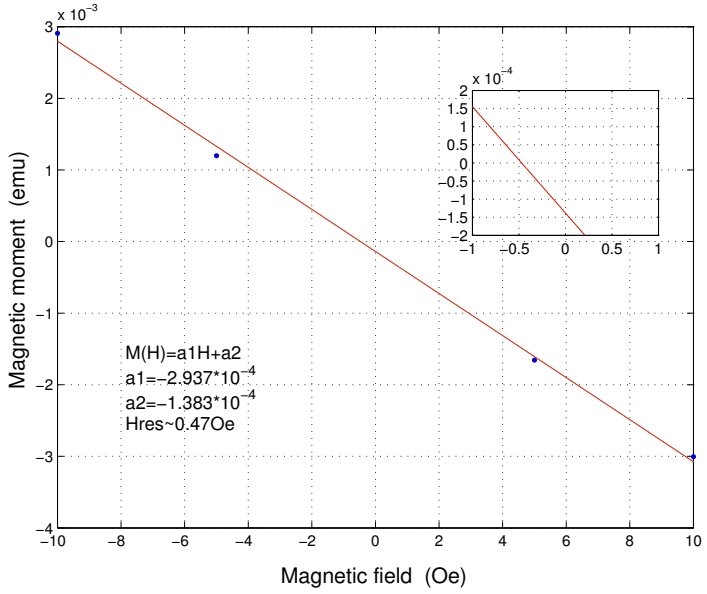

Figure 28: $M(H)$ response of $Y_{0.95}Ca_xBa_2Cu_3O_7$. For low fields the linear dependence is satisfied, and the intercept with the x-axis, enlarged in the inset, shows a rough average estimation of the residual field inside the magnet. The coefficients and residual field values are also displayed.

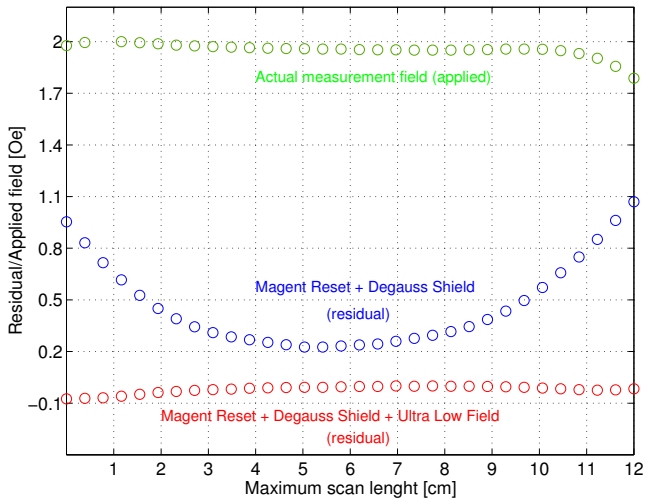

Figure 29: Residual (blue, red) and applied (green) fields inside the sample chamber of a MPMS system. The difference between the blue and the red circles highlights the accuracy in the determination of the residual field, while the green circles represents both the actual value and the homogeneity of the field present in the chamber when one sets the field at the measurement value (note that the usual scan length is 4 or 6 cm, hence shorter than the maximum scan length).

has a considerable extention by comparison with either the gradiometer or the calibration sample length, then the linear regression can give wrong results; extra care has to be taken to the sample extension and to the geometrical setting when preparing for a measurement.

Environment.
In principle a good rule is not to touch either with hands or magnetic tools all you will insert in the sample chamber in order to avoid contaminations of the sample space. Several gassy helium flushing out guarantee the exclusion of oxygen and nitrogen, whose condensation at low temperatures would bring to the formation of dry ice inside the chamber, limiting the instrument transport movement.

3.5 Other physical characterizations

Other techniques have been of fundamental importance in this work. In particular the Neutron Scatting (NS), the Seebeck effect and the Iodometric Titration.

Time-of-flight neutron diffraction patterns have been collected at the ISIS spallation source to extract the real content of both the R= Eu, Nd, Ca and O species in selected samples

of $Y_{1-x}R_xBa_2Cu_3O_{6+y}$. An example of NS Rietveld refinement is reported in Fig. 52, Sec. 5.2.

The thermoelectric power $S(h, e)$ of a material is the coefficient of the Seebeck effect. It measures the magnitude of an induced electric voltage in response to a temperature difference across that material; if the temperature difference between the two extremes is small, then the thermopower can be approximated [72] as $S = \Delta V/\Delta T$, where ΔV is the electric voltage seen between those points. In cuprates, the room temperature Seebeck coefficient $S^{RT}(h)$ is a measure of the intrinsic equilibrium electronic states of doped holes [73, 74, 75]. It has been measured for all the samples object of this work (see Sec. 5.3).

The Iodometric titration is a chemical method that accurately determines the oxygen content by the average oxidation state (2+h) of the Copper ions [76, 77]. In cuprates this kind of analysis have been largely exploited the years [78, 79], also with good improvements [80, 81]. In our case, the absolute oxygen calibration of the end members of each sample batch leads to an error of 1%.

Chapter 4

Muons and μSR technique

4.1 Muons

The muon is the second generation lepton. Its rest mass is equal to 107.5 Mev, 207 times the electron mass, and 1/9 the proton mass. It has spin $\mathbf{S}^{\mu} = 1/2$, and it features two eigenstates of the electric charge (-1,+1); we are dealing here with the positive muon, which, from a condensed matter prospective, behaves as a light proton rather than a heavy electron. Differently from the electron and the proton, this particle is not stable, and it spontaneously decays via weak interactions with an average lifetime $\tau_{\mu} = 2.2\,\mu$s. The muon μ is one of the elementary particles that compose our universe; speaking about elementary particles we mean particles that do not show internal structure.
The first sign of the muon presence goes back to a work by Kunze in 1933; the trial of a highly ionizing particle was highlighted inside a Wilson cloud chamber; a simple argument demonstrated that the particle energy could neither be attributed to an electron, nor to a proton. The identification of the muon is due to C.P. Anderson ed S.H. Neddermeyer in 1936, during their studies on the nature of cosmic rays. Cosmic rays are formed by charged particles of very high energies (up to 20 Tev); when these particles enter the atmosphere they interact with atomic nuclei, and the scattering process creates barions and mesons, whose decay spontaneously originates respectively leptons and light barions; among all, the most frequent production channel is the weak β-decay of π meson into muons and muonic neutrinos. Although they are very unstable, many of them (about $1\mu/min \cdot \mathrm{cm}^2$) reach the earth crust thanks to the time dilation described by the special relativity equations, as a consequence of their velocity close to c: one of these events was the subject of the report by Kunze. Measuring the energy loss of the particles forming cosmic rays, in their experiments Anderson and Neddermeyer concluded that the events involved particles characterized by unitary charge and mass larger than that of the electron one and smaller than that of the proton. Powell and collaborators later quantitatively clarified these results, evaluating the

muon mass $m_\mu = 205\, m_e$, and showing that the muon is the decay product of the pion π, the mediator of strong interactions in the Yukawa theory, whose mass and lifetime are approximately $m_\pi = 273\, m_e$ and $\tau_\pi = 2.6 \cdot 10^{-8} s$.
We know methods to artificially generate muons of selected charge and spin polarization, which will be described below. These methods are the key to the μSR technique.

4.2 Muon Spin Spectroscopy μSR

Historically the acronym μSR was intended to convey different meanings, such as Muon Spin Rotation, Relaxation or Resonance, depending on the type of the performed experiment.
This condensed matter investigation technique is very similar to Nuclear Magnetic Resonance (NMR) or to Electron Paramagnetic Resonance (EPR); by contrast with electrons and nuclei, already present in EPR and NMR samples, muons must be implanted; as a consequence μSR experiments must be performed in large scale facilities (ISIS and PSI in Europe), where muon production takes place exploiting proton accelerators of suitable characteristics. A polarized muon beam is aimed at the sample: muons stop at interstitial sites and their spin dynamics is measured from the angular distribution of the positrons emitted in their decay. The time evolution provide informations about the distribution of internal fields, which is of great interest typically in the case of magnetic and superconducting materials. Thanks to their large magnetic moment, about $4.5 \cdot 10^{-26}$ J/T, muons can measure small internal magnetic fields, such as the ones generated by Copper nuclear spins (less than 0.01 μ_B). Moreover this technique is very useful in the study of multiphasic or partially ordered samples, since the muon implantation takes place randomly inside the sample, and the signal amplitude in the spectrum turns out to be proportional to the volume fraction of the different phases. A detailed analysis of the technique follows for the two experimental configuration widely used in this work; they correspond to the first and the second meaning of the acronym μSR, that is Rotation and Relaxation.

4.2.1 Muon production as μSR probes

Muons generated as μSR probes are controlled in energy, flux, electric charge, spin polarization. For our purposes positive μ^+ are more useful than negative μ^-, being the latter captured by high atomic number nuclei. μSR experiments require spin polarization control; during the production process we are able to obtain a nearly 100% polarized beam.
Pulsed (ISIS) or continuous (PSI,TRIUMF) beams of protons are driven to high energies and directed on a thin graphite target, where positive pions π^+ are generated according to the following equation

$$p + p \rightarrow \pi^+ + p + n. \tag{27}$$

The pions generated in the process are spread in energies, but they can be selected in momentum with a dipole magnet into a beam of low energy pions that decay according to the following process

$$\pi^+ \rightarrow \mu^+ + \nu_\mu. \tag{28}$$

with an average lifetime of 26 ns. This is a two-body weak interaction decay: let us consider it in the pion rest reference system. The pion is a zero spin particle $\mathbf{S}^\pi = 0$, while the neutrino has $\mathbf{S}^\nu = \frac{1}{2}$. Parity violation, intrinsically associated to the weak decay, forces the neutrino to emerge with its projection S_z^ν in the same direction of its motion, but with reverse orientation, that is opposite in sign. Therefore the emitted muon, for angular momentum conservation, must also have negative helicity. This argument holds in the rest reference system; a large spin polarization is therefore preserved selecting the muon momentum either from π decaying on the target surface, at rest (surface muons), or from relativistic π. We consider here only surface muons, which have relatively small linear momentum and kinetic energy, respectively ~ 27 Mev/c and ~ 4.2 Mev. These muons stop within 10-100μm in condensed matter, loosing their epithermal energies mostly by ionization processes. The thermalization lasts less than $\Delta t = 10^{-9}$ s. The process may include a series of electronic captures and reemissions when the energy is of order of a hundred eV. This process can form muonium, the muonic equivalent of the hydrogen, where the proton is replaced by the μ^+. The time scale of the whole process of stopping and thermalizing of μ^+ is much shorter than the typical spin precession period, so that the implantation takes place without loss of spin polarization.
Muons decay according to:

$$\mu^+ \rightarrow e^+ + \nu_\mu + \bar{\nu_e} \tag{29}$$

with a life-time of 2.19714(7) μs. The Feynman diagram describing the weak process of muon decay is shown in Fig. 30. This is a three-body decay, so the positron energy, the only particle detectors are sensitive to, is not determined and varies as a function of the distribution of

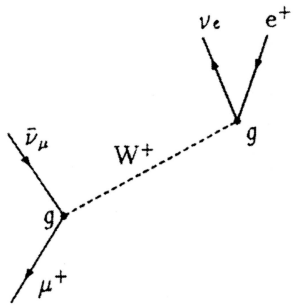

Figure 30: The Feynman diagram describing the weak process of muon decay; W^+ is the exchange boson involved in this decay.

linear momentum among the particles. The probability distribution $W(\theta, \epsilon)$ of the decay positrons is given [82] by

$$d^2W = W(\theta,\epsilon)d\epsilon d(\cos\theta) = \frac{G^2 m_\mu^5}{192\pi^3}(3-2\epsilon)\epsilon^2\left[1-\frac{2\epsilon-1}{3-2\epsilon}\cos\theta\right]d\epsilon\, d(\cos\theta) \tag{30}$$

where $G \sim 1.166 \cdot 10^{-5}(hc)^3[GeV]^{-2}$ is the Fermi weak constant, $\epsilon = E/E_{max}$ and θ is the angle between the muon spin and the emerging positron momentum. By integrating Eq. 30 over both ϵ and $\cos\theta$ we obtain the total decay probability per unit time, which is equal to the inverse of the muon lifetime τ_μ

$$W = 1/\tau_\mu = G^2 m_\mu^5/192\pi^3 \tag{31}$$

The energy spectrum of the positrons follows from Eq. 30 by integrating over $\cos\theta$ alone

$$dW(\epsilon) = W(\epsilon)d\epsilon = \left[2\epsilon^2(3-2\epsilon)/\tau_\mu\right]d\epsilon. \tag{32}$$

The energy spectrum is shown in Fig. 31, together with the asymmetry factor in front of the cosine in Eq. 30. The asymmetry factor $a = (2\epsilon-1)/(3-2\epsilon)$ depends on the positron energy; it becomes unity for $\epsilon = 1$ which means that no positrons with maximum energy are emitted antiparallel to the μ^+ spin.

The left panel of Fig. 32 displays the angular dependence of the probability decay for various asymmetries a; the perfect circle at 26 Mev ($\sim m_\mu$) is the minimum energy curve of the positron, and corresponds to $a = 0$, while the perfect cardioid at 53 Mev ($\sim \frac{m_\mu}{2}c^2$) is the maximum energy curve, and corresponds to $a = 1$. The right panel displays the integration over all energies which leads to the value $a = 1/3$, close to the experimental value which is affected by the detectors sensitivity and by their geometry (the solid angle they cover); this value will be called A.

Once implanted in the sample, the local magnetic environment dictates the time evolution

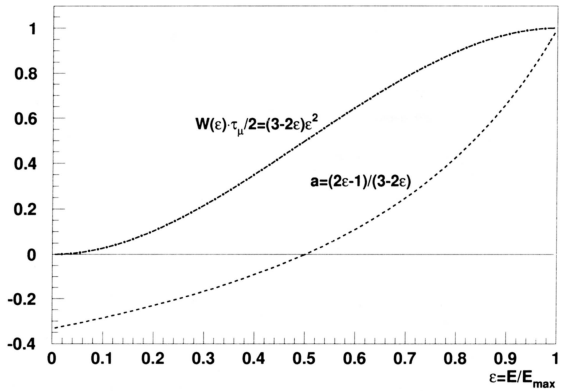

Figure 31: The energy spectrum and the asymmetry of a spatial distribution are plotted versus the energy of the decay positrons. For the minimum energy permitted $a = 0$, for the maximum $a = 1$.

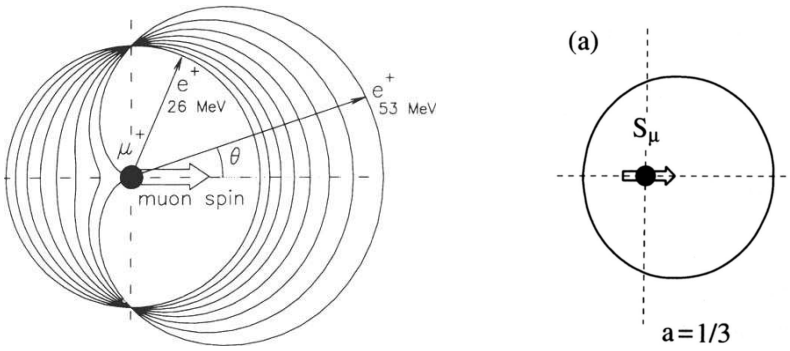

Figure 32: The left panel shows the angular distribution of positrons from a μ^+ decay with E_{min}=26Mev< E_{e^+} <52Mev=E_{max}; in the right panel the angular distribution is integrated over all energies.

of the muon spin. If a unique magnetic field **B** is present at all the muon sites, spin vectors precess around it at the Larmor frequency

$$\omega_\mu = \gamma_\mu B \tag{33}$$

where $\gamma_\mu = g\frac{e}{2m_\mu} = 2\pi \cdot 136\,\mathrm{MHz/T}$ is the gyromagnetic muon ratio and $g{\approx}2$ is the gyromagnetic spin factor. The probability of emission $W(\theta, \epsilon)$ expressed in Eq. 30 is directly proportional to the number of emitted positrons $N(\theta, \epsilon)$, that is $W(\theta)$ is proportional to $N(\theta)$ after summing over all energies; if the spin precesses at frequency ω, the angle in $W(\theta)$ will obey to $\theta = \omega t$, i.e. it will produce a periodic modulation in $N(\theta)$, at the same frequency of the spin precession. By measuring experimentally this frequency, that is, following in time the angular distribution of the emitted positrons, one can calculate the local magnetic field **B** thanks to Eq. 33 .

4.2.2 Transverse Static Field (TF): μSR = Muon Spin Rotation

This experimental setting will be discussed referring to the right panel of Fig. 33. The applied magnetic field $\mathbf{B}_{ext}$ lies along the vertical **x** axis, perpendicular to the spin of incident muons and gives rise to their precession. In the following I shall include a crude treatment of spin relaxation, which follows closely that of NMR [84, 85]. In order to clarify the physical pictures I shall assume simple situations and distinguish the static from the dynamic effects, by assuming that the time variation of the local field $\mathbf{B}_\mu$ at the muon may be described by a single fluctuation rate $1/\tau$. The field is static if $\gamma_\mu B_\mu \tau > 1$, otherwise it will produce dynamical relaxations. Of course when $\tau_\mu/\tau \ll 1$ the muon decay makes both static and dynamic relaxations unmeasurable, i.e. the environnment is static on the time-scale of muons.

Let us consider for example the B detector, in line with the incident beam, placed upstream relative to the sample. The positron number detected in absence of any muon spin

polarization would be given by the well known exponential decay of a particle of lifetime τ_μ

$$N_B(t) = N_B(0)e^{-\frac{t}{\tau_\mu}} \tag{34}$$

where t is the time delay between the muon implantation and its decay, $N_B(0)$ the initial count rate. Applying the transverse magnetic field $\mathbf{B}_{ext}$, the spin starts precessing at a frequency ω_μ around the external field. This results in a periodic modulation of the count rate

$$N_B(t) = N_B(0)e^{-\frac{t}{\tau_\mu}}[1 + A\cos(\omega_\mu t + \phi)] \tag{35}$$

where ϕ is the phase shift corresponding to the angle between the detector axis and the initial polarization, A is the experimental asymmetry defined in Sec. 4.2.1. The field at the muon site is actually the vector composition of the external field $\mathbf{B}_{ext}$ with any field of internal origin; in a powder this produces a distribution of precession frequencies $f(\omega_\mu)$, that means a dephasing of the spin ensemble, which gives rise to a damping of the oscillation, of envelope $G_x(t)$.

The positron count rate reflects the damped precessions accordingly to

$$N_B(t) = N_B(0)e^{-\frac{t}{\tau_\mu}}[1 + AG_x(t)\cos(\bar{\omega}_\mu t + \phi)] = N_B(0)e^{-\frac{t}{\tau_\mu}}[1 + AP_x(t)], \tag{36}$$

where $\bar{\omega}_\mu$ is the average precession frequency, and the term $P_x(t)$ is called transverse muon polarization; Fig. 34 shows the count rate function of Eq. 36 for the B (Backward) and F (Forward) detectors.

The depolarization described by $G_x(t)$ may originate from a static field distribution but also from dynamic fluctuations. If randomly oriented static magnetic moments produce the local field on the muon site, the distribution of the internal field moduli $p(B) = \int \delta(B - |\mathbf{B}_{ext} - \mathbf{B}_i(\Omega)|)d\Omega/4\pi$,

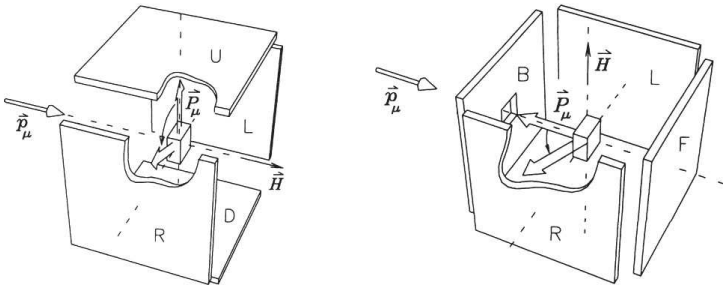

Figure 33: Two sketches of TF μSR experimental geometry. P_μ and p_μ refer respectively to the polarization and momentum vectors of the muon beam. **H** is the direction of the applied magnetic field. In the left panel the field **B** lays on the beam direction, perpendicular with respect to the muon spin, so the active counters are U (Up), R (right), D (Down), L(Left). In the right panel muon P_μ and p_μ are aligned, while **B** is perpendicular to them, so this time the active counters are B (Backward), R (right), F (Forward), L (left) [83].

i.e. the probability that the muon measures the field modulus B, is often approximated by a Gaussian function

$$p^G(B_i) = \frac{\gamma_\mu}{\sqrt{2\pi}\Delta} e^{-\frac{(\gamma_\mu B_i)^2}{2\Delta^2}} \qquad (i = x, y, z) \tag{37}$$

with standard deviation $\frac{\Delta}{\gamma_\mu}$, and the deriving $G_x^G(t)$ has the form

$$G_x^G(t) = e^{-\frac{1}{2}\sigma_G^2 t^2} \tag{38}$$

of standard deviation σ_G proportional to the second moment of the field distribution of Eq. 37 along **x**. For instance it is typically a good approximation for nuclear dipolar fields, and for internal fields in spin glasses, where the field acting on the muon site results as the superposition of many static randomly distributed contributions.

In dynamic conditions, when electronic spin produces time-variable fields at the muon site, or when muons themselves hop among different sites, a simple time-dependent perturbation theory shows that an internal field fluctuating with rate τ^{-1} yields an additional dynamic damping

$$p^L(B, \tau) = \frac{(\gamma_\mu \overline{B}_i)^2 \tau}{1 + {\gamma_\mu}^2 (B + \overline{B}_i)^2 \tau^2} \tag{39}$$

where $\overline{B}_i$ is the secular part of the fluctuating field amplitude. Therefore in the case of fast fluctuations, when $\gamma_\mu \overline{B_i} \tau \ll 1$, the Fourier transform of Eq. 39, $G_x^L(t)$, is described by the exponential relaxation

$$G_x^L(t) = e^{-{\gamma_\mu}^2 {\overline{B}_i}^2 \tau t} \tag{40}$$

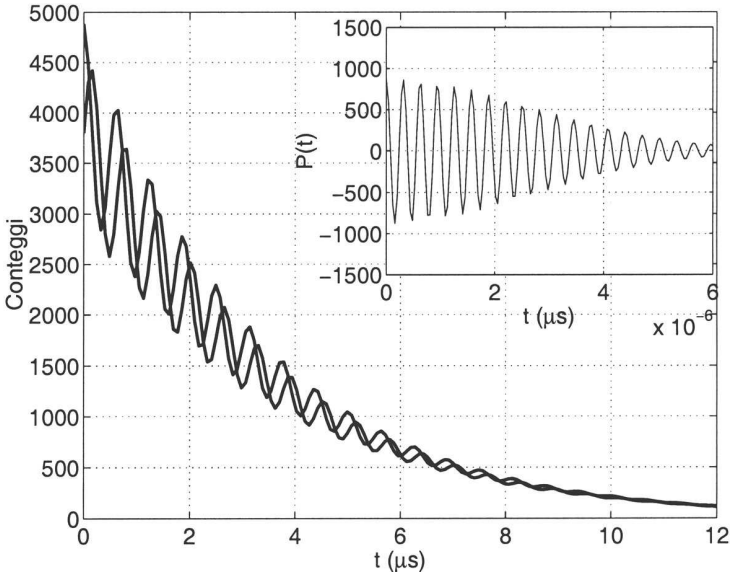

Figure 34: Positron counting in the B (Backward) and F (Forward) detectors in TF configuration. The main window shows the raw counting, the corresponding transverse depolarization function is shown in the inset.

4.2.3 Zero Field (ZF) or Longitudinal Static Field (LF): μSR = Muon Spin Relaxation

The experimental setting is the same for longitudinal field (LF) and zero field (ZF) μSR, so these configurations will be discussed referring to the right panel of Fig. 33. In longitudinal configuration the active detectors are B and F, the pair with axis parallel to the muon polarization direction, and the positron count rate is

$$N_i(t) = N_{oi} e^{-\frac{t}{\tau_\mu}} [1 + AG_z(t) \cos \phi_i] \qquad i = F, B. \tag{41}$$

We define $N_i(t) = N_B(t)$ for $\phi = 0$ and $N_i(t) = N_F(t)$ for $\phi = \pi$, which are the raw data from a μSR experiment.
The muon asymmetry can be written as

$$AG_z(t) = \frac{N_F(t) - \alpha N_B(t)}{N_F(t) + \alpha N_B(t)} \tag{42}$$

where $\alpha = N_{oF}/N_{oB}$ is an instrumental normalization factor accounts for the different sensitivity of the two detectors B and F. The constant α is experimentally determined by means of a preliminary calibration measurement typically performed in the normal-state, that is at a temperature greater than that of any magnetic or superconductive order. This is performed by applying a small transverse field B ($\sim$ 20 G in our case), at $T > (T_c, T_N)$. The spin precession produces an oscillating polarization and the experimental ratio of Eq. 42 obeys the condition $P_z \cong A(cos\gamma Bt) + B(\alpha')$ for the generic real number α', with $B(\alpha) = 0$ for the physical condition $\alpha' = \alpha = \frac{N_{oF}}{N_{oB}}$. The detector counts for B and F in zero field configuration, together with the corresponding asymmetry function, are shown in Fig. 35.

A real experiment is performed as follows. Thin compact disks ($\phi \sim 3$ cm) of powdered samples are prepared and then cooled down in zero or applied field, depending on the experimental set-up, as discussed in the next chapters. The sample mass is calculated in order to prevent muons to stop in the back side of the sample holder. Moreover, being the intensity of the muon beam section a 2-d spatial Gaussian profile, some muons implant in the holder surrounding the sample-disk. In order to avoid the relative spurious signal, the sample holder is covered by 625-μm kapton foils; kapton is a polymeric material that determines a very quick muons dephasingand this thickness is enough to stop all of the muons. These two expedients minimize spurious contributions; however a very small fraction of muons unavoidably ends in the in the cryostat walls. Assuming these muons having a minimal relaxation and precess at the Larmor frequency appropriate to the external field, a simple calibration measurement determines this small fraction. In the following we assume that this fraction is always subtracted from the raw data.

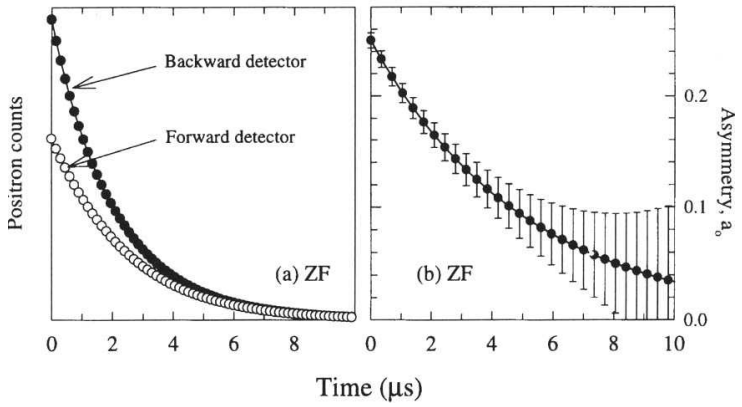

Figure 35: (a) Simulation of raw data (positron detected) in the F (forward) and B (backward) detectors in the ZF geometry. (b) Related symmetry calculated via (42). The simulation assumes realistically $N_{B,F}(t=0) \sim 10^4$ events.

4.2.4 Spontaneous internal fields in zero applied field (ZF)

When the local magnetic field $\mathbf{B}_{loc}$ and the muon spin initial direction $\mathbf{S}_\mu$ form an angle θ, the latter precesses around the former describing a cone of aperture θ as shown in Fig. 36. The contribution to the polarization along $\mathbf{z}$ will be given by

$$\sigma_z(t) = \cos^2\theta + \sin^2\theta\cos(\gamma_\mu B_{loc} t) \tag{43}$$

where the first term corresponds to the average time-independent polarization along $\mathbf{z}$, while the second to the precessing asymmetry. The muon spin relaxation function $G(t)$ can be obtained by averaging $\sigma_z(t)$ over the field probability distribution $P(B)$. In the following, we discuss the case for specimens where the directions of $\mathbf{B}$ are random, isotropically distributed. For a stationary $\mathbf{B}$, randomly oriented on the solid angle 4π, and with a distribution of second

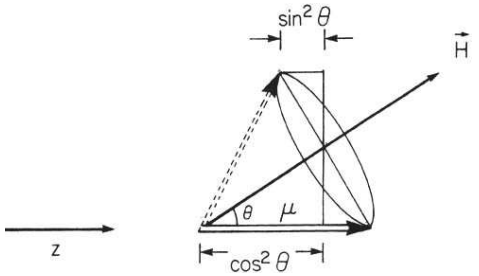

Figure 36: Larmor precession of a muon spin around a local magnetic field B_{loc} (H in figure); θ is the angle included between $\mathbf{z}$ and $\mathbf{B}_{loc}$. $\cos^2\theta$ is the projection factor for the time independent contribution to the muon polarization along $\mathbf{z}$, and $\sin^2\theta$ is the projection factor for the contribution precessing at the Larmor frequency.

moment $\sigma = \gamma\Delta B$, the directional average will lead Eq. 43 to the relaxation function

$$G(t) = \frac{1}{3}e^{-t/T_1} + \frac{2}{3}e^{-\sigma^2 t^2/2}\cos(\gamma_\mu B_{loc} t) \tag{44}$$

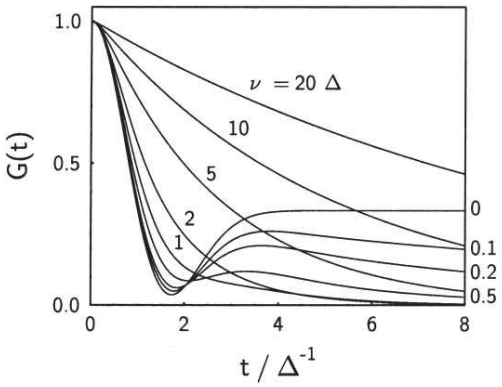

Figure 37: Static and dynamic Kubo-Toyabe relaxation function. The dynamic case is shown for several selected values of the correlation time τ, under the assumption of Gaussian random local fields [87], [86].

where in analogy to NMR language the time constant $1/T_1$ represents the rate of the dynamic spin-lattice relaxation, while the transverse relaxation rate σ arises from a static Gaussian inhomogeneous distribution. If the distribution $P^G(B)$ is centered at $B = 0$, (as an example this situation is suitably corresponding to the muon spin depolarization caused by nuclear dipolar fields), the zero field relaxation function is given by

$$G^G(t) = \frac{1}{3} + \frac{2}{3}(1 - \Delta^2 t^2)e^{-\frac{1}{2}\Delta^2 t^2} \tag{45}$$

which is known as the Kubo-Toyabe [86] static function. This function is represented by the $\nu = \tau^{-1} = 0$ curve in Fig. 37, where ν is the fluctuating rate, and Δ/γ_μ is the second moment of the field distribution. The Kubo-Toyabe may be seen as a Gaussian transverse overdamped component of amplitude 2/3 plus a longitudinal static component of amplitude 1/3. The amplitude of these two components reflect the average of the $\cos^2\theta$ and $\sin^2\theta$ terms of Eq. 43 over the entire solid angle.

Let us now consider the case of slow fluctuations, that is $\tau\Delta \gg 1$; this is the static case, so the muon spin relaxation function is the static Kubo-Toyabe previously treated. If local fields fluctuate slowly, with rate $\nu = 1/\tau < \Delta$, only the tail of $G(t)$, decays, with a rate close to ν. When ν becomes larger than Δ the initial Gaussian decay is affected, and the corresponding spectrum in the frequency domain becomes narrower ("Motional Narrowing"). This typically happens at high temperature, when motions become faster. Finally, at high enough temperature to insure the condition $\nu \gg \Delta$, the dynamic relaxation reduces to an exponential. These features can be derived in the strong collision approximation, which assumes a total loss of the memory of previous history at each fluctuation event. It is schematically shown in Fig. 38

A specially relevant case is the application of ZF-μSR to magnetically ordered materials. I restrict this description to the antiferromagnets as prototypes of magnetically ordered

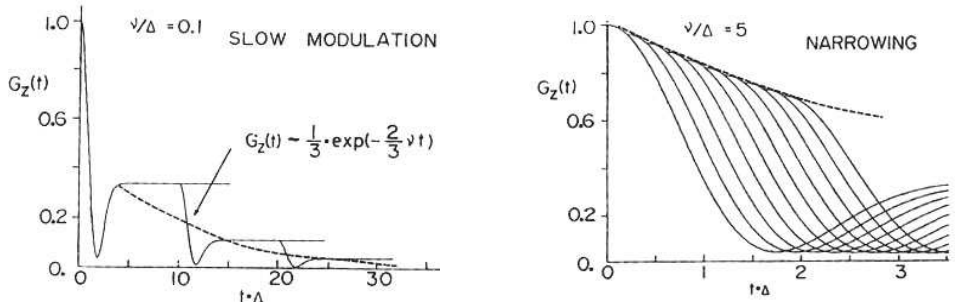

Figure 38: A schematic view of the time evolution of the average muon spin polarization in the Strong Collision Model for Gaussian random local fields. Left: for slow fluctuations $\nu < \Delta$ only the long time tail decays. Right: in the case of fast fluctuations $\nu \gg \Delta$ motional narrowing sets in [86].

materials with vanishing demagnetization fields. In these compounds, assuming a unique stopping site, the muon spin precesses around the spontaneous internal magnetic field B_i, which originates both from hyperfine contributions through spin polarized bonds to magnetic ions, and from distant electronic dipole moments. For a polycrystal the same distinction between longitudinal and transverse components of Eq. 45 applies with a ratio 0.5 between the two amplitudes.

4.2.5 The Bloembergen, Purcell and Pound relaxation model

A simple model of temperature dependent spin relaxation in NMR is due to Bloembergen, Purcell and Pound [88]. I will consider a similar situation adapted to the case of spontaneous internal field B_i in an antiferromagnet in a ZF-μSRexperiment. This is a special case of the relaxation introduced in Eq. 39. According to time dependent perturbation theory, a temperature dependent source of stochastic fluctuating fields perpendicular to the spontaneous B_i will act on the muon spin ensemble behaviour leading to a relaxation rate

$$\frac{1}{T_1} = \frac{\gamma^2 B_i^2 \tau}{1 + (\gamma B_i \tau)^2}. \tag{46}$$

A peculiar example of this relaxation mechanism is provided by the slowing down of the critical spin fluctuations, approaching a second order magnetic transition. The very large internal fields of the ordered phase start to appear as an instantaneous fluctuating field above the transition, and the correlation times increases as $T \to T_m$, yielding a rate (in Eq. 46) peaked at T_m.

Alternatively, supposing that the fluctuation arise from an activation process $\tau(T) = \tau_\infty e^{-\frac{T_a}{T}}$, Eq. 46 leads to a characteristic peak in the $\frac{1}{T_1}$, which takes place for $\tau(T_{peak}) = (\gamma B_i)^{-1}$.

4.3 Muons and superconductivity

Muon Spin Rotation (μSR) is particularly useful in dealing with type-II superconductors, where the Abrikosov vortex lattice is formed under an external field. The vortex lattice is incommensurate with the crystal lattice and, except in the very highest magnetic field regime, the vortex cores are separated by a larger distance than the unit cell dimension. Implanted muons sit at specific crystallographic sites and thus they sample randomly the field distribution of the vortex lattice. The Abrikosov lattice (see Sec. 1.5) is best investigated in

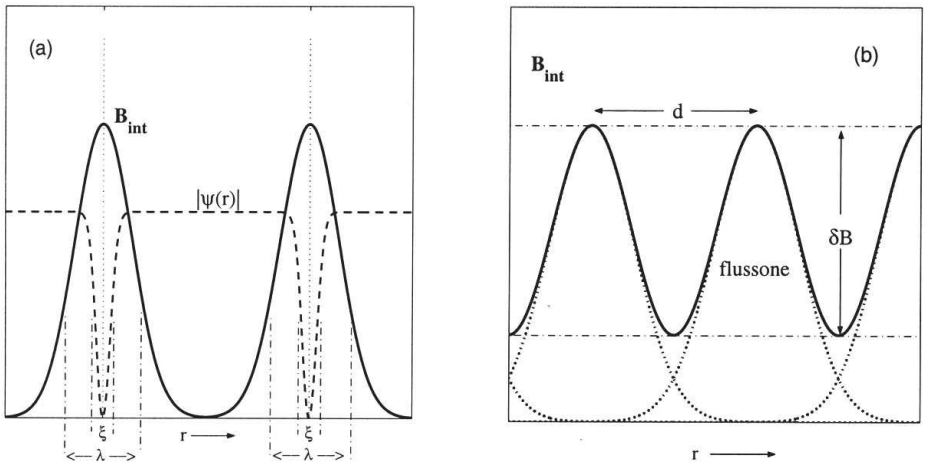

Figure 39: The spatial field distribution in a flux lattice of a superconductor in the mixed state: (a) $B_{ext} \sim B_{c1}$, the vortex lines do not overlapped. The superconducting order parameter $\psi(r)$ becomes zero in the vortex centers. (b) $B_{c1} \ll B_{ext} \ll B_{c2}$, vortices do overlap, and the flux lattice survives with a field contrast $\delta B = B_{max} - B_{min}$ [89].

TF-μSR. In the normal state ($T > T_c$) the external applied field penetrates uniformly the material and all muons precess with frequency $\omega_L = \gamma_\mu B$.

In the superconducting state ($T < T_c$) muons implanted close to the vortex cores experience a larger magnetic field than those implanted between vortices. Consequently there is a spread in precession frequencies, resulting in a decay of the observed precession signal; the larger the penetration depth, the smaller the magnetic field variation, and hence the decay. When $\kappa = \frac{\lambda}{\xi} \gg 1$ (as for the cuprates), the vortex core dimensions are not relevant up to very high vortex density, when the cores begin to overlap. For extreme type-II the spatial distribution of magnetic flux is determined only by λ.

The Fourier transform of the transverse depolarization function gives the muon precession frequency distribution, which coincides with the probability distribution $p(B)$ of the internal field values

$$p(B) = \frac{1}{v} \int_v d^3r \, \delta(|\mathbf{B}(\mathbf{r})| - B)) \tag{47}$$

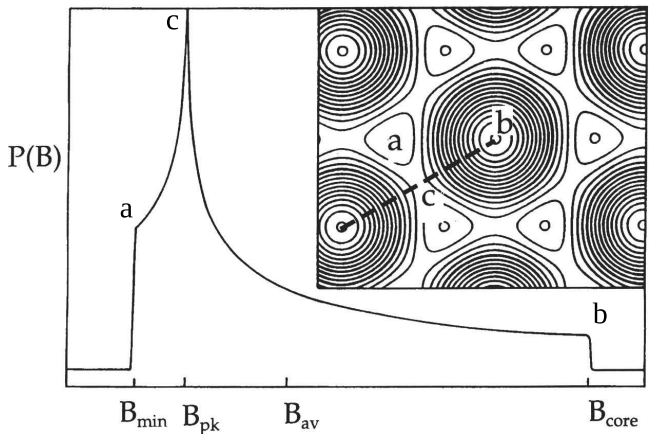

Figure 40: The internal field distribution $p(B)$ for a typical isotropic superconductor in the case of a triangular vortex lattice for large k; details vary depending on symmetry, and on the values of ξ, λ and a [89, 90].

Under typical Ginzburg-Landau approximations the shape of the function $p(B)$ is easily obtained by a numerical calculation [90] in the reciprocal space [91]; Fig. 40 shows a typical result for an ideal isotropic triangular lattice. Several distinctive features may be identified in this rather asymmetric line shape. A minimum field value $B \neq 0$ originates from the center of the cell ((a) in Fig. 40). The maximum field B_{max} corresponds to the vortex core, (b), and to a rather low weight $p(B)$ since the core region is small for large k. The sharp peak at a field $B_{pk} = B_s$ (s=saddlepoint), just little below the mean value $B_{av} = \langle B \rangle$ arises from the saddle point on the line connecting two vortex cores, (c). The precise details of the shape of $p(B)$ actually depend on the symmetry of the lattice (triangular or square) and on the values of ξ, λ ed a. In the experimental data the singularities of $p(B)$ are broadened by random vortex pinning which is represented by the convolution of $p(B)$ with a Gaussian lineshape.

$$p_{exp}(B) = \int \frac{1}{2\pi\sigma_d} e^{-\frac{1}{2}\left(\frac{B-B'}{\sigma_d}\right)^2} p(B)\mathrm{d}B' \tag{48}$$

where σ_d may be related to the root mean square displacement of a vortex line about its mean position. Such analysis has been successfully applied to studies of disorder in the moderate moderately anisotropic high T_c superconductor $YBa_2Cu_3O_{6+y}$ [92].
In polycrystalline cuprates this broadening is rather severe and the resulting lineshape reduces to a pure Gaussian whose relaxation parameter σ_μ is still dominated by the flux lineshape. In these conditions it is impossible to identify the additional effect of disorder, and measurements are affected by a systematic overestimation. Nevertheless, these measurements are perfectly suitable for comparative studies like ours.

For isotropic superconductors and for $B_{c1} < B_{ext} \ll B_{c2}$ the penetration depth can be directly obtained [93] from the muon relaxation parameter σ_μ, hence from the second moment

of the internal field distribution $p(B)$ as

$$\sigma_\mu = \gamma_\mu \sqrt{\langle \Delta B^2 \rangle} = \frac{1.072 \cdot 10^5}{\lambda^2} \tag{49}$$

where σ_μ (in μs^{-1}) and λ (in nm) are the zero temperature extrapolations of the corresponding quantities. Recalling that $\lambda^{-2} = \mu_0 e^2 n_s/m^*$, this provides a direct relation between σ and n_s. When the superconductor is anisotropic, (e.g. the effective mass tensor is has components $m_a = m_b \neq m_c$) the line shape of the second moment depend on the field orientation. For highly anisotropic SC like cuprates ($m_{a,b} \gg m_c$) the ab component of the penetration depth tensor ($\mathbf{B} \parallel \hat{c}$) dominates in the powder average, and the effective London penetration depth is estimated to be $\lambda_{eff} = 1.23\lambda_{ab}$. This results in $\sigma_\mu = 7.086 \cdot 10^4/\lambda_{ab}^2$.

The temperature dependence of $\sigma(T)$ and $\lambda(T)$ can be often described by the empirical formulas

$$\sigma(T) = \sigma(0)[1 - (\frac{T}{T_c})^\alpha], \quad T < T_c \tag{50}$$

$$\lambda(T) = \frac{\lambda(0)}{\sqrt{1 - (\frac{T}{T_c})^\alpha}}, \quad T < T_c \tag{51}$$

where α usually varies between 4 and 2 ($\alpha = 4$ is the prediction of the phenomenological two-fluids model [91]). Power laws are generic of a critical behaviour, where the order parameter vanishes at the critical point.

4.4 Pulsed ISIS muon source

Most of the experiments have been performed at the ISIS facility of the Rutherford Appleton Laboratory. In the following sections I will shortly analyze some proper ISIS facility characters. In the last one I will introduce μ-Lab, our software for data analysis.

4.4.1 Muon production, time structure and beam transport

The energy of the main proton beam at ISIS is ~ 800 MeV, that is about 3 times the production threshold. The pulses are generated in pairs, with a frequency of about 50 Hz; the two pulses of each pair are separated by 320 ns, while each short pulse is about 70 ns wide at half height (Full Width at the Half Maximum).

The target is a thin ($\sim 5mm$) pyrolytic graphite plate; it works at a proton beam current of $200 - 300\,\mu$A, corresponding to 160 Kw. Intercepting approximatively 5% of this power needs water cooling to operate at a temperature of about 800 K. The low Z number and the

specified thickness attenuate the proton beam intensity only by a factor ~ 0.1, not a relevant drop for the Spallation Target, which acts as Neutron Source placed downstream, so that $\sim 90\%$ of the beam continues towards a high Z target (typically tantalum) for the spallation process (the ISIS facility is the most powerful spallation neutron source in the world as well). Pions decaying at rest on the surface of the muon production target generate the surface muons, fully spin polarized, as discussed in Sec. 4.2.1. Near the surface a pair of quadrupole magnets collect muons emerging within a solid angle of about 0.13 srad.

Beam transport (dipole and quadrupole magnets) is optimized for 26Mev/c momentum particles to guarantee nearly monochromatic muons. A velocity selector discriminates these particles by mass to eliminate pions and positrons of equal momentum. Many of the latter would otherwise be transported to the sample, providing spurious triggers in the detectors. The muon beam is characterized by a temporal structure that reflects that of the protons convoluted with the pion decay ($\tau_\pi \sim 26$ ns) to produce a slightly asymmetric pulse of full width ~ 80 ns. The muon energy is ~ 3.05 MeV instead of the calculated 4.2 MeV, because of the stopping effect of the thin vacuum windows between the primary proton and the secondary muon beam. The beam current is $\sim 170\,\mu$A, that is a flux of about $2 \cdot 10^5 \mu^+/s$.

An electrostatic kicker is responsible for subdividing the beam among three instruments. Inside the kicker the first of the two beam pulses is spatially split in two, by a central electrode at very high voltage. This kicks half the pulse to the left and half to the right, feeding the two side beamlines (EMU and DEVA). In the time between the two muon pulses the voltage on the electrode is reduced to zero, and the second pulse travels undeflected to the MuSR area.

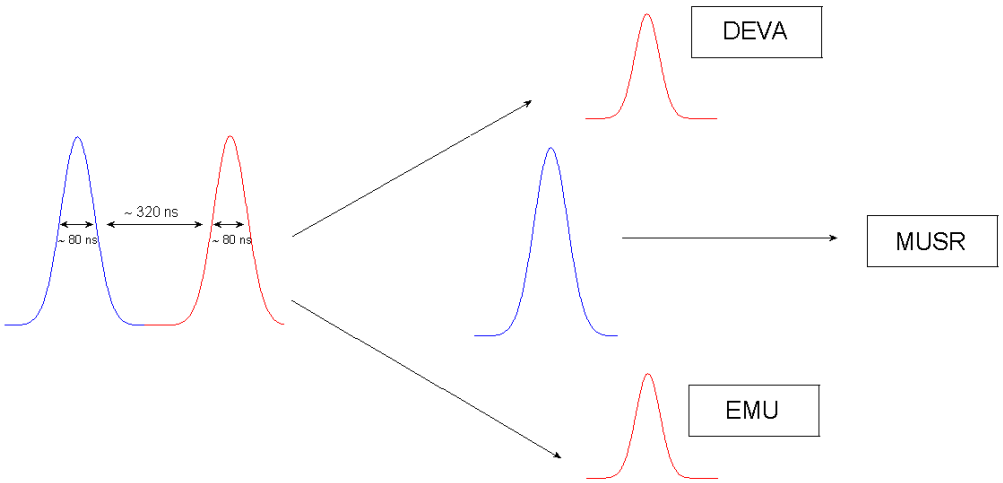

Figure 41: The muon beam time structure and the operation of the kicker. Two short pulses (for simplicity represented as two Gaussians with FWHM ~ 80 ns) are separated by ~ 320 ns. The kicker splits in two the first (red) pulse, and feeds the two side beamlines EMU and DEVA. The second (blue) pulse travels undisturbed toward the MuSR spectrometer.

The timing signal for the kicker is provided by a lead glass Cerenkov counter located near the muon production target. The kicker is essential since the spread of the beam time structure has a profound influence on the measurable frequency spectrum. Without the kicker the width would be dominated by the large burst separation (320 ns), whereas with the single burst is reduced to 1/4. The passband of a square beam of width $\Delta t = 80$ ns is simply the Fourier transform of this double step, that is $sin(\nu\Delta t/2)/(\nu\Delta t/2)$. This factor reduces the measured asymmetry to zero at $\nu = 12.5$ MHz, In practice with the actual beam an upper limit to the measurable local fields is about 600 G, corresponding to an asymmetry reduction from 1 to 0.25 at $\nu = 8$ Mhz.

Summarizing, with a beam time structure characterized a pulse width τ_1 and a pulse repetition period τ_2, requires that $\tau_1 << \tau_{\mu^+} << \tau_2$, where τ_1 is the pulse width, τ_{μ^+} the muon life-time, τ_2 the reciprocal of the frequency of pulse repetition. In our case $\tau_1 = 70$ ns, $\tau_{\mu^+} = 2.2\,\mu$s, $\tau_2 = 20$ ms, so the relation above is verified. The other constraint is an upper limit to local fields of about 600 G.

4.4.2 Revealing and recording $e+$ events

Most experiments were run on the MuSR spectrometer at the ISIS facility. Some details of this spectrometers follow.
64 plastic scintillator detectors are arranged around the sample, covering a solid angle of $\sim$ 20%, and connected with as many photomultipliers by light guides. The positron revealing takes place symmetrically respect to the starting muon polarization; moreover the whole apparatus must satisfy some practical aspects, such as the presence of Helmotz coils and a cryostat housing; so the final setting is strongly dependent on a number of versatility requirements. The muon burst indirectly triggers the timing start signal in the Cerenkov detector. A detected positron provides the stop signal. The time elapsed is digitalized and one count is added to the corresponding memory location which records both time and detector label. An experimental data set from the MuSR spectrometer is formed by 64 histograms (one per detector); each histogram contains 2000 time bins each corresponding to 16 ns, for a total of 32 μs, equal to $\sim 15\tau_\mu$. However incorrelated background counts (corresponding to 10^{-5} times those at $t = 0$) start to influence the data after 24μs $\sim 11\tau_\mu$. Pulsed muon detection has another limitation: many positrons ($\sim 200 e^+/burst$) must be detected over a few muon lifetimes. The typical detector dead-time τ_m for which it is insensitive after a recorded event is $\sim$ 75 ns. For an incident positron rate $n(t)$, the measured rate $n_{obs}(t)$ is easily calculated by Poisson statistics [89] as

$$n_{obs}(t) = \frac{n(t)}{1 + n(t)\tau_m} \tag{52}$$

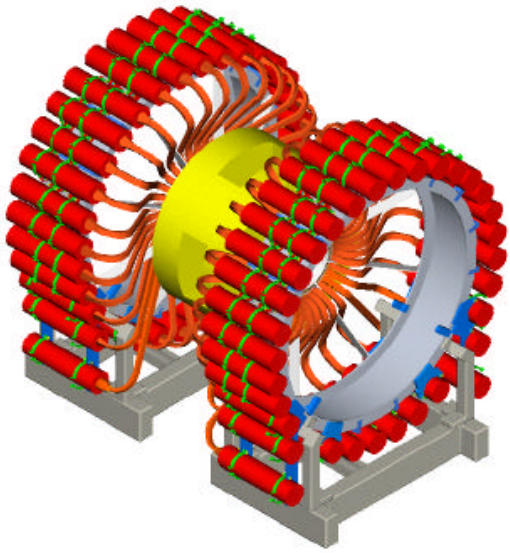

Figure 42: The events counted by the 1 to 64 positrons detectors on the MUSR spectrometer, arranged into two arrays, can be combined in the more appropriate configuration, depending on the experimental setup (ZF or TF).

so that $n(t)\tau_m \ll 1$ is the requirement for a negligible miscount rate. If for instance we allow a maximum miscount of 10%, we must fix $(N/\tau_\mu)\tau_m \leq 0.1$, i.e. $N \leq 220/75 \approx 3$ events per detector per burst. To grant this condition a large number of small detectors must be employed. With 200 events/burst, 64 detectors provide the required event rate per detector. The events can be subsequently recalculated by software, combining the detectors in the more appropriate configuration, depending on the type of experiment.

4.4.3 Data analysis: μ-Zen and μ-Lab

The software utilized for the data analysis have been μ-Zen (by G. Guidi, R.De Renzi and G. Allodi) and μ-Lab (by R.De Renzi and G. Allodi). The former runs on linux, and is now outperformed by and latter, that is a matlab tool running both on linux and on windows. Both μ-Zen and μ-Lab allow the analysis of the data recorded on the EMU and MUSR spectrometers (ISIS facility) and on the LTF and GPS spectrometers (LMU facility) by choosing the correct set up for the instrument. From the fit menu main window data loading, fit function selection, saving and reloading, fit execution, plotting, fft of residues and saving of results can be chosen. Free download and instructions can be found at the webpage http://www.fis.unipr.it/ derenzi/dispense/pmwiki.php?n=MuSR.Mulab.

Both μ-Zen and μ-Lab are based on MINUIT, a powerful algorithm that working on chisquare functions computes the best-fit parameter values and uncertainties of a multi-parameter function, including correlations. MINUIT has been originally written [94] by F. James and

M. Roosat at CERN. From this original version successive improvements by G. Allodi lead to the actual version implemented in μ-Lab. More informations can be found at the CERN webpage http://wwwasdoc.web.cern.ch/wwwasdoc/minuit/minmain.html.

Chapter 5

Experimental Results

In this section I present the experimental results of my thesis work. The first four sections regard the samples, which I mostly produced myself, starting from their solid state synthesis, their structural and compositional characterizations by diffraction techniques, the thermopower determination of the hole density transferred to the CuO_2 plane, and the SQUID measurement of T_c. I have already reported a summary table of all the compounds in Tab.2 (see Sec.1.4). The last section contains the main results of three groups of μSR experimental runs, that form the core of this thesis work (a fourth one will be written up afterward). The μSR section is subdivided in four subsections, devoted respectively to: the ZF muon data analysis, with the relation between the local muon field and the Cu magnetic moment in the magnetically ordered phases; the ZF results on magnetism in lightly doped, clean-limit Y100%, YEu8% and YNd7.5% [95]; the corresponding results in dirty-limit Ca- substituted samples [37,96]; finally, the TF results on the underdoped superconductors, in the clean and dirty limit [47]. The discussion of Ch. 6 is organized along the same line.

5.1 Sample preparation

The sample preparation has been carried on in the high-temperature synthesis laboratory of our Physics Department. The polycrystalline samples have been synthesized by using the standard solid state reactions (see, for example, [97, 98, 99]). The best conditions have been obtained after several preliminary tests, by changing the grinding time of reagents, the dwell temperatures, the warming/cooling rates, the oxygen flux. Standard diffraction, transport and magnetic characterizations lead to define a standard protocol, but different solubility limits and thermodynamics of the Y substituents (Eu, Nd and Ca) turned out in slightly different best synthesis conditions. Moreover differences are sometimes present when utilizing nominally equivalent reagents from different suppliers. Some others differences we had to take into account in the process standardization concerned the fact that nominally

equivalent ovens are actually slightly different.
In the following of this chapter is presented a better description of the main steps involved in the preparation of $Y_{1-x}R_xBa_2Cu_3O_{6+y}$, (R=Eu, Nd, Ca), that starts from the chemical reagents listed with their own purity in Tab. 3.

Reagent	**Declared Purity**
Y_2O_3	99.999%
Eu_2O_3	99.999%
Nd_2O_3	99.999%
CuO	99.995%
$BaCO_3$	99.997%
$CaCO_3$	99.995%

Table 3: The starting reagents for the synthesis of polycrystalline $Y_{1-x}R_xBa_2Cu_3O_{6+y}$, (R=Eu, Nd, Ca) and their relative declared purities.

Weighting and grinding.
Stoichiometric quantities of the appropriate reagents are weighted on a digital scale which sensitivity is equal to 10^{-6} g. Starting from about 10 g of powders reagents results into 20 small bars 0.43 g each, thus during the whole preparation process there is a waste of about 15% of the initial mass, mainly due to the CO_2 emitted by the decomposition of carbonates. The weighting is performed under nitrogen atmosphere; the yttrium oxide, such as many other oxides, is very hygroscopic, and the total absence of humidity ensures the correct stoichiometry. The reagents are then milled inside a 45 ml agate bowl with ten agate balls of 1 cm of diameter by using a PULVERISETTE 7 ball mill which guarantees both an homogeneous mixing of the reagents, and a final grain size of about 1 μm, maximizing the reacting surfaces. The optimal milling speed and total time are obtained by performing short consecutive millings at increasing speed rate. Small differences were noted between wet (ethanol) and dry milling; being the latter more convenient under several practical points of view all our samples have been prepared by dry milling.

Synthesis cycles.
The obtained powder is then pressed at about 0.9 GPa to form small bars of about $3 \times 5 \times 25\, mm^3$ and $2.4\, g$ each, which now undergo an high temperature synthesis process in a tubular oven with automatic temperature control. The synthesis process consists of a controlled heating up to the desired dwell temperature, followed by a variable dwell time. The last synthesis step is the cooling to room temperature that can be spontaneous, controlled, or very quick (quenching); A scheme of the steps involved in this process is shown in the left

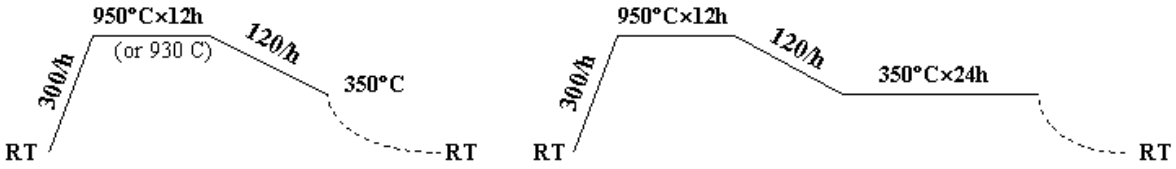

Figure 43: Left side: synthesis protocol. It consists in a controlled warming at a 300° C/ hour up to the dwell temperature, 950° for the parent compound and the Eu and Nd substituted series and 930° C for the Ca substituted series, which is held for 12 hours; then a cooling rate of 120° C/ hour leads the system to 350° C, and a spontaneous cooling to room temperature follows. Right side: sintering protocol. The dwell temperature is 950° C, and the dwell time at 350° C is 24 hours; a spontaneous cooling to room temperature follows. Both the treatments are performed under a quite consistent oxygen flux (~ 0.5 l/min)

side of Fig. 43. The chemical reactions that take place in the synthesis process are shown in Eq. 53 for R=(Eu,Nd) and in Eq. 54 for R=Ca; the reaction for the pure $YBa_2Cu_3O_{6+y}$ is obtained in both of them simply by substituting $x = 0$.

$$(1-x)Y_2O_3 + xR_2O_3 + 4BaCO_3 + 6CuO + \frac{1}{2}O_2 \longrightarrow \\ \longrightarrow 2\,Y_{1-x}R_xBa_2Cu_3O_7 + 4CO_2. \tag{53}$$

$$(1-x)Y_2O_3 + 2xCaCO_3 + 4BaCO_3 + 6CuO + \frac{1+x}{2}O_2 \longrightarrow \\ \longrightarrow 2\,Y_{1-x}Ca_xBa_2Cu_3O_7 + 2(x+2)CO_2. \tag{54}$$

The extra oxygen in the previous formulas is required to promote the solid state reaction [100], and is supplied by performing the synthesis under an oxygen flow of 0.5 l/m. Experimentally we note that the best conditions for the reaction of Eq. 53 are achieved at $T = 950K$, while for the reaction of Eq. 54 $T = 935K$ is the more appropriate temperature. After this thermal cycle the pellets are milled and pressed again and the entire synthesis protocol is repeated once more to ensure that the decomposition of staring carbonate (calcination process) is fully achieved. After this process the original mechanical mixture has become a desired stoichiometry single phase of $Y_{1-x}R_xBa_2Cu_3O_{6+y}$ (R=Eu, Nd, Ca), with purity greater than 99%, as confirmed by Neutron Scattering (see Fig. 52 in Sec. 5.2) and reported in [47].

Sintering.

After the synthesis the pellets are milled again and pressed at about 1.1 GPa into bars of $0.42g$ and $2 \times 3 \times 12\,mm^3$. The final thermal treatment involves two dwell temperatures (right side of Fig. 43); the higher one (950° C) promotes the sintering process, that is the aggregation of smaller size grains into a bigger size grain (nucleation) and the partial compenetration of different grains, optimizing the morphological properties of this ceramic material. The lower dwell temperature (350° C) allows the reordering and homogenization of the chain oxygen.

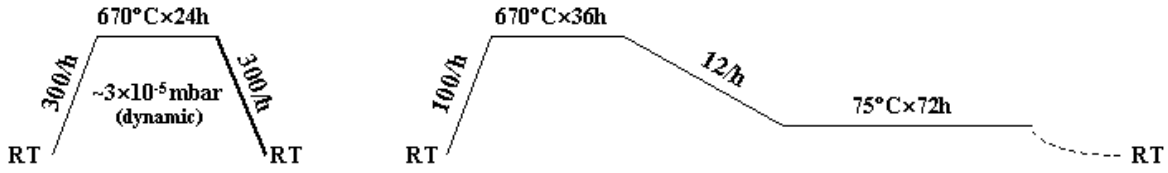

Figure 44: Sketches of the reduction (left) and equilibration (right) protocols. The reduction takes place under a dynamic vacuum of about $1.7 \cdot 10^{-7}$ bar at $670°$ C, that is the temperature that maximizes the oxygen mobility; it turns out in a fully reduced samples series with $y = 0.05(2)$. The oxygen equilibration between the two end members takes place at the same temperature as well, while the long $75°$ C temperature annealing stabilizes the oxygen ordering.

Reduction.

After the sintering we obtain fully oxidized samples, that is $y \sim 1$ in the chemical formula; after a subsequent iodometric titration [47], we are able to carefully evaluate the exact oxygen content within an error of 1%. A part of the obtained samples undergoes the basal plane oxygen depletion thanks to the thermal process shown in the left side of Fig. 44. This treatment is performed under dynamic vacuum, at a pressure of about $1.7 \cdot 10^{-7}$ bar. Now two sample series are available: the first one composed by fully oxidized samples $y = 0.98(1)$, and the second one by fully reduced $y = 0.05(1)$.

Oxygen equilibration.

This is an ad-hoc technique developed by Prof. Manca *et al.* [101]; it consists in the oxygen equilibration of stoichiometric quantities of the two end members $y = 0.05(1)$ and $y = 0.98(1)$, tightly packed in a vessel that is sealed under vacuum; the final oxygen content will be obtained following the simple relation

$$y = \frac{0.98(1) \cdot m_1 + 0.05(1) \cdot m_2}{m_1 + m_2}. \tag{55}$$

During the high temperature step of the thermal process described in Fig. (44) the reduced samples will be the oxygen "acceptors", while the fully oxidized samples will be the "donors"; then a slow cooling and a long low temperature annealing yield high quality homogeneous samples of the desired oxygen stoichiometry with an absolute error $\delta x = \pm 0.02$, reduced to $\delta x = \pm 0.01$ after recalibrating end members of different batches. Besides this determination, the absolute oxygen content is cross-checked by iodometric titration, thermogravimetry on each sample, and selected neutron Rietveld refinements [47]. The overall process leads to a very high reproducibility and homogeneity we especially need when treating with stoichiometries close to the insulating-superconducting transition, where the competition among different ground states is very sensitive to inhomogeneity and defects. In order to preserve the quality of the samples, since $YBa_2Cu_30_{6+y}$ is very sensitive to humidity and carbon dioxide in air [102], the pellets have to be stored in desiccators. Finally in Fig. 2, Sec. 1.4 I report

a legend that associates each chemical formula with a conventional label that for simplicity will be used in the following.

5.2 Crystallographic analysis

The crystallographic analysis has been accomplished by Rietveld refinements of x-rays diffraction patterns to roughly check the phase purity and to measure the lattice parameters. A crystallographic information file (.cif) provide to the software all the required structural items; this file is based on the informations collected in the *International Tables for Crystallography*. We performed neutron diffraction experiments on several selected samples to determine the actual stoichiometry of both cation substitutions and oxygen; sizeable differences between nominal and real values have been found only in the Ca substituted compounds at large Ca content (an example is reported in Fig. 52 at the end of this section). In the following I will refer to the real stoichiometry of the samples. As previously pointed out the x-ray analysis have been systematically performed during each step of the synthesis, then on the final, oxygen-equalized samples; some selected results and quantitative evaluations are dis-

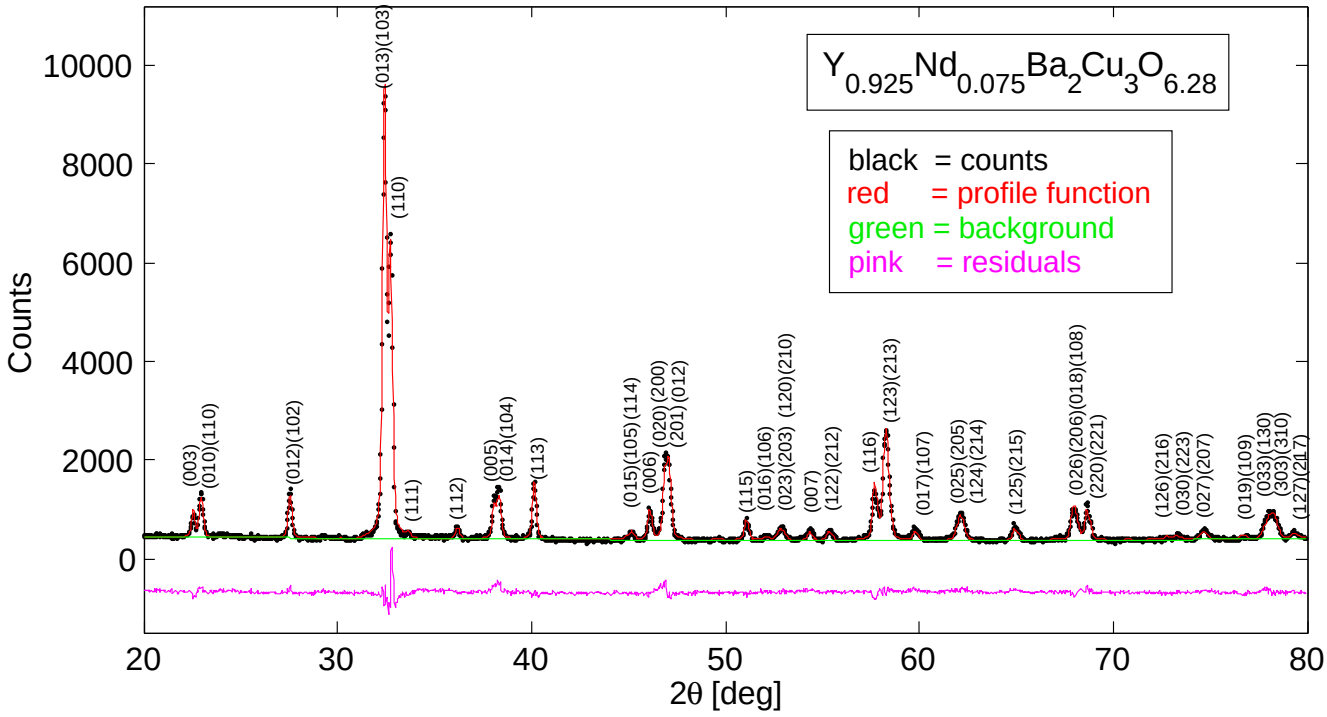

Figure 45: $Y_{0.925}Nd_{0.075}Ba_2Cu_3O_{6.28}$ powder x-ray diffraction pattern (black spots) and the associated profile function (red line), as calculated by the Rietveld refinement. The absence of not indexed peaks confirms the purity of the phase.

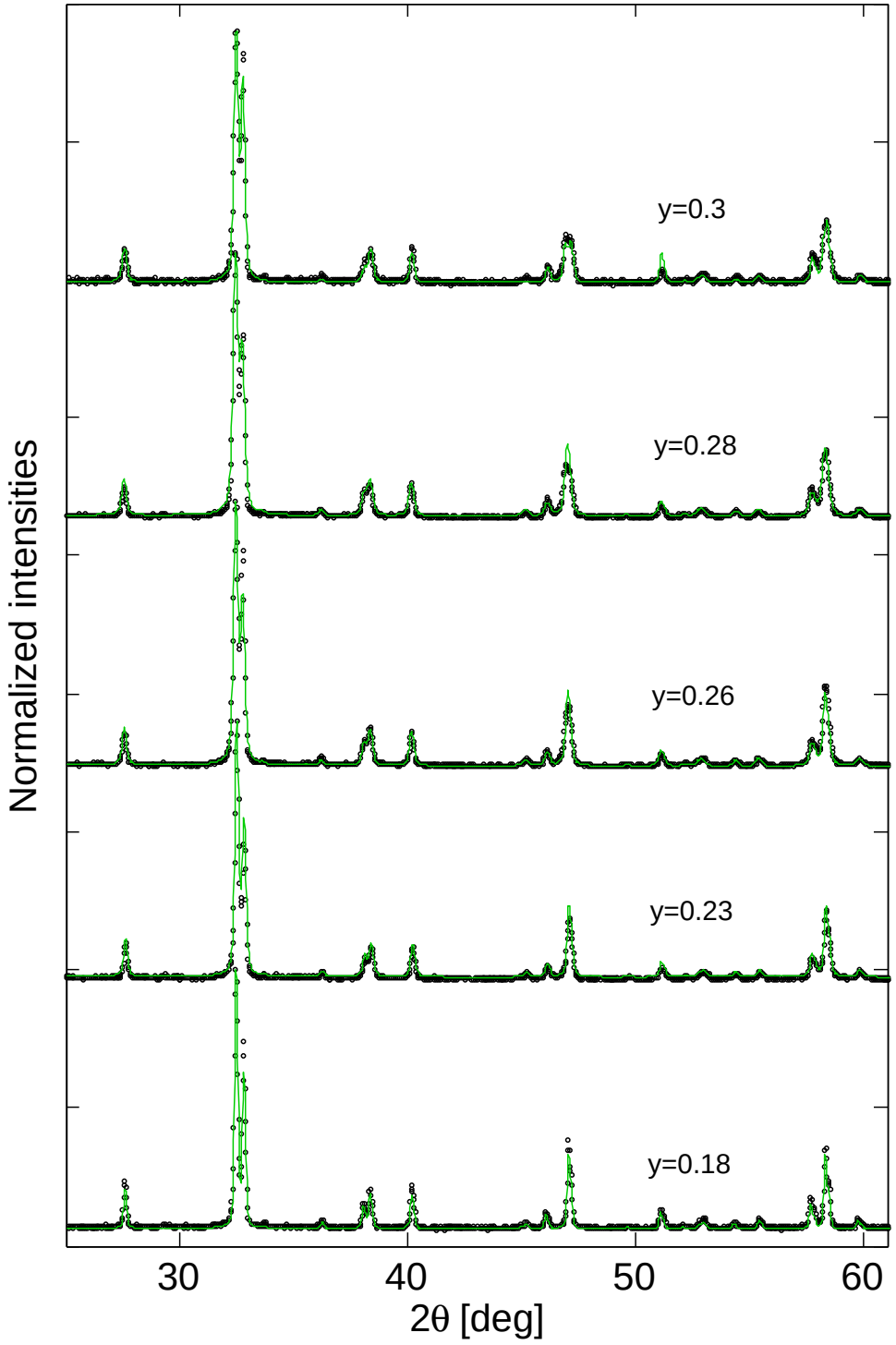

Figure 46: The x-ray pattern (black) and the best profile functions (green) for the $Y_{0.925}Nd_{0.075}Ba_2Cu_3O_{6+y}$ series, from bottom to top for increasing oxygen content ($0.18 \leq y \leq 0.3$). Symmetry space group for the tethragonal structure: P 4/M M M

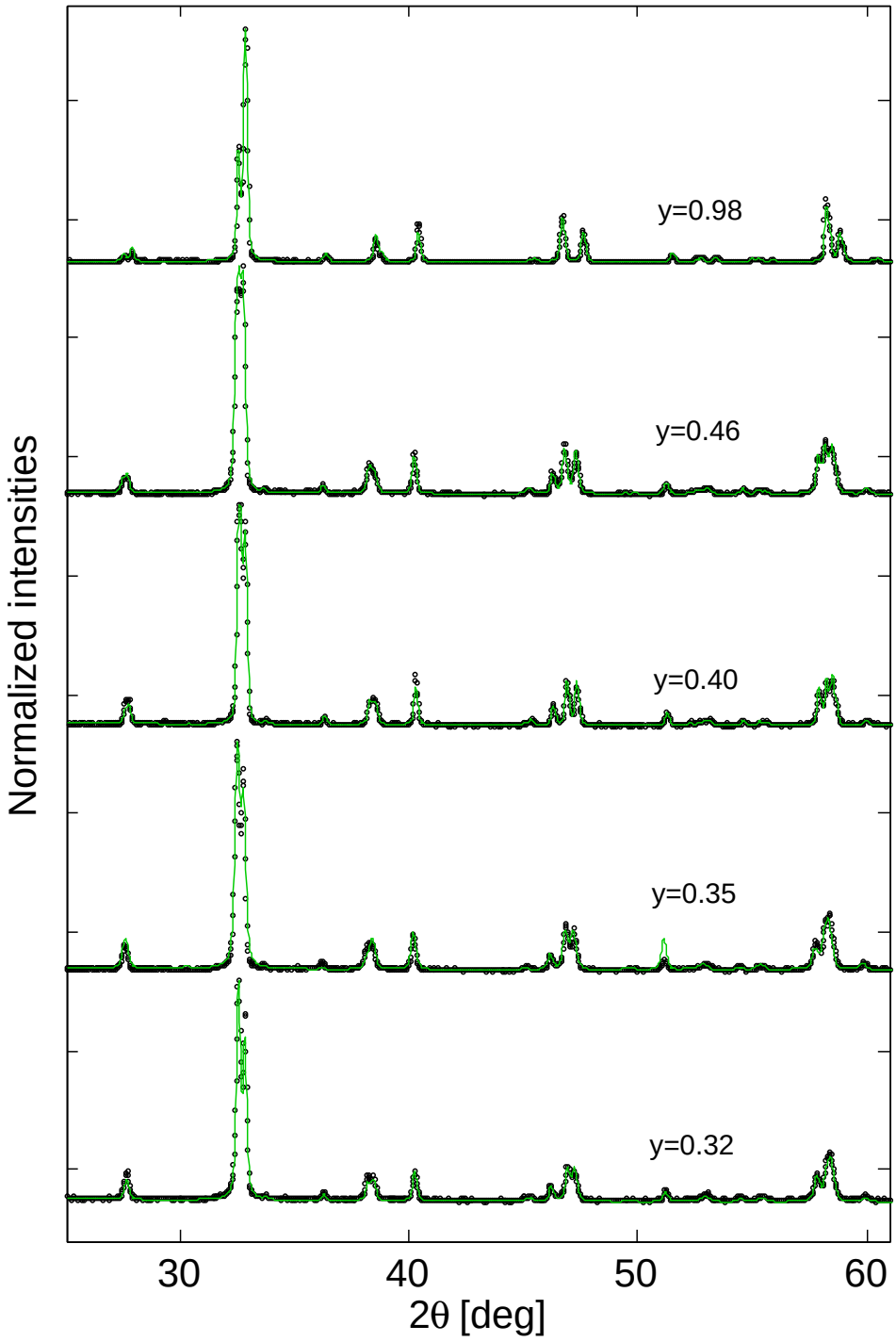

Figure 47: The x-ray pattern (black) and the best profile functions (green) for the $Y_{0.925}Nd_{0.075}$-$Ba_2Cu_3O_{6+y}$ series, from bottom to top for increasing oxygen content ($0.32 \leq y \leq 0.98$). Symmetry space group for the orthorhombic structure: P M M M

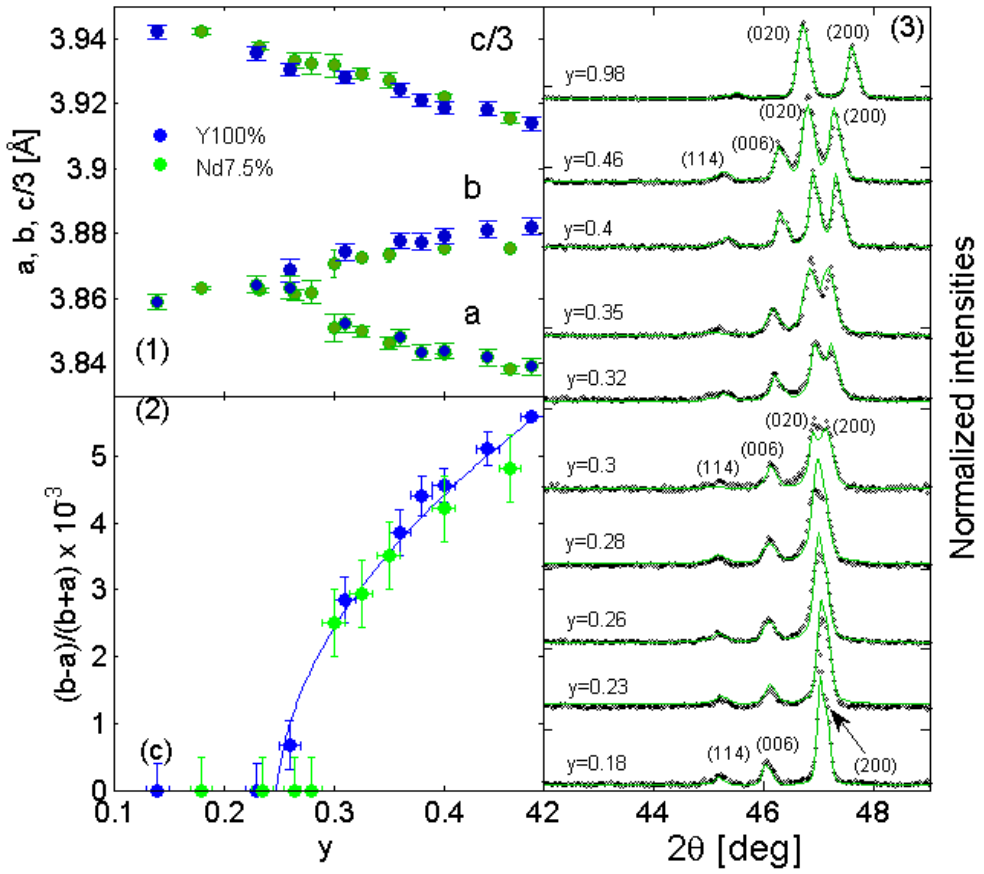

Figure 48: The Y100% (blue) and Nd7.5% (green) series. (1): oxygen dependent splitting of the a and b lattice parameters at $y_c = 0.28(2)$. (2): orthorhombic distortion (3): a detail of the profile functions of Figs. 46 and 47 where is evident the splitting of the (020)-(200) peaks for increasing y content, characteristic of the **T**→ **O** transition.

cussed here. In Fig. 45 the powder x-ray spectrum of $Y_{0.925}Nd_{0.075}Ba_2Cu_3O_{6.28}$ is shown; black dots are the raw data, and the red curve is the fitted profile function. All the peaks belong to the reflections of the YBCO crystal structure, excluding the presence of sizeable amount of impurity phases. More examples for the Nd7.5% series are reported in Figs. 46 and 47. From the Rietveld analysis the cell parameters have been determined for all of the samples, except for the Eu8% series, which has been measured to check the phase purity only. In Fig. 48(1) the evolution of a, b, and b with oxygen doping is shown for the two series Y100% and YNd7.5%, as determined by the slight variation of the peaks positions. It is possible to identify a critical oxygen content ($y_c = 0.28(2)$) corresponding to the tethragonal to orthorhombic transition (**T**→ **O**) of the structure; y_c can be qualitatively identified for the YNd7.5% series by observing the evolution of the diffraction peaks (020)-(200) (the more sensitive to this structural change) reported in panel (3); this latter panel is the zoom in the region $42° \leq 2\theta \leq 50°$ of Figs. 46 and 47. Panel (2) shows the orthorhombic distor-

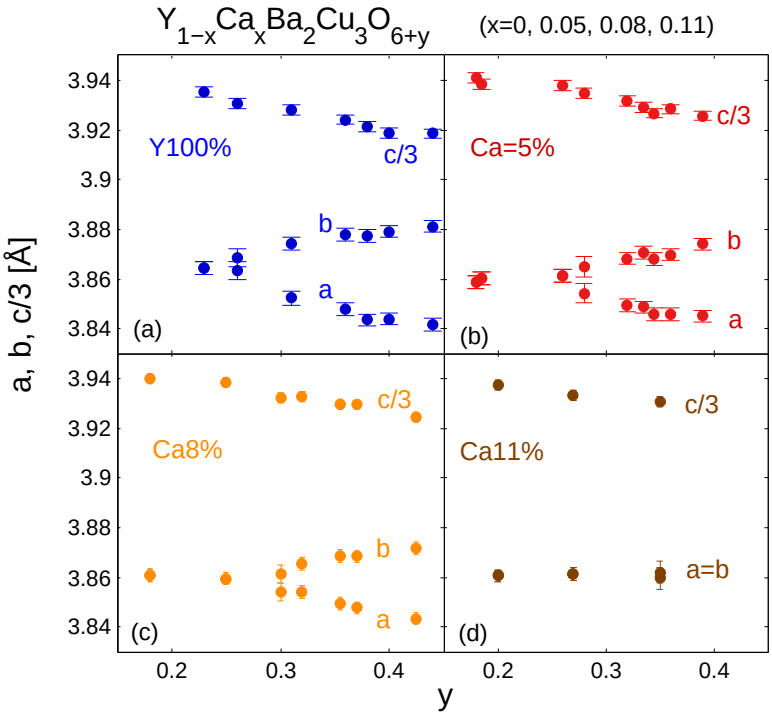

Figure 49: Evolution of the lattice parameters of $Y_{1-x}Ca_xBa_2Cu_3O_{6+y}$ for increasing Ca substitutions (i.e. Y100%, Ca5%, Ca8%, Ca11% shown respectively in panel a, b, c, and d, versus oxygen doping.

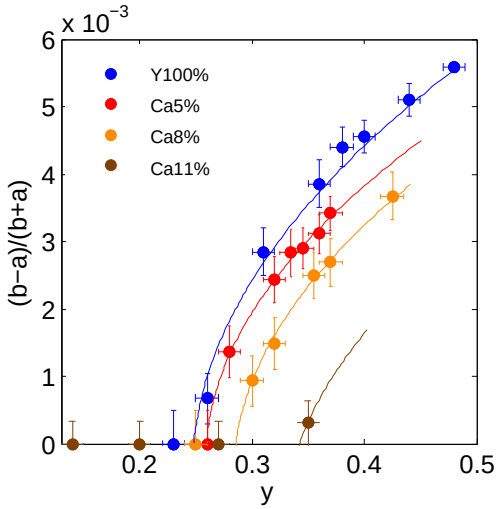

Figure 50: Orthorhombic distortion (b-a)/(b+a) of the samples of Fig. 49. The colored lines, guides to the eye, are clearly right-shifted with respect to the Y100% values (blue).

tion $(b-a)/(b+a)$, directly calculated from the data of panel (1): significant differences between the two series both in panel (1) and (2) are not present. The values of a,b, and c and their errors are resumed in the tables of Fig. 53. The tethragonal-to-orthorhombic (**T**→ **O**) transition is clearly associated with oxygen doping; as soon as the oxygen chains reach a critical length (along the b direction), corresponding in the Y100% structure to a critical oxygen stoichiometry, the unit cell becomes orthorhombic, while the c axis gets shorter about linearly with a small change of the slope of $c(y)$ across the transition. The decreasing of c is strictly associated with the decreasing of the bond distance Cu(1)-O(1), that is the distance between the copper of the CuO chain and the apical oxygen in position (0,0,± z). Let us now focus on the Ca-substituted samples whose lattice parameters are plotted in Fig. 49. Panel (a),(b),(c), and (d) correspond respectively to the series Y100% (parent compound), Ca5%, Ca8% and Ca11%. The orthorhombic distortion as a function of the oxygen content is displayed in Fig. 50 for all of the Ca families. The data clearly show that the critical oxygen content y_c for the **T**→ **O** transition increases by adding Ca, i.e. the presence of Ca hampers the formation of ordered chains along the b direction, in agreement with previous results [103].

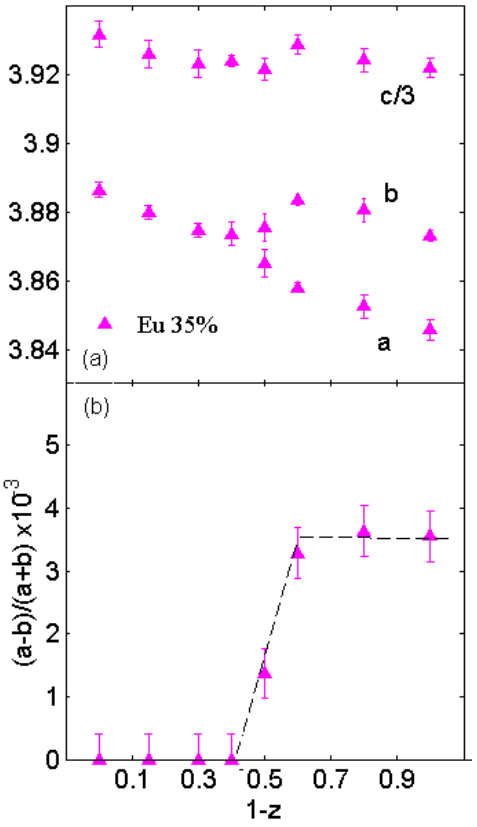

Figure 51: Calculated lattice parameters (a) and orthorhombic distortion (b) of the Eu35% series. A **T**→ **O** transition takes place at $z \approx 0.5$.

Let us finally focus on the Eu35% series; its lattice parameters and the orthorhombic distortion, as a function of the Y content $1-z$ are presented respectively in Fig. 51(a and b). The data show that this series with a fixed oxygen content y=0.35(1) displays a **T**→ **O** transition for $z_c \sim 0.45$. If compared to Figs. 48 and 49, the main difference is the presence of a negative slope in the evolution of the lattice parameters a and b.

A possible explanation of the plot could be the following: at fixed oxygen content the Y100% structure ($1-z=1$) is orthorhombic, being the $y=0.35(1)$ well above the required oxygen content for the system to be orthorhombic ($y_c = 0.28(2)$ determined by Fig. 48). The insertion of Eu stabilize the tetragonal structure, like the case of Ca discussed above. Cu-NQR experiments, providing informations about the oxygen ordering [104], have been performed on the end term $1-z=0$ and 1 of this series, to determine the Cu-O chain length ℓ . The results [105] give $\ell = 13$ for the orthorhombic sample ($1-z=1$) and $\ell = 3$ for the tetragonal one ($1-z=0$), evidencing that the oxygen ordering is strongly influenced by the cation substituted in the Y site. The different chain length of in pure and Y-substituted compounds underlines the importance of an independent calibration of the hole density for each family of materials. This was achieved by thermopower measurements (see Fig. 54c).

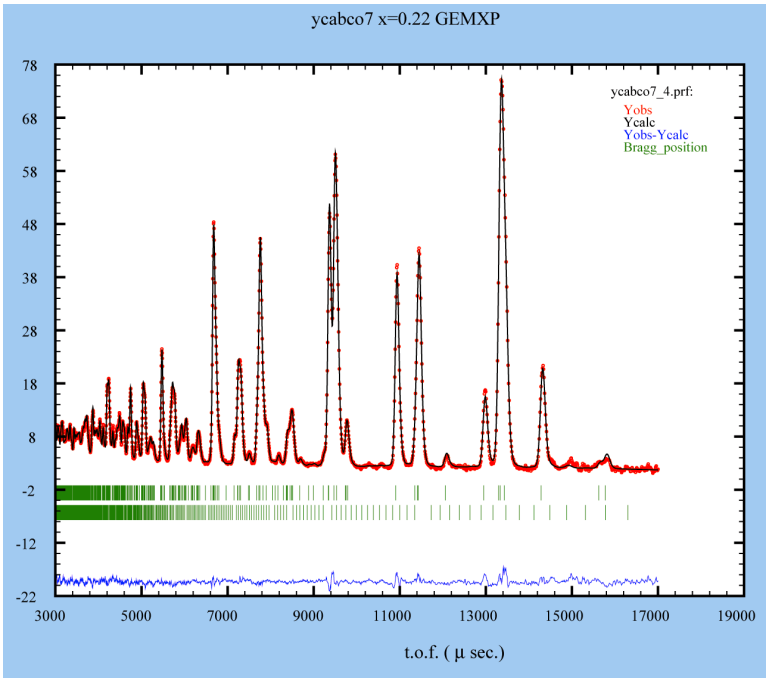

Figure 52: The time of flight neutron diffraction pattern for a sample of the series Ca18% (nominal Ca concentration: 22%). Both the $Y_{1-x}Ca_yBa_2Cu_3O_6$and the $BaCuO_3$ phases (the competing one) are fitted; the latter results in an amount less than 1%.

Series	y	a(Å)	b(Å)	c(Å)	(b-a)/(b+a)
Ca5%	0.18	3.859(1)	3.859(1)	11.823(3)	0.0000(3)
Ca5%	0.185	3.860(1)	3.860(1)	11.815(4)	0.0000(3)
Ca5%	0.26	3.861(2)	3.861(2)	11.814(4)	0.0000(4)
Ca5%	0.26	3.856(3)	3.865(3)	11.812(6)	0.0011(5)
Ca5%	0.28	3.854(3)	3.865(3)	11.804(6)	0.0014(5)
Ca5%	0.32	3.849(3)	3.868(3)	11.795(6)	0.0024(5)
Ca5%	0.335	3.849(2)	3.871(2)	11.787(5)	0.0028(4)
Ca5%	0.345	3.846(2)	3.868(2)	11.78(4)	0.0029(4)
Ca5%	0.36	3.846(1)	3.861(1)	11.785(4)	0.0031(3)
Ca5%	0.39	3.845(1)	3.874(1)	11.777(4)	0.0037(3)
Ca5%	0.98	3.821(1)	3.882(1)	11.678(3)	0.0079(3)

Series	y	a(Å)	b(Å)	c(Å)	(b-a)/(b+a)
Ca8%	0.18	3.861(3)	3.861(3)	11.821(3)	0.0000(3)
Ca8%	0.25	3.860(3)	3.860(3)	11.815(3)	0.0000(3)
Ca8%	0.3	3.854(7)	3.861(7)	11.797(5)	0.0009(5)
Ca8%	0.32	3.854(5)	3.866(5)	11.798(5)	0.0015(5)
Ca8%	0.355	3.849(4)	3.869(4)	11.789(5)	0.0025(5)
Ca8%	0.37	3.848(4)	3.869(4)	11.788(4)	0.0027(5)
Ca8%	0.425	3.843(3)	3.872(3)	11.773(4)	0.0037(4)

Series	y	a(Å)	b(Å)	c(Å)	(b-a)/(b+a)
Ca11%	0.03	3.859(1)	3.859(1)	11.828(3)	0.000(4)
Ca11%	0.14	3.861(1)	3.861(1)	11.823(3)	0.000(4)
Ca11%	0.2	3.861(2)	3.861(2)	11.812(3)	0.000(4)
Ca11%	0.27	3.861(2)	3.861(2)	11.801(3)	0.000(4)
Ca11%	0.35	3.861(2)	3.861(2)	11.792(3)	0.000(4)
Ca11%	0.35	3.862(1)	3.860(1)	11.792(3)	0.0003(4)

Series	y	a(Å)	b(Å)	c(Å)	(b-a)/(b+a)
Y100%	0.23	3.8643(7)	3.8643(7)	11.826(2)	0.0000(2)
Y100%	0.26	3.8634(7)	3.8686(7)	11.811(2)	0.0007(3)
Y100%	0.31	3.8523(8)	3.8743(7)	11.804(4)	0.0028(3)
Y100%	0.36	3.8480(8)	3.8778(8)	11.792(5)	0.0039(3)
Y100%	0.38	3.8435(9)	3.8775(9)	11.783(4)	0.0044(2)
Y100%	0.4	3.8439(7)	3.8791(7)	11.776(3)	0.0046(2)
Y100%	0.44	3.8418(6)	3.8812(6)	11.775(2)	0.0051(2)
Y100%	0.48	3.8390(6)	3.8821(6)	11.761(2)	0.0056(1)

Series	y	a(Å)	b(Å)	c(Å)	(b-a)/(b+a)
Nd7.5%	0.18	3.863(1)	3.863(1)	11.827(3)	0.0000(5)
Nd7.5%	0.235	3.862(1)	3.862(1)	11.813(3)	0.0000(5)
Nd7.5%	0.265	3.861(2)	3.861(2)	11.800(7)	0.0000(5)
Nd7.5%	0.28	3.862(3)	3.862(3)	11.798(9)	0.0000(6)
Nd7.5%	0.3	3.851(4)	3.871(4)	11.795(9)	0.0025(6)
Nd7.5%	0.325	3.850(2)	3.873(2)	11.788(5)	0.0029(5)
Nd7.5%	0.35	3.847(2)	3.873(2)	11.782(5)	0.0035(5)
Nd7.5%	0.4	3.843(2)	3.876(2)	11.766(5)	0.0042(5)
Nd7.5%	0.46	3.838(1)	3.875(1)	11.747(4)	0.0048(5)
Nd7.5%	0.98	3.815(1)	3.882(1)	11.665(3)	0.0087(5)

Series	z	a(Å)	b(Å)	c(Å)	(b-a)/(b+a)
Eu35%	1	3.886(2)	3.886(2)	11.796(9)	0
Eu35%	0.85	3.880(2)	3.880(2)	11.779(8)	0
Eu35%	0.7	3.875(2)	3.875(2)	11.770(9)	0
Eu35%	0.6	3.874(1)	3.874(1)	11.772(5)	0
Eu35%	0.5	3.865(3)	3.876(3)	11.765(7)	0.0014(4)
Eu35%	0.4	3.859(3)	3.884(2)	11.787(7)	0.0033(4)
Eu35%	0.2	3.853(3)	3.88(2)	11.773(9)	0.0036(4)
Eu35%	0	3.846(2)	3.873(2)	11.766(8)	0.0034(4)

Figure 53: Summary table of the values of the lattice parameters of the samples reported in Figs. 48, 49 and 51, as extracted from the XRD-Rietveld analysis.

5.3 Thermopower results

The Seebeck coefficient is an independent measure of the mobile carrier content, since an exponential dependence of $S(290\ \mathrm{K})$ vs h is observed in $YBa_2Cu_3O_{6+y}$ [75, 74]. We systematically measured the value of S at room temperature (RT) $T = 290$ K, calibrating the dependence on for the fully reduced compounds, $y \approx 0$. For these samples the h contribution from chain oxygen is nearly zero; we therefore assumed an average hole content per Cu plane $h = h_{Ca} = x/2$. We identify two regions as in a previous work, [75] and our best fit to

$$S^{RT}(h) = \alpha \cdot exp(-\beta h) \tag{56}$$

shown in Fig. 54a, yields values of $\alpha = 480\mu$V/K and $\beta = 25$ for the $h \geq 0.016$ and $\alpha = 650\mu$V/K and $\beta = 44$ for $h \leq 0.016$. Panel b shares the y scale with panel c, and shows the h values obtained for all of our series, by comparing their RT Seebeck coefficient S with the calibration curve of panel a. Notice that in the entire range of oxygen content explored in this work, $0.05 \leq y \leq 0.42$, the Cu(1)O(1) chains do not produce [106] a normal metal contribution to the thermopower, hence the measured hole density is located in the CuO_2 layers.

As already anticipated in Sec. 1.1, Fig. 54b shows the well known fact that oxygen does not contribute to hole transfer up to $y_t \approx 0.12 \div 0.15$, since below this threshold oxygen concentration, only locally charge-neutral Cu(1)O Cu(1) dimers are formed [107], while above y_t hole doping increases almost linearly with y, as oxygen ions start forming negatively charged trimers. Secondly it is clear that the Eu or Nd substitutions do not alter the oxygen transfer efficiency of holes, because the blue, green and pink data all collapse on the same curve. Moreover, despite the small slope reduction for higher calcium contents, the common linear behaviour of $h(y)$ proves the fact that the oxygen doping mechanism remains nearly the same. Confirmations of the validity of the hole determination by TP come from bond valence sum analysis (BVS) [73, 108], and from chemical estimations of the Cu formal valency based on titration techniques [109].

In panel (c) the hole content for the series Eu35% is plotted; the step-like function at

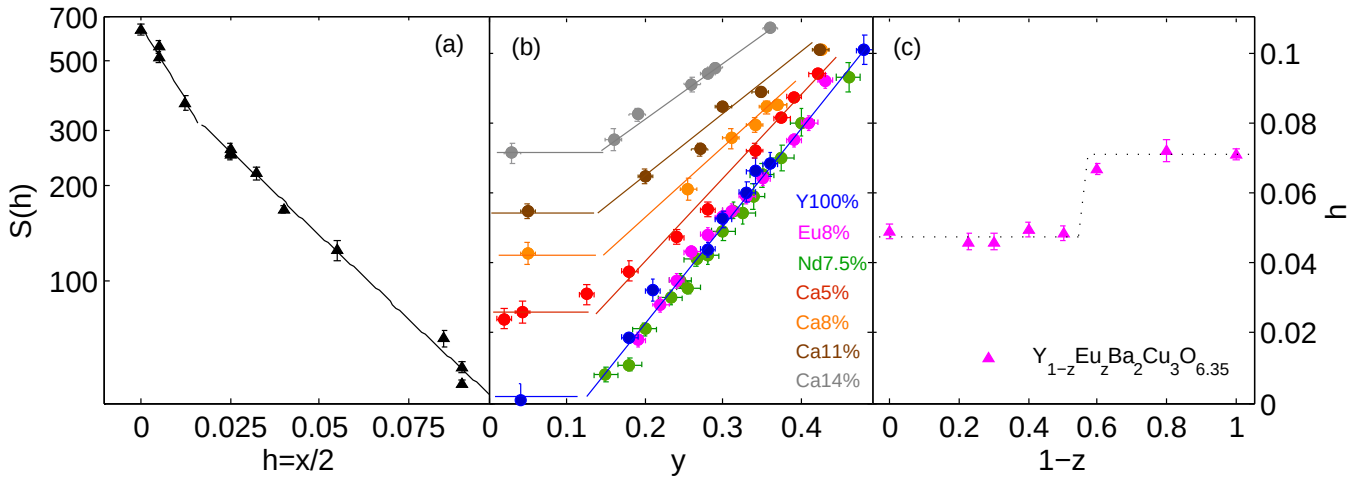

Figure 54: Hole content determination. (a) Calibration of holes h per CuO_2 layer from thermopower S at $T = 290$ K for the fully reduced samples $Y_{1-x}Ca_xBa_2Cu_3O_6$. The lines are the best fits from Eq. 56. (b) Hole content for $Y_{1-x}A_xBa_2Cu_3O_{6+y}$ A=Ca, Eu, Nd and (c) $Y_{1-z}Eu_zBa_2Cu_3O_{6.35}$ as a function of oxygen y and yttrium content $1-z$ respectively.

$0.4 \leq 1 - z \leq 0.6$ shows an abrupt change in the hole content, nearly corresponding to the **T**→ **O** transition of Fig. 51, while apart from the discontinuity value it seems not altered by the Europium substitution, even at very high stoichiometry, up to $z = 1$; the step corresponds to $\Delta h \approx 0.02$.

The determination of the hole doping of the $YBa_2Cu_3O_{6+y}$ compound has been a tricky task for many years. In order to asses the validity of our calibration, in Fig. 55 the hole content of the Y100% and Nd7.5% series as a function of the c crystallographic axis is compared with the data from a recent calibration of the pure $YBa_2Cu_3O_{6+y}$ by Liang et al [110]. The latter is a phenomenological relation between the hole content and the c axis. The excellent agreement between these two indipendet calibrations confirms the reliability of our results. It is noteworthing that no sizeable differences are found between the Y100%, Eu7.5% and Nd8% series on both the $h(y)$ and $h(c)$ from Fig. 54b and 55 respectively. This indicates that the presence of small quantity of isovalent cations substituents negligibly affect both the chain oxygen hole doping efficiency and the structure. Conversely a sizeable influence is observed for small amount of heterovalent substitutions in Figs. 54b and 50, and for much higher isovalent substitutions in the $Y_{1-z}Eu_zBa_2Cu_3O_{6.35}$ in Figs. 54c and 51.

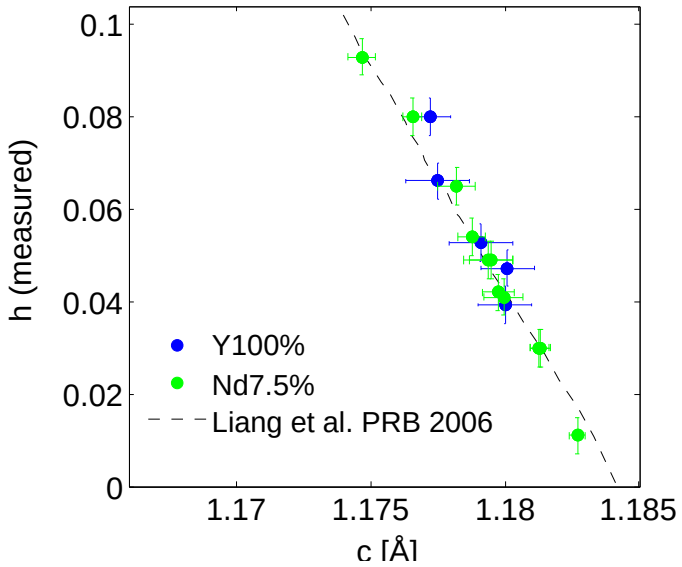

Figure 55: Comparison between two indipendent h calibrations for $YBa_2Cu_3O_{6+y}$. Blue and green dots (Y100% and Nd7.5% respectively) are from our XRD analysis and $S(h)$ calibration, the dashed line from an independent calibration [110].

The thermopower data and the corresponding hole doping values are reported in the following tables.

Sample Name	x [Ca]	h=x/2	S(muV/K))	eS(muV/K))
y89-7	0	0	630	26
yc26-10	0.01	0.005	558	22
yc25-11	0.01	0.005	515	16
yc20-14	0.025	0.0125	368	19
yc21-14	0.05	0.025	257	10
yc23-14	0.05	0.025	263	11
yc22-13	0.05	0.025	252	10
yc31-14	0.065	0.0325	220	10
yc27-13	0.08	0.04	168	5
yc32-13	0.11	0.055	125	9
yc34-2	0.17	0.085	66	4
yc40-6	0.18	0.09	47	1
yc36-2	0.18	0.09	53	2

Series	Sample name	y (oxygen)	z [Eu]	S(h)[uV/K]	h (S)	eh(S)
Eu35%	eu10-6	0.35(1)	1	141	0.049	0.002
Eu35%	ye 14-2	0.34(1)	0.77	162	0.043	0.002
Eu35%	ye 14-15	0.35(1)	0.77	142	0.049	0.002
Eu35%	ye5-7	0.35(1)	0.70	131	0.052	0.003
Eu35%	ye 17-7	0.34(1)	0.60	157	0.045	0.002
Eu35%	ye 17-16	0.35(1)	0.60	126	0.054	0.003
Eu35%	ye 18-15	0.34(1)	0.50	151	0.046	0.002
Eu35%	ye 18-16	0.35(1)	0.50	136	0.051	0.003
Eu35%	ye6-7	0.35(1)	0.40	91	0.067	0.003
Eu35%	ye4-7	0.35(1)	0.20	82	0.071	0.003
Eu35%	y90-4	0.35(1)	0	82	0.071	0.003

Figure 56: Top panel: calibration data defing the $S(h)$ dependence plotted in Fig. 54(a). Bottom panel: $S(h)$ measurements and h calculation from formula 56 (with α and β specified above) for the Eu35% series

Series	Sample name	equalization	y	S(h)[uV/K]	h (S)	eh(S)
Ca1%	yc25-11	deox	0.03	515	0.005	0.001
Ca1%	yc26-10	deox	0.06	558	0.003	0.001
Ca1%	yc24-2/3	G6int22	0.22	234	0.029	0.003
Ca1%	yc38-5/6	P2int29	0.29	187	0.038	0.003
Ca1%	yc24-13	G7dis35	0.34	89	0.068	0.003
Ca1%	yc24-10	G5int39	0.38	69	0.079	0.004

Series	Sample name	equalization	y	S(h)[uV/K]	h (S)	eh(S)
Ca5%	yc23-14	deox	0.03	263.40	0.024	0.001
Ca5%	yc21-14	deox	0.05	256.90	0.025	0.001
Ca5%	yc22-13	deox	0.04	252.00	0.026	0.001
Ca5%	yc21-3	F1int15	0.13	220.80	0.032	0.001
Ca5%	yc22-2	F4int18	0.18	192.70	0.037	0.001
Ca5%	yc21-8	F2int21	0.19	188.30	0.038	0.001
Ca5%	yc23-5	G2dis28	0.28	123.90	0.055	0.003
Ca5%	yc23-8	G3int32	0.32	104.20	0.062	0.002
Ca5%	yc21-11	F3int37	0.35	86.50	0.070	0.003
Ca5%	yc18-7	D2int36	0.34	80.70	0.072	0.003
Ca5%	yc23-18	G4dis36	0.36	74.40	0.076	0.003
Ca5%	yc18-4	D4dis40	0.38	65.40	0.081	0.003
Ca5%	yc10-6	D3int39	0.39	55.70	0.087	0.003
Ca5%	yc10-8/9	D5int42	0.42	47.50	0.094	0.003

Series	Sample name	equalization	y	S(h)[uV/K]	h (S)	eh(S)
Ca8%	yc27-13	deox	0.05	168	0.043	0.001
Ca8%	yc28-3	I1int27	0.26	107	0.061	0.002
Ca8%	yc27-5	I3int34	0.32	77	0.074	0.003
Ca8%	yc28-5	I2int31	0.3	71	0.078	0.001
Ca8%	yc28-10	I5int38.5	0.37	64	0.082	0.002
Ca8%	yc28-9	I4int36.5	0.36	59	0.085	0.003
Ca8%	yc27-16	I5dis38.5	0.37	59	0.085	0.003
Ca8%	yc27-9/10	I6int44.5	0.43	39	0.101	0.003

Ca11%	yc27-13	deox	0.04	168	0.043	0.002
Ca11%	yc32-3	M5int28	0.2	95	0.066	0.002
Ca11%	yc32-16	M6dis35	0.27	81	0.072	0.002
Ca11%	yc32-7	M6int35	0.27	81	0.072	0.002
Ca11%	yc32-15	N1int38	0.3	60	0.085	0.002
Ca11%	yc32-14	N2int42	0.34	54	0.089	0.002

Series	Sample name	equalization	y	S(h)[uV/K]	h (S)	eh(S)
Ca14%	yc33-3	deox	0.03	82.7	0.071	0.002
Ca14%	yc33-4	O1int23	0.16	75.2	0.075	0.001
Ca14%	yc33-7	O2int26	0.20	63.1	0.082	0.002
Ca14%	yc33-9	O3int33	0.26	50.9	0.091	0.002
Ca14%	yc33-14	O5int35	0.29	45.3	0.096	0.002
Ca14%	yc33-15	O6int43	0.36	34.3	0.107	0.004

Series	Sample name	equalization	y	S(h)[uV/K]	h (S)	eh(S)
Y100%	y89-7deox	y89-7deox	0.05	630	0.001	0.001
Y100%	at2int20	at2int20	0.18	304	0.019	0.002
Y100%	q2int23	q2int23	0.21	218	0.032	0.002
Y100%	bfint30	bfint30	0.28	163	0.044	0.002
Y100%	aq1dis32	aq1dis32	0.3	132	0.052	0.003
Y100%	ap1dis35	ap1dis35	0.33	109	0.060	0.003
Y100%	bp1int37	bp1int37	0.34	94	0.066	0.003
Y100%	bt1int40	bt1int40	0.36	69	0.079	0.004
Y100%	bc1int41	bc1int41	0.4	57	0.086	0.004
Y100%	ag3dis50	ag3dis50	0.48	40	0.101	0.004

Series	Sample name	equalization	y	S(h)[uV/K]	h (S)	eh(S)
Nd7.5%	yn1-4	deox	0.05	419	0.009	0.001
Nd7.5%	yn1-9	B1int15	0.15	461	0.008	0.001
Nd7.5%	yn1-12	B2int18	0.18	394	0.011	0.001
Nd7.5%	yn1-15	B3int19	0.20	283	0.021	0.001
Nd7.5%	yn1-18	B4int22	0.23	292	0.020	0.001
Nd7.5%	yn3-10	C1int23	0.23	226	0.030	0.001
Nd7.5%	yn2-6	B5int24	0.25	202	0.035	0.001
Nd7.5%	yn3-12	C2int26	0.26	210	0.033	0.001
Nd7.5%	yn1-21	B6int26	0.27	171	0.041	0.001
Nd7.5%	yn2-9	B7int28	0.28	166	0.042	0.001
Nd7.5%	yn2-12	B8int30	0.30	142	0.049	0.002
Nd7.5%	yn4-6	C3int31	0.31	122	0.055	0.003
Nd7.5%	yn2-15	B9int32	0.33	123	0.054	0.003
Nd7.5%	yn4-9	C4int33	0.34	109	0.059	0.002
Nd7.5%	yn3-21	B10dis35	0.35	94	0.065	0.003
Nd7.5%	yn2-21	B11int38	0.38	84	0.070	0.003
Nd7.5%	yn3-7	B12int40	0.40	66	0.080	0.004
Nd7.5%	yn2-5	Adis46	0.46	47	0.093	0.004

Series	Sample name	equalization	y	S(h)[uV/K]	h (S)	eh(S)
Eu8%	ye29-3	deox	0.02	438	0.009	0.001
Eu8%	ye31-19	deox	0.02	368	0.013	0.001
Eu8%	ye31-8	deox	0.07	389	0.012	0.001
Eu8%	ye24-5	C1int19	0.19	306	0.018	0.001
Eu8%	ye31-10	E2int22	0.22	238	0.028	0.001
Eu8%	ye26-5	D1int24	0.24	202	0.035	0.001
Eu8%	ye26-8	D2int26	0.26	162	0.043	0.001
Eu8%	ye26-11	D3int28	0.28	146	0.048	0.003
Eu8%	ye24-8	C2int30	0.30	126	0.053	0.002
Eu8%	ye31-17	E5int31	0.31	121	0.055	0.003
Eu8%	ye26-14	D4int32	0.33	111	0.059	0.003
Eu8%	ye24-11	C3int35	0.35	96	0.064	0.003
Eu8%	ye24-14	C4int39	0.39	74	0.075	0.003
Eu8%	ye24-17	C5int41	0.41	65	0.080	0.003
Eu8%	ye30-17	E6dis43	0.43	48	0.092	0.003

Figure 57: $S(h)$ measurements and h calculation from formula 56 (with α and β specified above) for the Y100%, Nd7.5%, Eu8%, Ca1%, Ca5%, Ca8%, Ca11%, and Ca14% series.

5.4 SQUID Magnetometry

The superconducting transition temperatures T_c have been extracted from susceptibility measurements in a field equal to 2Oe, well below the critical field for the disruption of the full Meissner regime, H_{c1}, of the order of several tens of Oe for underdoperd cuprates. In the following sections I report some examples of different magnetometric measurements that it is possible to perform, and I show why we chose the Zero Field Cooling measurement on bulk samples as a standard in evaluating T_c.

5.4.1 Zero Field Cooling and Field Cooling measurements

The typical SQUID measurements have been carried out by both Zero Field Cooling (ZFC) and Field Cooling (FC) procedures. In ZFC (red circles in Fig. 58) the sample is first cooled in zero field, a field H turned on, and then data collected on warming. In FC (black squares in Fig. 58) the data are collected as the sample is cooled in the same field. The two curves merge into a common reversible behaviour only above a characteristic field dependent temperature T_i, called irreversibility temperature, below which the vortex liquid of flux quanta developing in FC is pinned by impurities into a vortex lattice. In order to reduce the flux pinning we used a low field of 2 Oe.

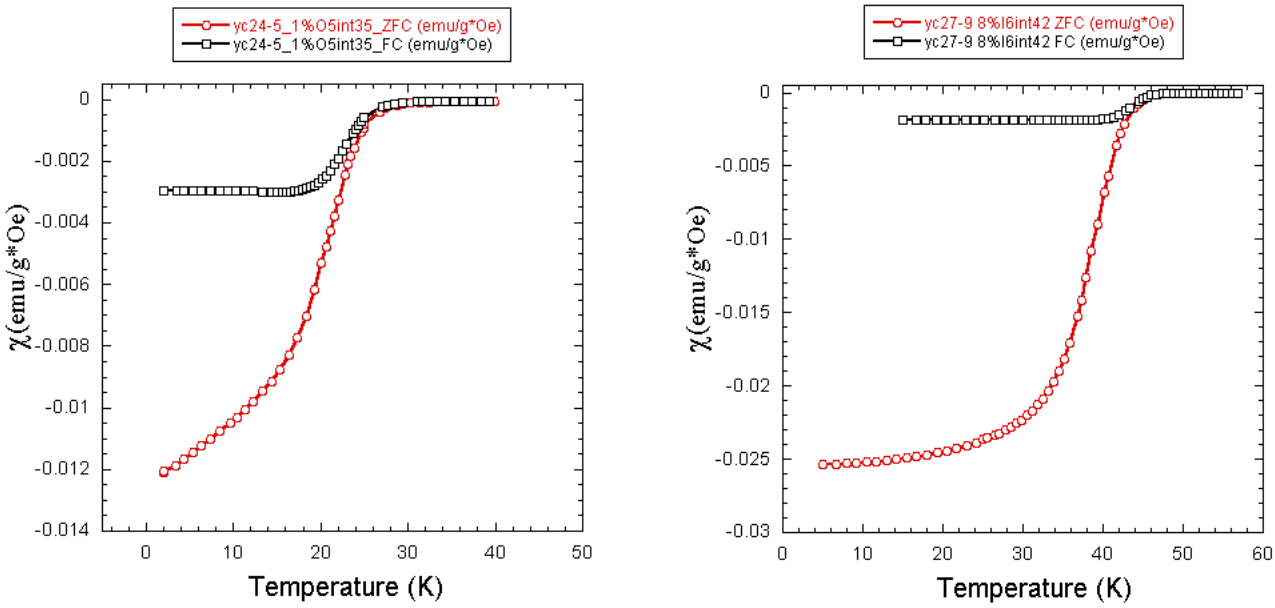

Figure 58: ZFC (red, circles) and FC (black, squares) bulk magnetic susceptibility versus temperature of the oxygen-intercalated sample (see Sec. 5.1) Ca1%, y=0.35 (left panel) and Ca8%, y=0.44 (right panel) for an applied field H=2Oe The legend reports the following tags: sample name, percentage of cationic substitution, number of equalization, final oxygen content.

Let me refer to the right panel of Fig. 58 to better explain the physical meaning of this measure. The low temperature points in the ZFC curve correspond to the maximum (modulus) of the susceptibility value, due to the shielding effect of the supercurrents developed on the surface of the sample. Below 30 K the susceptibility is nearly constant, implying that the supercurrents that prevent the penetration of the external field are also constant, that is the whole material has completed its transition to the superconducting regime. For increasing temperatures the steep slope of $\chi(T)$ is determined by the disruption of the collective state that originates the supercurrents, accompanied by the field penetration inside the bulk. The finite width of the transition toward the normal, paramagnetic state, is here mostly determinated by the intrinsic inhomogeneities of the material, which set a local distribution of transition temperatures. The paramagnetic susceptibility of the normal state is very weak with respect to the diamagnetic shielding, and can't be observed on such a scale.
Upon cooling, the Meissner effect takes place. Cuprates show a very strong flux-pinning, that is the pinning of vortices at short length scale inhomogeneities, that represent energetically favorable sites. This behaviour determines a reduced value of the FC zero temperature susceptibility, displayed by all the reported examples in Figs. 58 and 61. The T_c evaluation can result slightly different (from 1 to 5 K) when extracted from the ZFC or the FC curve. Our

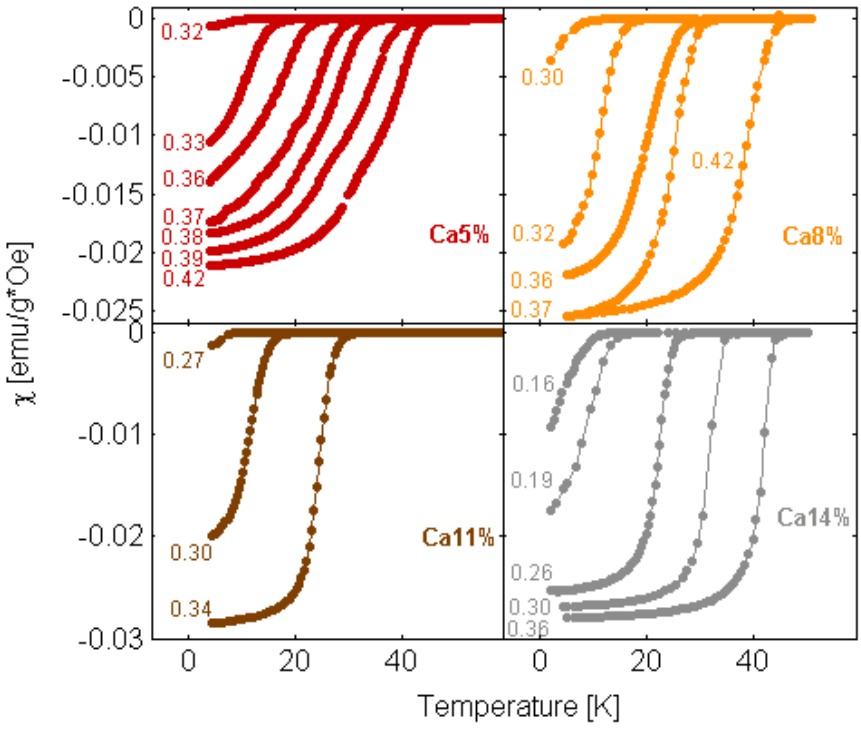

Figure 59: Examples of χ(T) ZFC bulk measurements on the samples of the Ca5% Ca8%, Ca11% and Ca14% series. Applied field: 2Oe. The number that accompanies each curve is the oxygen stoichiometry y.

criterion in determining the T_c has been to refer to the ZFC bulk measurements, for which the pinning is absent. In Fig. 59 I report some instances regarding the Ca5%, Ca8%, Ca11% and Ca14% series. The number that accompanies each curve is the oxygen stoichiometry y.

5.4.2 Intercalated and disintercalated samples

In Fig. 60 each panel display the comparison of the ZFC susceptibility curves for the intercalated and disintercalated samples of the same vessel (see Sec. 5.1). The data show a difference of T_c up to 4-5 K. The different T_c is most probably caused by a different oxygen ordering related to the kinetic path of the oxygen exchange between the acceptor and donor sample [101]. Since the acceptor one does generally display the higher T_c, in the following

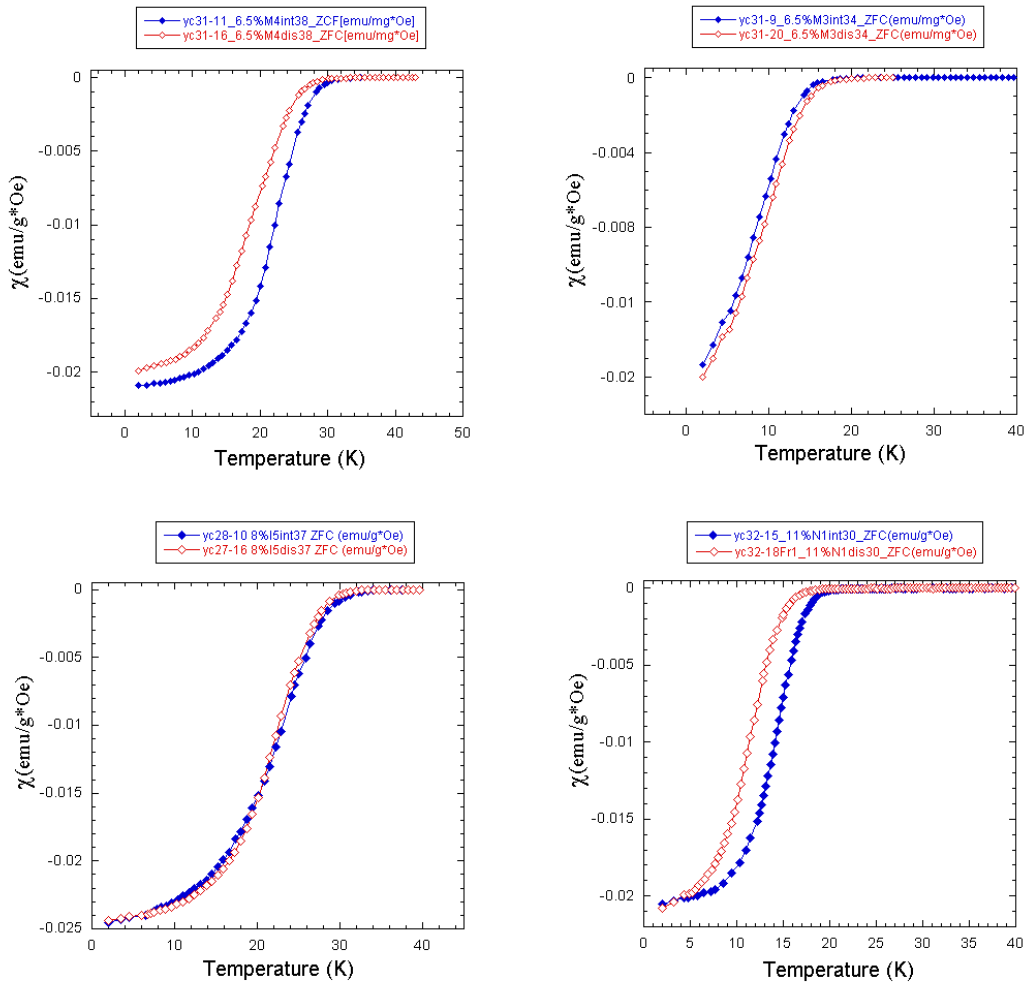

Figure 60: Comparison between ZFC bulk magnetic susceptibility of intercalated (blue, full symbols) and disintercalated (red, open symbols) pair samples, measured in 2Oe. Ca6.5% with y=0.36 and with y=0.40 are in the upper-left and upper-right panel respectively. Ca8% with y=0.37 and Ca11% with y=0.30 are in the bottom-left and bottom-right ones.

our results will refer to the intercalated phase.

5.4.3 Powders and bulk measurements

The susceptibility measurements on superconducting samples are affected by the demagnetization field contribution, $\mathbf{H}_d$. This field can be visualized as generated by magnetic monopoles left on the sample surface and is proportional to the magnetization ($\mathbf{H}_d = -\overline{N}\mathbf{M}$), where $\overline{N}$ is the demagnetization tensor. $\mathbf{H}_d$ is spatially inhomogeneous and depends on the geometry of the sample. Its contribution can be calculated only in special cases: for an ellipsoidal sample $\overline{N}$ can be diagonalized, and if we consider a sphere it reduces to the scalar 1/3. When the sample geometry allows to calculate N, the intrinsic susceptibility value can be evaluated by the simple relation $\chi_{exp}=\chi_{intr}/(1 + N\chi_{intr})$. Occasionally we performed ZFC-FC measurements on fine ground samples (one example is the right panel of Fig. 61). In this case the $\chi(T)$ value can be corrected,by assuming grains of spherical shape, for which N=1/3.
In Fig. 61 the comparison between bulk (left) and powder (right) measurement on the Ca18% $y = 1$ sample is shown. The bulk samples show a much greater difference between the ZFC and FC curves, because of the pinning due to the intergrain boundaries, absent in the powdered samples. However the measurement on powder display a much larger transition. This is expected when the the grain size is comparable to the penetration depth at zero temperature ($\lambda_L(0) \sim R/2$): the temperature dependence of λ expressed in Eq. 51 broads the

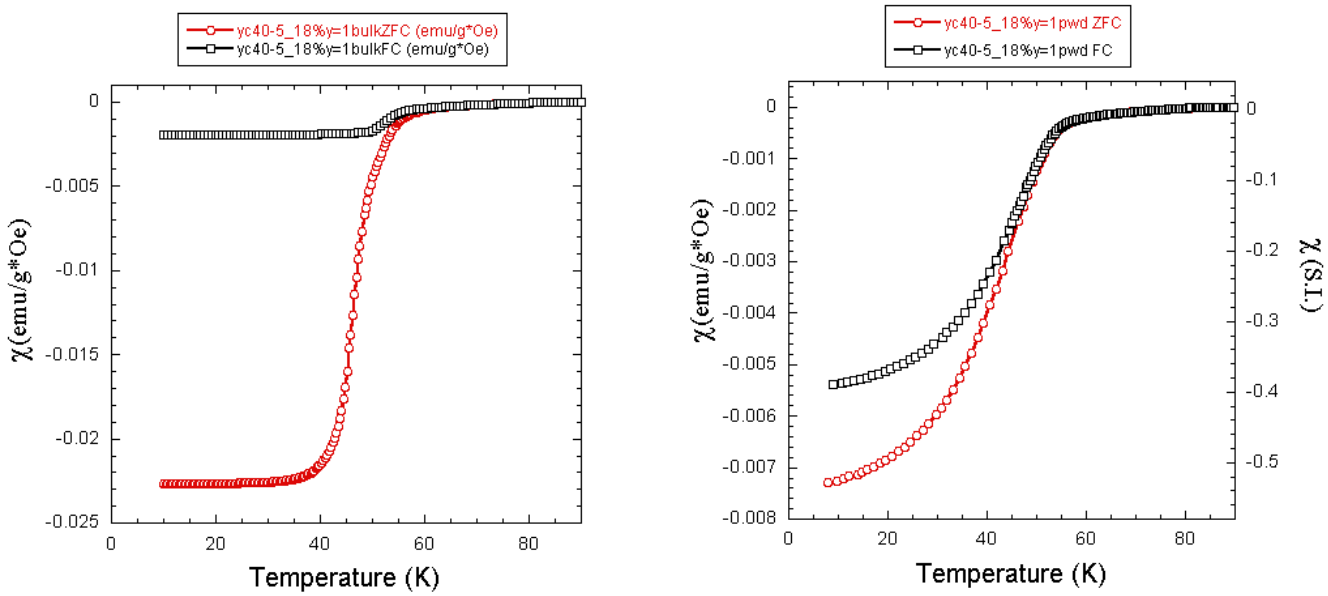

Figure 61: ZFC (red, circles) and FC (black, squares) magnetic susceptibility versus temperature for the sample Ca18% y≈1, in the bulk (left) and powder (right) form.

transition, and at the same time reduces shielded fraction in the ZFC curve. For the same reason $|\chi(0) < 1|$, i.e. the shielded volume fraction is lower than 100%. From the relation $\chi/\chi(0) = (1-f)^3$ [12] with $f = \lambda/R$, $\chi(0) = -1$, $\lambda \approx 0.2$ μm, for the sample in Fig. 61 with $\chi = 0.5$, we obtain $R \sim 1$ μm, compatible with the size of our grains. Considering that the contribution of lambda is not easy to be subctracted we will refer to the bulk samples which also give a sharper transition.

5.4.4 Fully oxidized Ca doped samples

In this last section I report a short comment about the measurement on various series of fully oxidized Ca substituted samples. Figure 62a shows the bulk ZFC curves for such samples, that for the sake of clarity I normalized on an arbitrary scale. From the Ca1% sample, for increasing Ca substitutions, the transition is largely shifted toward lower temperatures. The shift is systematic, and much larger than any effect which might be generated by oxygen deficiencies that sometimes occur during the preparation. In fact we can evaluate that at optimum doping ($y \sim 0.9$) an oxygen deficiency $\Delta y \sim 10\%$ (the maximum value we have observed via titration) would correspond to $\Delta T_c \sim 7$K [110]. Therefore the progressive reduction from the maximum T_c=92K at $x = 0$ to 53K at $x = 0.18$ is the signature of overdoping due to Ca substitution. In Fig. 62b the smooth linear dependence of $T_c(x)$ also guarantees an effective Ca-Y substitution in the whole explored range. Remarkably, it confirms the double doping mechanism already pointed out in Fig. 54b that we largely exploit in this work. In Fig. 63 I report the critical temperature of all the final samples of each series.

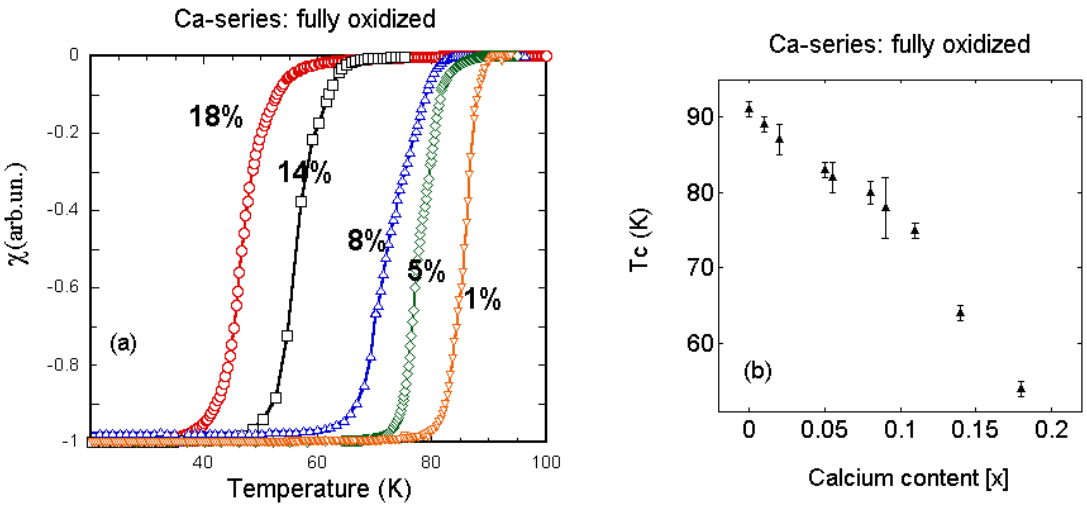

Figure 62: Left: $\chi(T)$ for the "as grown" end members (y≈1) of the Ca1%, Ca5%, Ca8%, Ca14% and Ca18% series. Applied field: 2Oe. The decreasing of T_c with increasing Ca content is due to overdoping. Right: the T_c of all the fully oxidized samples considered in this work.

Series	Sample name	y	equalization	Tc (K)
Ca5%	yc23-6	0.28	G2int28	0
Ca5%	yc23-19F1	0.32	G3dis32	3(2)
Ca5%	yc23-9	0.32	G3int32	5(3)
Ca5%	yc18-7	0.335	D2int36	14(1)
Ca5%	yc21-12	0.345	F3int37	18(1)
Ca5%	yc23-11	0.36	G4int36	23(1)
Ca5%	yc10-4	0.375	D4int40	32(1)
Ca5%	yc18-10	0.375	D4int40	29(1)
Ca5%	yc18-4	0.375	D4dis40	30(1)
Ca5%	yc10-5	0.39	D3int39	37(1)
Ca5%	yc10-15	0.39	D3dis39	38(1)
Ca5%	yc10-18	0.42	D5dis42	44(2)
Ca5%	yc10-8	0.42	D5int42	44(2)
Ca5%	yc22-8	0.51	F5int51	54(1)
Ca5%	yc22-15	0.51	F5dis51	54(1)

Series	Sample name	y	equalization	Tc (K)
Ca8%	yc27-4	0.300	I2int31	4(2)
Ca8%	yc28-15	0.300	I2dis31	6(1)
Ca8%	yc28-4	0.300	I2int31	5(2)
Ca8%	yc27-5	0.320	I3int34	13(2)
Ca8%	yc28-19Fr2	0.320	I3dis34	12(2)
Ca8%	yc28-9	0.355	I4int36.5	28(1)
Ca8%	yc28-7	0.355	I4int36.5	29(1)
Ca8%	yc28-19Fr3	0.355	I4dis36.6	27(2)
Ca8%	yc27-16	0.370	I5dis38.5	29(1)
Ca8%	yc27-8	0.370	I5int38.5	30(1)
Ca8%	yc27-7	0.370	I5int38.5	30(1)
Ca8%	yc28-10	0.370	I5int38.5	30(1)
Ca8%	yc28-17	0.420	I6dis44	43(1)
Ca8%	yc27-9	0.425	I6int44.5	44(1)

Ca11%	yc32-2	0.00	deox	0
Ca11%	yc32-19Fr1	0.14	M7dis22	0
Ca11%	yc32-9	0.14	M7int22	0
Ca11%	yc32-3	0.20	M5int28	1(1)
Ca11%	yc32-17Fr1	0.20	M5dis28	0
Ca11%	yc32-16	0.27	M6dis35	4(3)
Ca11%	yc32-7	0.27	M6int35	5(3)
Ca11%	yc32-15	0.30	N1int38	18(1)
Ca11%	yc32-18Fr1	0.30	N1dis38	16(1)
Ca11%	yc32-20	0.35	N2dis42.5	28(1)
Ca11%	yc32-19Fr2	0.35	N2int42.5	30(1)
Ca11%	yc32-1	0.90	y=1	82.5(5)

Series	Sample name	y	equalization	Tc (K)
Ca14%	yc33-2	0.030	deox	3(3)
Ca14%	yc33-16Fr1	0.160	O1dis23	10(2)
Ca14%	yc33-4	0.160	O1int23	10(2)
Ca14%	yc33-7	0.190	O2int26.5	14(1)
Ca14%	yc33-16Fr2	0.195	O2dis26.5	13(2)
Ca14%	yc33-19Fr1	0.260	O3dis33	26(1)
Ca14%	yc33-9	0.260	O3int33	27(1)
Ca14%	yc33-17	0.300	O4dis37	32(1)
Ca14%	yc33-11	0.300	O4int37	33(2)
Ca14%	yc33-15	0.360	O6int43	44.(1)
Ca14%	yc33-20Fr1	0.360	O6dis43	44(1)
Ca14%	yc33-1	0.910	y=1	76(2)

Series	Sample name	y	equalization	Tc (K)
Y100%	ap1int35	0.330	ap1int35	10(1)
Y100%	ap1dis35	0.330	ap1dis35	10(1)
Y100%	bp1int37	0.340	bp1int37	14(1)
Y100%	be2int36	0.350	be2int36	22(1)
Y100%	br2dis39	0.365	br2dis39	30(1)
Y100%	bl4int39	0.370	bl4int39	31(1)
Y100%	bg4dis41	0.380	bg4dis41	36(1)
Y100%	br4int41	0.380	br4int41	37(1)
Y100%	bc1dis41	0.395	bc1dis41	38(1)
Y100%	bh4dis41	0.400	bh4dis41	42(1)
Y100%	bi4dis41	0.405	bi4dis41	44(1)
Y100%	bi4int41	0.405	bi4int41	44(1)
Y100%	ag3dis50	0.480	ag3dis50	49(1)

Series	Sample name	y	equalization	Tc (K)
Nd7.5%	yn2-10/11/12	0.300	B8int30	0
Nd7.5%	yn4-6	0.313	C3int31.3	0
Nd7.5%	yn2-13/14/15	0.325	B9int32.5	0(2)
Nd7.5%	yn4-9	0.338	C4int33.8	8(3)
Nd7.5%	yn2-16/17/18	0.350	B10int35	15(2)
Nd7.5%	yn2-19/20/21	0.375	B11int37.5	23(2)
Nd7.5%	yn3-5/7	0.400	B12int40	35(2)
Nd7.5%	yn2-3/4	0.460	Aint46	49(1)

Series	Sample name	y	equalization	Tc (K)
Eu8%	ye26-12	0.315	D4int32.5	6(3)
Eu8%	ye26-15	0.325	D5int33.5	12(3)
Eu8%	ye24-9	0.340	C3int35	16(3)
Eu8%	ye24-12	0.380	C4int39	28(2)
Eu8%	ye24-15	0.400	C5int41	36(2)
Eu8%	ye30-11	0.420	E6int43	46(1)

Series	Sample name	z	y	equalization	Tc (K)
Eu35%	ye18-9	0.5	0.35	B2int37	0
Eu35%	ye6-4	0.4	0.35	Abis-int38	2(2)
Eu35%	ye4-4	0.2	0.35	Abis-int38	11(2)
Eu35%	y90-2	0	0.35	Abis-int38	18(2)

Figure 63: A summary of the T_c values for each sample. The Y100% data are from resistivity measurements.

5.5 μSR results

In this section I report the main experimental μSR findings. They describe the magnetic properties of YBCO in the clean limit under the assumption of a staggered and collinear spin arrangement explained in Sec. 5.5.1, starting from the assignment of the muon localization sites.

These properties are not affected by the isovalent substitution; therefore I report Y%100, Eu8% and Nd7.5% results together in Sec. 5.5.2. Their modifications under the introduction of charged impurities (Ca^{2+} for Y^{3+}) are described in Sec. 5.5.3, and the influence of both isovalent and heterovalent substitution on the superconducting properties is summarized in Sec. 5.5.4.

5.5.1 Spin arrangement and muon local field in cuprates

Three types of muon stopping sites are distinguished in cuprates. The dominant one, observed in all compounds, irrespective of both the details of the perovskite structure and doping, is bound to the apical oxygen (AO), just above or below the CuO_2 plaquette (see Sec. 1.2 and inset of Fig. 64). The low temperature value of the field probed by muons at this site is $B^L_{AO} = 40$ mT for La_2CuO_4 [13], and $B^Y_{AO} = 30$ mT for $YBa_2Cu_3O_6$ [27], respectively.

A second site is specific of $YBa_2Cu_3O_{6+y}$ for $y > 0.2$ and it is attributed to muons bound to chain oxygen (CO), with roughly half the field intensity. A third site, directly bound to the oxygen ions of the plaquette (PO), with large internal fields, is observed only [111] in undoped $YBa_2Cu_3O_6$.

The AO site is the main subject of our analysis, and its assignment is based on numerous observations [112, 113, 114, 115]. One of them is that the value of B^Y_{AO} at zero temperature and doping is reproduced by simple dipolar sums: if $S(h,T)$ is the average staggered Cu spin that gives rise to the staggered magnetic moments, $\hat{S}_i$ is the spin direction at site i, $r_i = r_i\hat{r}_i$ is the vector joining the muon site to the i-th Cu spin and g is the Landé factor, we can write

$$\begin{aligned} B_{AO}(h,T) &= \frac{\mu_0 g \mu_B}{4\pi} \left| \sum_j \frac{3(\hat{S}_j \cdot \hat{r}_j)\hat{r}_j + \hat{S}_j}{r_j^3} \right| S(h,T) \\ &= |D|\, S(h,T), \end{aligned} \tag{57}$$

The zero temperature value is reproduced in this site with the standard [24] 2D spin reduction, $gS(0,0) = 0.6$. A small isotropic super-hyperfine contribution cannot be a-priori excluded, but it would preserve the validity of Eq. 57, with the simple addition of a term $A\hat{S}_1$ to D, S_1 being the Cu spin nearest to the muon.

The sums defining vector D in Eq. 57 converge rapidly, thanks to the alternating sign of $\hat{S}_i$ in the AF structure (the staggered moment). Even in the very underdoped superconductor

$YBa_2Cu_3O_{6.35}$, where in-plane magnetic correlation lengths are shortest, [45] they never fall below $\xi_{a,b} \approx 12$ Å, and the relative contributions to Eq. 57 for $r_j > \xi_{a,b}/2$ are only a few percent. Hence the local field may be written as a constant, $D = |D|$, times $S(h,T)$. The rapid convergence of the dipolar sums and the tensorial nature of the interaction guarantee that D does not change as long as the local spin directions $\hat{S}_i$, nearest neighbours to the muon, remain *i)* collinear, *ii)* parallel to the *ab* plane, and *ii)* staggered. These points follow from the consideration that the value of B_{AO} obtained in the simple Néel arrangement is actually invariant under in-plane $\hat{S}_i$ rotations for a muon site coinciding with that of the apical oxygen. The AO site is displaced only by 110 pm from this symmetry position and the invariance is roughly preserved. By converse if either the moment were drastically reduced, or the local spin arrangement did change significantly from staggered, collinear and in-plane, the low temperature value of the local muon field of Eq. 57 would also change. As it will be shown in Sec. 5.5.2 and 5.5.3, in all our measurements we detect a nearly constant local field $B_{AO}(h,0)$ (rescaled to $m_R(h)$), that requires both nearly constant D and S. An unvarying D in turns implies that a collinear staggered in-plane spin arrangement is at least locally preserved at low temperature for all hole densities.

The field distribution itself does not change appreciably as it is witnessed by the measurements reported in Sec. 5.5.2; the low temperature asymmetries in the nine panels of Fig. 66, spanning from $h = 0.02$ (top) to $h = 0.07$ (bottom) are very similar. If local correlations did vary significantly we would observe the appearance of distinct frequency components, signaling different internal fields, whereas the only notable change is that the damping of the precessions (i.e. the width of the field distribution) increases with hole content.

The field distribution does not change appreciably with temperature either. Fig. 64 shows

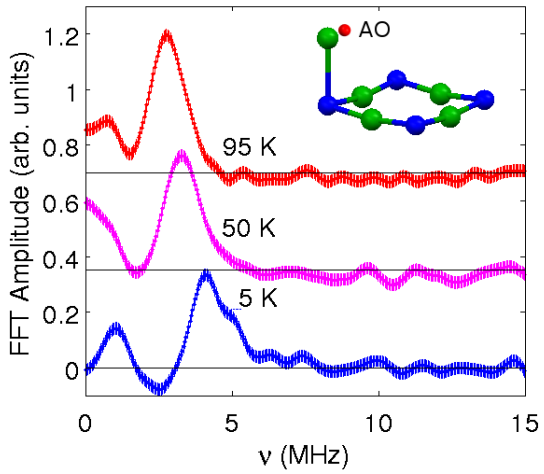

Figure 64: $YBa_2Cu_3O_{6+y}$, $y = 0.27$, $h = 0.023$: FFT amplitude of the precessing asymmetry a three temperatures. Inset: muon AO site, with apical oxygen and the CuO_2 plaquette.

representative Fast Fourier Transform (FFT) spectra of the muon precessing asymmetry for three temperatures below the magnetic transition T_N. They display two peaks corresponding to the AO and CO sites, which shift to lower frequency as $S(T)$ is reduced, preserving their shape.

5.5.2 Magnetic behaviour in the clean limit

Typical asymmetry functions in magnetically ordered and paramagnetic phases are shown in Fig. 65a with the relative best fits for one of our Y100% samples ($y = 0.25$ $h \sim 0.04$). From bottom to top the time evolution of the muon asymmetry is shown for three temperatures, the lowest, one close to the magnetic transition and one just above it. Following Eq. 44 the

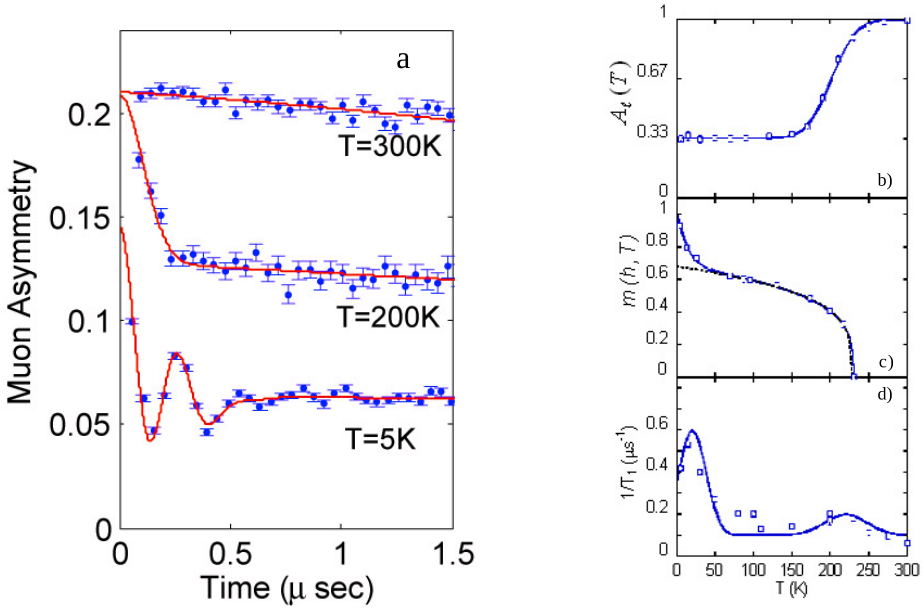

Figure 65: Left panel: typical asymmetry functions for three significative temperatures. The red line is the best fit to the functions described in the text. Right panels: from top to bottom, the longitudinal muon fraction $f^\ell$the staggered normalized magnetic moment $m(T)$ and the longitudinal relaxation rate $1/T_1$; from their temperature behaviour the magnetic transition temperature T_m is extracted.

asymmetry is given by

$$A(t) = A_0 \left[\sum_i f_i^t e^{-(\sigma_i^2 t^2)/2} \cos \gamma B_i t + f^\ell e^{-\lambda t} \right], \tag{58}$$

where $\gamma = 0.8514 \cdot 10^9$ $(\mathrm{sT})^{-1}$ is the muon magnetogyric ratio, $f^{t,\ell}$ are the transverse and longitudinal muon fractions, experiencing relaxation rates σ_i and λ, respectively. The index i spans the two muon sites, AO and CO (see Sec. 5.5.1), where muons probe two distinct local fields B_{AO} and B_{CO}. The longitudinal term does not distinguish the two sites.

When magnetic and non-magnetic phases are present in the sample, since muons are evenly implanted in both, their fractions reflect the relative volumes of the two phases. The transverse fractions obviously disappear in the paramagnetic phase, hence the smooth drop of f^ℓ to 1/3 across the magnetic transition temperature, reported in Fig. 65b, signals some oxygen inhomogeneity, producing a Gaussian distribution [12,35] of magnetic transition temperatures of mean T_m and width ΔT_m. It can be therefore fitted by

$$f^\ell(T) = (1/3)[2 + erf((T - T_m)/\sqrt{2}\Delta T_m)]. \tag{59}$$

By converse the relative magnetic volume $v_m = V_m/V_{tot}$, given by $v_m = 3(1 - f^\ell)/2 = 3f^t/2$, increases across the transition and can be fitted to the function

$$v_m(T) = [1 - \mathrm{erf}((T - T_m)/\sqrt{2}\Delta T_m)]/2. \tag{60}$$

These two equations allow the determination of the magnetic transition temperature T_m. It is worth to notice that we do not distinguish yet between T_N and T_g because the muon cannot identify the two states; in Ch. 6 the way to characterize theme will be clarified.
The middle plot (T=200 K) in Fig. 65a shows data just below T_m characterized by over-damped precessions and increased value of the longitudinal fraction f^ℓ. Best fits allow only for one indistinguished transverse fraction, with $B = \sqrt{\Delta B^2}$.
At the highest temperatures, well above the magnetic transition, samples are fully in the paramagnetic state and the asymmetry is fitted to the function

$$A(t) = f^\ell e^{-(\sigma_n{}^2 t^2)/2} \tag{61}$$

with $f^\ell = 1$ and σ_n is the static contribution to the relaxation rate arising from neighbour nuclear moments.
Fig. 65c shows the reduced staggered magnetization

$$m(h, T) = B_{AO}(h, T)/B_{AO}(0, 0), \tag{62}$$

where $B_{AO}(0, 0)$ is the muon internal field value at zero temperature in the undoped compound. Fig. 65d shows the $1/T_1$ relaxation rate of the longitudinal fraction; both of these quantities allow in principle an independent determination of the magnetic transitions.

The staggered magnetization, whose details are discussed in the following, vanishes at T_m. The $1/T_1$ relaxation rate displays two peaks, both connected (according to section 4.2.5) to the presence of slow spin fluctuations. The lower temperature one will be discussed in Sec. 6.1.4. The second is due to the slowing down of the critical fluctuations at the transition temperature T_m. The extraction of T_m from the vanishing of $m(h, T)$ is not accurate at low doping, i.e. high magnetic transition temperatures, because above $T \approx 250$ K muon diffusion sets in, preventing the direct measure of the transverse precessions, but not that of

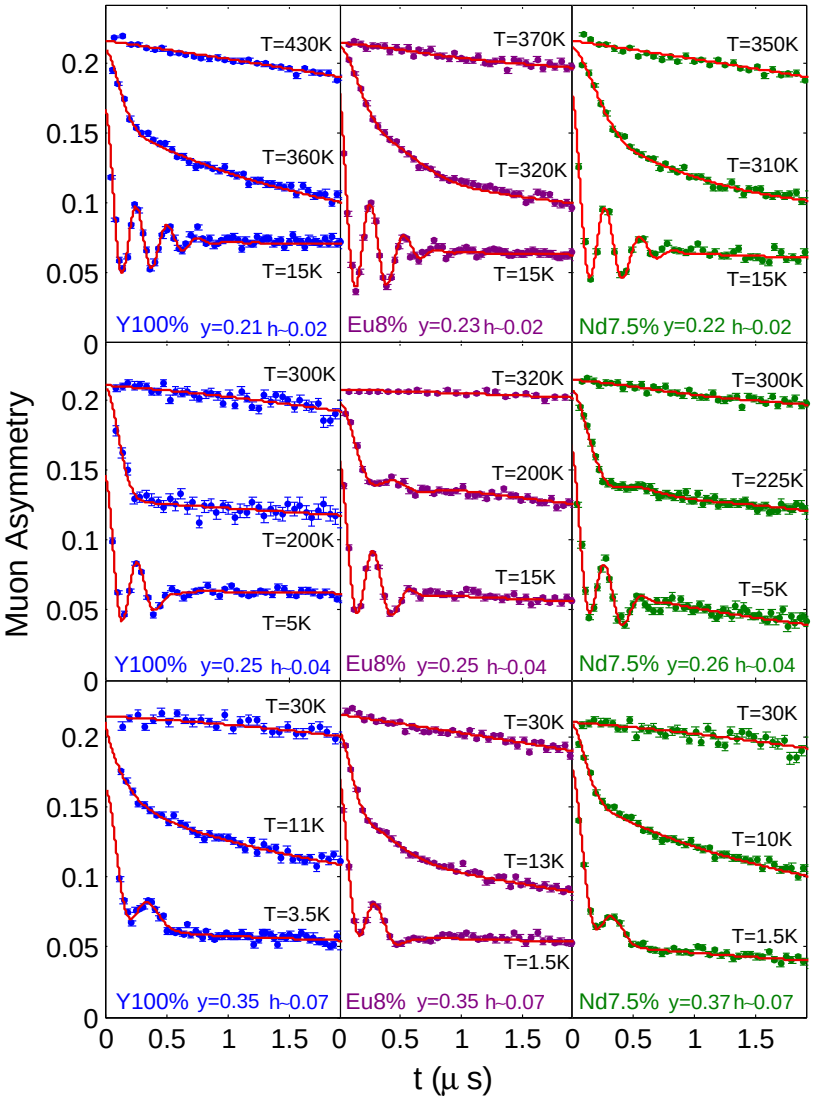

Figure 66: Muon asymmetry above T_N, just below and for $T \ll T_N$. Left column: three $YBa_2Cu_3O_{6+y}$ samples. central and right columns: three corresponding $Y_{0.92}Eu_{0.08}Ba_2Cu_3O_{6+y}$ and $Y_{0.925}Nd_{0.075}Ba_2Cu_3O_{6+y}$ samples, from nearly undoped (top) to above the onset density for superconductivity.

the longitudinal fractions [35], therefore the the Néel temperature can still be determined. More instances are shown in Fig. 66 where the left, central and right column refers to Y100%, Eu8% and Nd7.5% respectively. From top to bottom three different samples for each class of compounds span the magnetic phase diagram, from very low to intermediate doping ($h \approx 0.02$, $h \approx 0.04$, and $h \approx 0.07$ respectively). The analysis described above provide the magnetic transition temperatures.

Fig. 67a shows the behaviour of the normalized staggered magnetization $m(h, T)$ for three $YBa_2Cu_3O_{6+y}$ samples whose hole density ranges from nearly undoped, to just over the critical value where superconductivity appears, the strongly underdoped regime. Fig. 67b

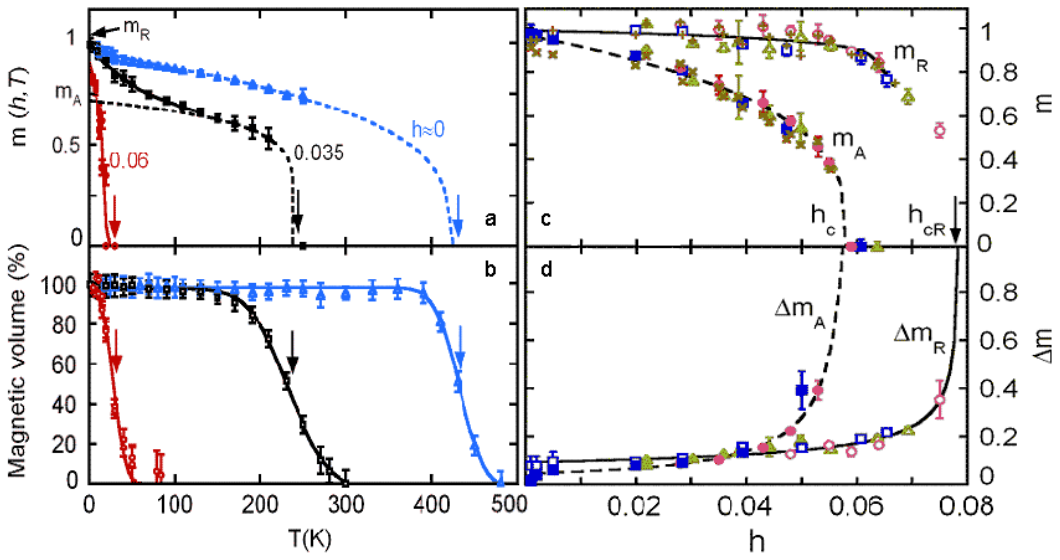

Figure 67: a: Staggered magnetization for three samples of the series Y100%; the dotted lines show the fit of the high temperature data to a critical behaviour, while the full lines represent the magnetization upturn. b: The magnetic volume fraction for the samples plotted in the a panel. c: m_R and m_A for three full sets of samples (Y100%, Eu8% and Nd7.5%); the values calculated with the preliminary fit and the thermally activated model of Eq. 64 are almost coinciding. d: The widths $\Delta m_{R,A}$ of the two static distribution show critical behaviours at h_c and h_{cR}.

displays the fraction of implanted muons detecting the magnetically ordered state, i.e. the fraction of the samples volume belonging to the magnetic state. Both quantities are extracted from the muon asymmetry analysis reported at the start of this section.

First of all the data of the two panels allow the determination of the magnetic transition temperature T_m (as previously reported we do not distinguish yet between T_N and T_g, because the muon cannot *directly* identify the two states). These temperatures are indicated in both panels by the vertical arrows: for $h = 0, 0.035$, and 0.07, T_m is respectively about 430, 230 and 30 K. Secondly, at intermediate doping the order parameter m deviates from a standard power law behaviour like that of the undoped sample (dashed lines). The power law, with lower T_m and rescaled magnetization, is followed only at high temperature, whereas an upturn (solid line) appears toward the *undoped* zero temperature value, $m(0.035, 0) = 1$. The corresponding moment μ reaches the value $\mu_{2D} \approx 0.6\,\mu_B$ (μ_B being the Bohr magneton) appropriate to the two dimensional spin 1/2 Heisenberg antiferromagnet (2DHAF), with its quantum spin reduction [24]. For finite h the recovery of the undoped magnetization $m(0, 0)$ shown in Fig. 67a justifies the term *re-entrance* (whence the subscript R) for this behaviour. A similar upturn is just barely perceptible also in the light blue data , i.e. for the undoped case; as pointed out in Sec. 1.3.1, it has been described before, first [30,42] in $La_{2-x}Sr_xCuO_4$, then [36,35,37] in $YBa_2Cu_3O_{6+y}$. Many more instances showing such an upturn are shown in Fig. 68. Muons and NQR data agree quantitatively on the low temperature upturn, granting

that this is *not* one of those very rare instances where the muon alters its local surroundings.

The data are naturally described as the crossover from a low temperature magnetization toward a magnetically weaker high temperature regime, whose origin must be found in the thermal population of the doped Mott-Hubbard excitations, in other words in a thermally activated process. The functional form of the upturn looks like an exponential decay to the rescaled behaviour. Thus, in order to distinguish the two regimes, we perform a first qualitative fit of the data [35] to the function

$$m(h,T) = [m_A + (m_R - m_A)e^{-cT}]\ (1 - T/T_m)^{\beta}, \tag{63}$$

where $m_{R,A}$ stand for the reduced moment in the re-entrant and activated regimes, respectively. The former value corresponds to the experimental ratio at $T = 0$, $m_R = m(h, 0)$ and the latter, m_A, yields the zero temperature extrapolation indicated by the dashed line in Fig. 67a. For $h > 0.055$ we must revert to a simple power law fit $m(h,T) = m_R\,(1 - T/T_m)^{\beta}$. Similar fits are obtained for all of the samples, including those with Eu and Nd partial substitutions.

The m_R and m_A values extracted by this preliminary fit are shown by brown plus and crosses in Fig. 67c, where it is possible to notice that the re-entrant zero temperature parameter m_R is very close to one, up to the highest hole densities, until it undergoes an abrupt reduction around a hole content equal to $h_{cR} \approx 0.08$. By converse the activated parameter m_A, plotted in the same panel, displays a clear distinct critical behaviour, fitted to a power law $m_A = (1 - h/h_c)^{\alpha}$ with $\alpha = 0.35(5)$ and $h_c = 0.058(2)$. This difference is a first, important result, whose discussion is momentarily postponed to a following part of this chapter when, after some strightforward considerations, its significance will be more clear.

It is now tempting to include the power law behaviour of $m_A(h)$ (Fig. 67c) directly into the fit model, (i.e. into the function describing the high temperature m behaviour) identifying its doping dependence as $m_A(h) = m_R(h)\,(1 - h/h_c)^{\alpha}$. It is however clear that a constant hole density does not reproduce the thermally activated features of m and a straightforward extension is to replace h by $h(T) = h\exp(-T_A/T)$, assuming for the sake of the argument that delocalized (hopping) holes are responsible of the magnetization reduction. This leads to

$$m(h,T) = m_A(h,T)\left(1 - \frac{T}{T_m}\right)^{\beta} = m_R\left(1 - \frac{h}{h_c}e^{-T_A/T}\right)^{\alpha}\left(1 - \frac{T}{T_m}\right)^{\beta}. \tag{64}$$

This activated-hole function yields excellent best fits of the data as it is shown by the solid lines in Fig. 68.

We note however that Eq. 64 could also hold in a stripe scenario [116], where it is possible to imagine a mechanism by which the influence of thermally activated excitations on magnetism depends on the stripe density, which in turns is proportional [117] to h.

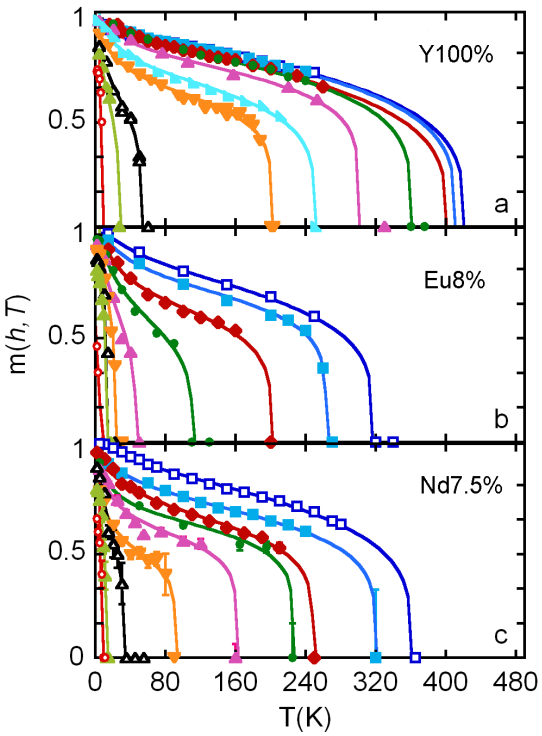

Figure 68: Staggered magnetization for three full sets of samples: the Y100% and the Eu8% and Nd7.5% isovalent substituted series. The lines show the fit of the data to the thermally activated model introduced in Eq. 64.

The new parameter T_A quantifies the crossover temperature between the two magnetic regimes. The difference from the previous functional form is often beyond resolution, that is the magnetic critical temperature T_m, as well as m_A and m_R, fitted in the two models, are almost identical. The two reduced moments displayed by the brown plus and crosses in Fig. 67c have in fact a counterpart in the activated-hole model described by Eq. 64: the zero temperature moment, m_R, is still a free parameter, whose functional dependence on h is directly determined by best fit procedures, whereas m_A is obtained as $\lim_{T\to\infty} m_A(h,T)$. These new determinations agree perfectly with the previous ones as it is shown by the colored marks in Fig. 67c, often superimposed on the data of the first fit. Once again, therefore, they underlie the two distinct trends for the quantities m_A and m_R vs. h. Two very distinct critical behaviours are also shown in Fig. 67d, where the plot of the widths $\Delta m_{R,A}$ of the two static moment distributions is presented. These widths are obtained directly from the static relaxation of the muon asymmetry precession as $\sigma_{AO}(T)/2\pi\gamma B_{AO}(0)$, taking cuts through the data at two temperatures: the lowest one, $2K$, below all T_A and another one, $70K$, above the largest T_A. Both quantities display a divergence which points to the same two distinct critical densities mentioned above, h_c and h_{cR}.

A compact view of the transition temperatures, together with the reduced moment as a

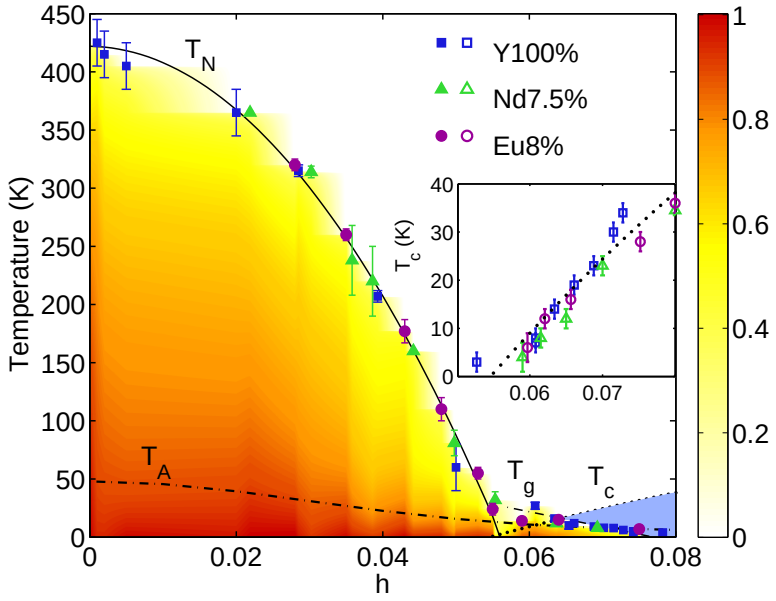

Figure 69: Common phase diagram for Y100%, Eu8% and Nd7.5% series: transition temperatures T_N and T_g from the fits to Eq. 64; experimental reduced moment m, still from the fit to Eq. 64, are encoded in the nonlinear color mapping (see right bar). The phase boundaries are best fits with $h_c = h_s = 0.056(2)$ (see text) and T_A labels the guide for the eye of Fig. 70. Inset: zoom of the superconducting T_c.

color map, is provided by Fig. 69 for the three families Y100%, Eu8% and Nd7.5%. It is evident that they display a unique behaviour, both magnetic and superconductive (see the inset), within experimental errors; in addition, the plotted T_m agree qualitatively with many previous observations [12, 27, 28, 29, 118] on unsubstituted $YBa_2Cu_3O_{6+y}$, but only here are presented as a function of calibrated hole density h. We recognize two regions: the first for $0 < h \lesssim 0.05$ where T_m drops rapidly with increasing hole density, and we identify it with the Néel transition; the second for $h \gtrsim 0.05$, where the $T_m(h)$ dependence is much weaker, and we associate this transition with T_g. The Néel temperature follows a quadratic behaviour vs. hole density $T_{N0}(1 - (h/h_c)^2)$ with $T_{N0} = 422(5)$ K and critical concentration $h_c = 0.056(2)$ as shown by the continuous line in Fig. 69.

The color map is nonlinear to emphasize the upturn of $m(T)$, already underlined in this section, and well evident in Fig. 68. The re-entrant region is characterized by a uniform dark red color toward $T = 0$, signifying that $m_R = m(h, 0)$ approaches the full 2D moment μ_{2D} at all dopings, even underneath the superconducting dome. The parameter T_A, that quantifies the crossover temperature, is reported both in Fig. 69 as a dot-dashed line to guide the eyes, and in Fig. 70, where the value for each sample is plotted in an expanded scale. The activation energy follows a dome that replicates roughly the AF phase boundary, albeit

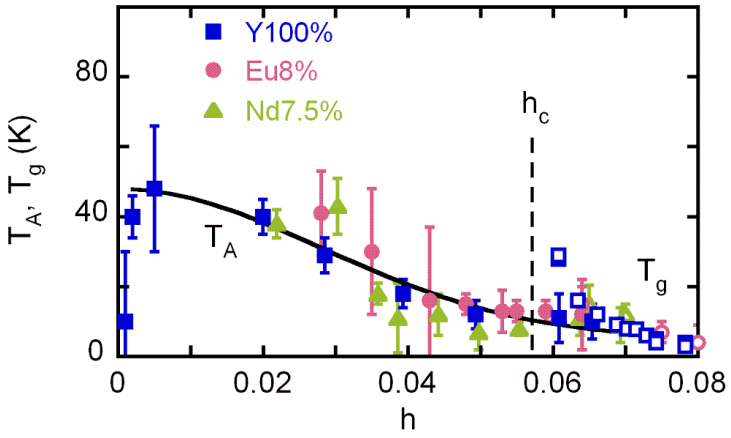

Figure 70: Dependence on hole doping of the activation temperature T_A from the best fits to Eq. 64. The line is a guide for the eye and the T_A (closed symbols) and T_g (open symbols) data for $h > h_C$ are overlapping within the error bars.

with a large down-shift. On entering the CSG phase coexisting with superconductivity, for $h > h_c$, the fit gives T_A values hardly distinguishable [1] from T_g, hence in Fig. 70 the open symbols (T_g) are often overlapping with the full ones, T_A.

5.5.3 Magnetic results on the dirty limit compounds

Figure 71a shows a three dimensional view of the $Y_{1-x}Ca_xBa_2Cu_3O_{6+y}$ phase diagram, that summarizes our results (notice that the $x = 0$ plane corresponds to the diagram of Fig. 69). These results disentangle the influence of doping, h, and disorder, x, showing that the portion of the green region where T_g is the only transition temperature continuously widens with increasing Ca content, i.e. with disorder. A similar conclusion was qualitatively shown in earlier work on Zn substitution [119], across different cuprate families [19], and in irradiated samples [48].

Let us describe distinct influence of doping and disorder in Fig. 71a. Dotted parabolas describe the superconducting transitions $T_c(h)$, which shift rigidly to higher onsets $h_s(x)$ with Ca content, as we previously reported [47]; it is discussed in details in the forthcoming Sec.6.2. Solid parabolas represent the doping dependence of the Néel temperature $T_N(h) = T_{N0}(1 - (h/hc)^2)$ with $T_{N0} = 422(5)$ K and $h_c = 0.056(2)$, discussed in the previous section for the clean limit. For the sake of clarity the Eu and Nd data are omitted.

Remarkably the same function, with no adjustable parameters, agrees with the low hole density data of Ca1% (diamonds) and Ca5% (circles), demonstrating that $T_N(h)$ is, at least initially, a universal function of doping, independent of the disorder parameter x. A first-order transition from high T_N values to much lower T_g values (dash-dotted lines in Fig. 71a)

[1] A single sample, Y100% with $h = 0.06 \gtrsim h_c$, stands just outside the limits of this classification, since its magnetic transition, $T_m = 28$ K is larger that its activation temperature $T_A = 15$ K .

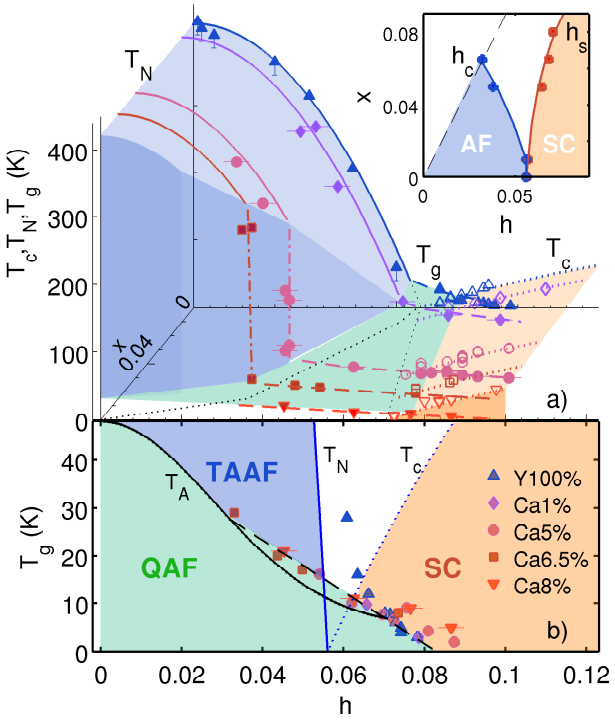

Figure 71: Doping (h) and disorder (x, Ca content) dependence in YBCO: a) Phase diagram; inset: critical hole densities $hc(x)$ and $h_s(x)$; b) Zoom of $T_g(h,x)$, projected on the $x = 0$ plane; solid dotted and dashed-dotted curves are the clean limit T_N, T_c, and T_A, respectively, from [95].

interrupts this behavior at Ca dependent critical hole densities, $h_c(x)$. A similar abrupt jump is displayed also by $Ca_xLa_{1.25}Ba_{1.75-x}Cu_3O_{6+y}$, a system where doping can be varied at fixed disorder [120]. The slightly asymmetric influence of disorder on the two critical hole densities, h_c and h_s, is plotted in the inset of Fig. 71a.

Another very interesting point is the doping and Ca dependence of the low transition temperature T_g (dashed curves in Fig. 71a). Figure 71b projects the $T_g(h,x)$ data on the T,h plane revealing that they all fall on the same dashed line, from $x = 0$ to $x = 0.08$. Notice that this line lies very close to the activation temperature $T_A(h)$ detected in the clean limit compounds (solid curve), i.e. at the crossover between the the thermally activated AF regime. The linear trend is obeyed by all except a small number of points. The deviations regard a single Y100% sample at one end, ($h = 0.06$, already commented in the previous section), and a few Ca doped samples at the opposite end, for large hole densities, where the low temperature magnetic regime is slightly extended by disorder, in agreement with theoretical predictions [121].

Figure 72 shows the very similar time evolution of the zero field muon asymmetry at $T = 2$ K, in three Ca5% samples with different hole densities, respectively $h = 0.031 < h_c$

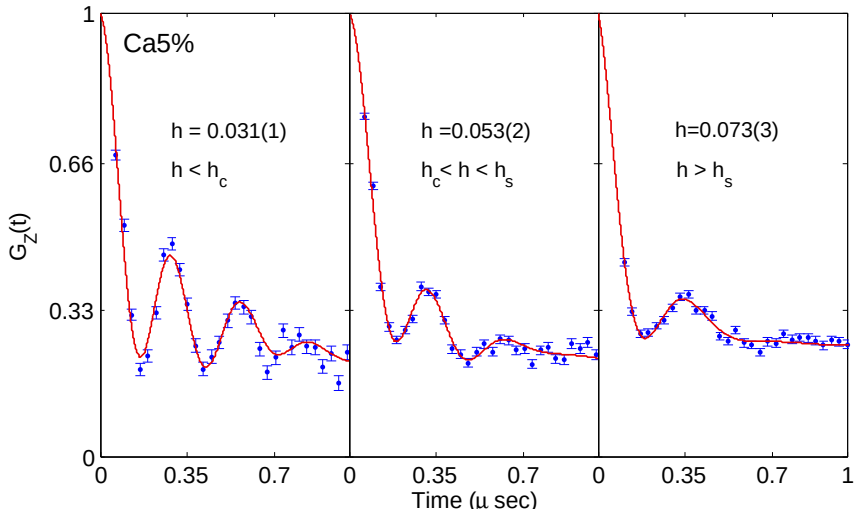

Figure 72: Muon asymmetry at T=2 K with best fits for three Ca5% samples with very different hole densities.

($T_N = 258$ K), $h_c < h = 0.053 < h_s$ ($T_g = 16.1$ K) and $h = 0.073 > h_s$ ($T_g = 7.7$ K), within the green region of Fig. 71b. Solid curves are best fits. Apart from a modest frequency reduction, the main difference between the three samples is an increase of the damping, up to a maximum relative value $\Delta m/m = \Delta B_\mu/B_\mu = 0.3$, that indicates inhomogeneity, but still within a well ordered magnetic state, as it is demonstrated by the oscillatory pattern still present for $h > h_s$. We now consider the disorder dependence of the staggered magnetic moment. Let us focus on two slices of the phase diagram of Fig. 71a, at constant doping versus disorder, for $h \approx 0.03$ and 0.04. The temperature dependence of $m(T)$ is displayed in Fig. 73 for different values of x (disorder) in the slices. Best-fit solid curves follow the same model of clean compounds (Eq. 63), describing the low temperature upturn due to the smooth moment crossover to the activated regime. The most important features are:

- m_R, which is the actual $T \to 0$ value in the low temperature state, approaches $0.6\,\mu_B$ at all h and x, and its values are in totally agreement with best fit of Fig. 67.
- m_A, the low temperature extrapolation (Fig. 73b) of the power law in the activated regime, is reduced and strongly (h, x)-dependent.

The best fit parameters m_A and m_R are shown in Fig. 74, panels b, d, and the corresponding transition temperatures in panels a, c. The first order nature of the transition between samples with and without an activated phase is apparent (panels a and c) also when cut along the disorder axis.

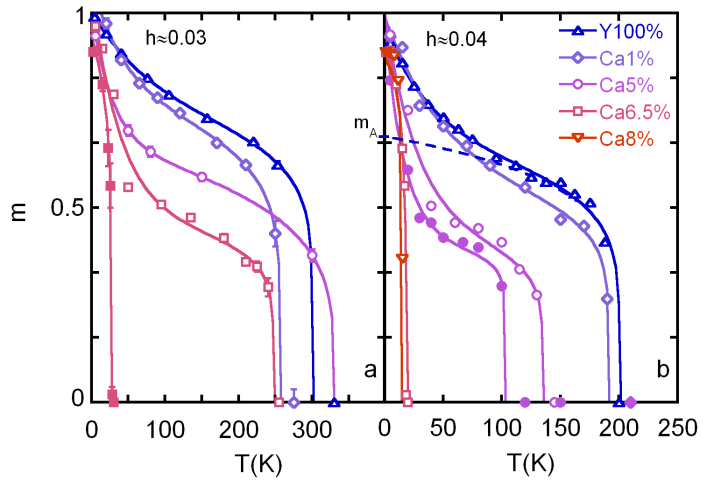

Figure 73: Temperature dependence of the magnetic moment with the best fit to Eq. 63, for the $h \approx 0.03$ (a) and $h \approx 0.04$ (b) samples. The dashed line shows an example of the low T extrapolation m_A.

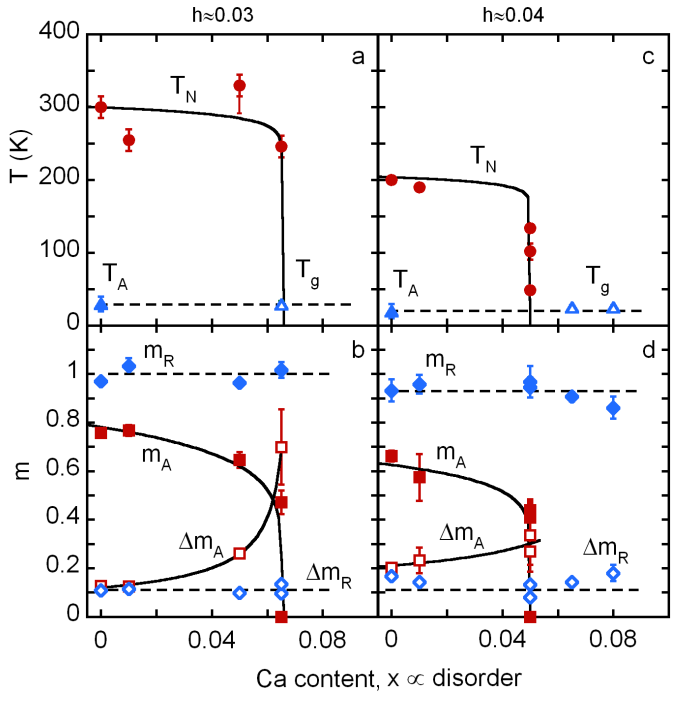

Figure 74: Samples at constant hole densities: a) and c) Ordering (T_N, T_g) and activation (T_A) temperatures ; b and d) Magnetic moment and width of its distribution in the low temperature $(m_R, \Delta m_R)$ and in the high temperature $(m_A, \Delta m_A)$ magnetic regimes.

5.5.4 Superconducting behaviour from the clean to the dirty limit

In this investigation we have addressed two properties of the superconducting state: the critical temperature T_c, determined most reliably by SQUID (Sec. 5.4), and the density of superconducting carriers n_s, by means of TF-μSR experiments (Eq. 49).

5.5.4.1 TF-μSR in underdoped cuprates

Field-cooling (FC) experiments in transverse field configuration have been performed in order to probe the flux-lattice distribution in the mixed state.

A typical TF asymmetry data set in B_{ext}= 220 Oe is shown in the panels of Fig. 75, for decreasing temperatures from (a) to (f). The sample is one of the Ca5% series that displays nanoscopic coexistence of magnetism and superconductivity. Below $T_N = 5.5K < T_c = 18$ K muons experience the composition of the external field, the spontaneous internal AF field, and the contribution from vortices.

Panel (a) refers to the signal in the normal, paramagnetic phase. The applied external field

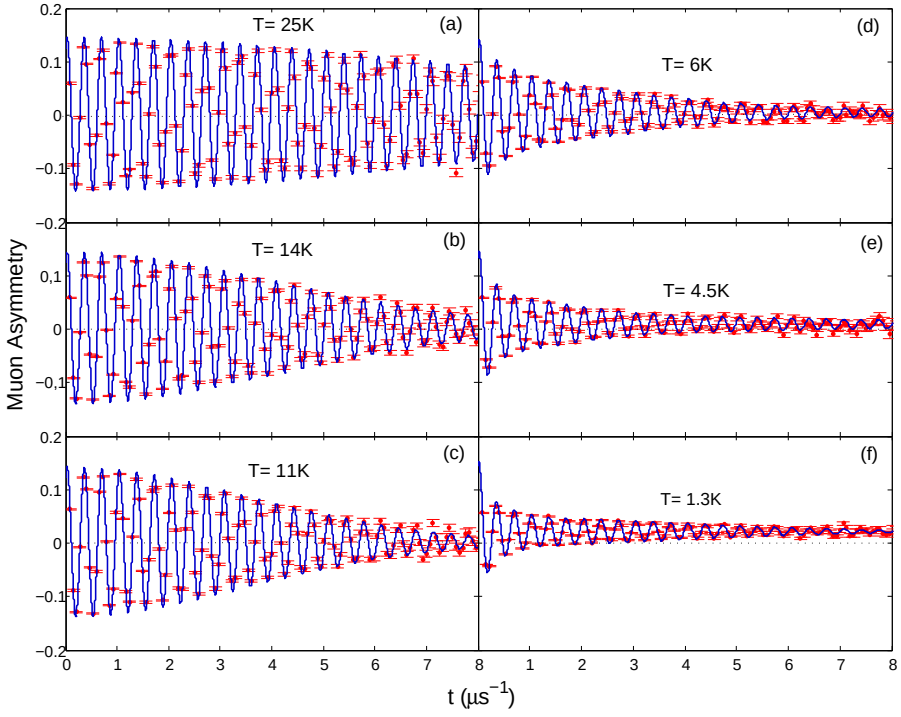

Figure 75: TF asymmetries for various temperature of a Ca5% with $T_N = 5.5K$ and $T_c = 18K$. The red dots are the data, with their errorbars; the blue lines is the best fits. (a): paramagnetic state ($T \geq T_N$). (b) and (c): The superconducting state is developing ($T_c \geq T \geq T_N$) and the signal is damped by the presence of the flux-lattice. (d),(e) and (f): The magnetic state is developing ($T \leq T_N$): the signal is overdamped by the further inhomogeneities introduced by a spontaneous internal field distribution.

entirely penetrates inside the sample, therefore the local field at the muon site is simply given by $B_\mu = \mu_0 H$. The transverse asymmetry is characterized by a weak Gaussian decay governed by a small σ_n (typically $\sim 0.13\mu s^{-1}$) that arises from the field inhomogeneities generated by the randomly oriented nuclear Cu dipolar moments. In panels (b) and (c) the presence of a further contribution to the relaxation, that increases with decreasing temperatures, is evident; it is originated by the stronger field inhomogeneities due to the presence of a flux lattice that progressively develops together with the superconducting state. For $T \leq T_N = 5.5$K (panels d,e,f) the asymmetry profile is no longer a single Gaussian and the overall damping is much stronger. All these features are summarized in the best fit model

$$A(t) = A_0 \left[f_s^t e^{-(\sigma_s^2+\sigma_n^2)t^2/2} \cos\gamma B_s t + f_m^t e^{-t/T_2} \cos\gamma B_m t + f_m^\ell e^{-t/T_1} \right]. \quad (65)$$

In this equation f_s^t is the transverse fraction associated to the muons that experience a local field B_s dominated by the vortices diamagnetic shift (i.e. by the superconductive behaviour), associated to a damping rate σ_s (the nuclear contribution σ_n is very small, nevertheless it has been subtracted in the following analysis). The developing below T_N of spontaneous, randomly oriented AF internal fields, originates the transverse and longitudinal fractions f_m^t and f_m^ℓ, the former precessing a frequency dictated by the composition of the external field

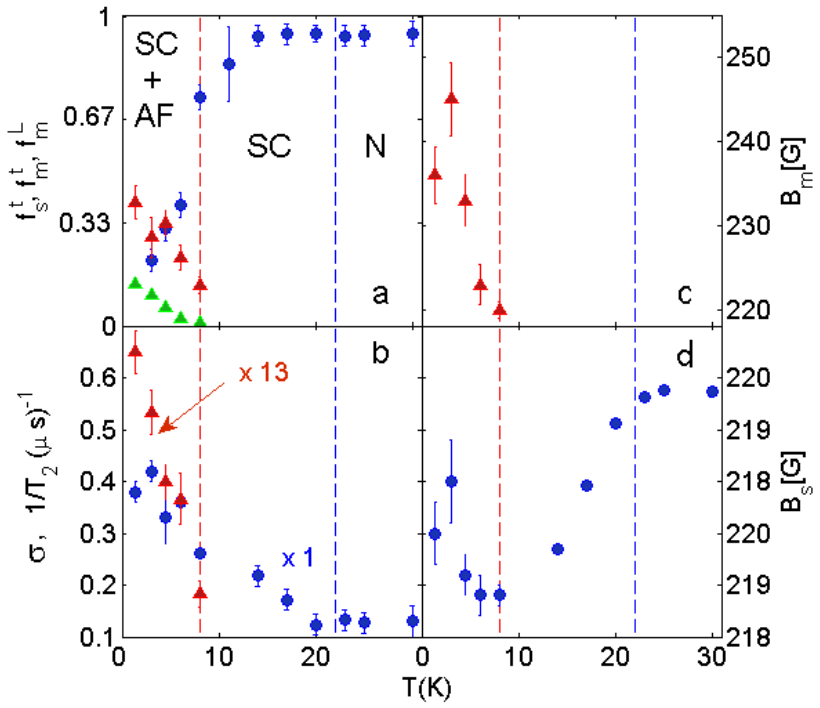

Figure 76: Temperature dependence of the fit parameters of Eq. 65 for a sample of the Ca5% series, with h=0.07. Blue, red, and green marks indicates respectively the parameters associated with the first, second anf third term of Eq. 65. Here $\sigma = \sqrt{\sigma_s^2 + \sigma_n^2}$.

with the spontaneous AF.

Most of the parameters of these fit are shown in Fig. 76. Above $T_N \approx 5.5$K only one component is present (i.e. $f_s^t = 1, f_m^t = f_m^\ell = 0$). In this regime panel d shows a clear diamagnetic shift of the local field, and panel b shows the flux line lattice damping, both arising below T_c. The superconducting carrier density n_s is extracted in this range. Below T_N the field distribution is heavily influenced by the appearance of an internal field (panel c), all three components are present, and it is impossible to extract reliably the parameter n_s. For a representative series of samples the temperature dependence of the damping parameter σ_s is shown in Fig. 76. The best fit follows Eq. 50, yielding the low temperature extrapolation which provides n_s at $T = 0$ K.

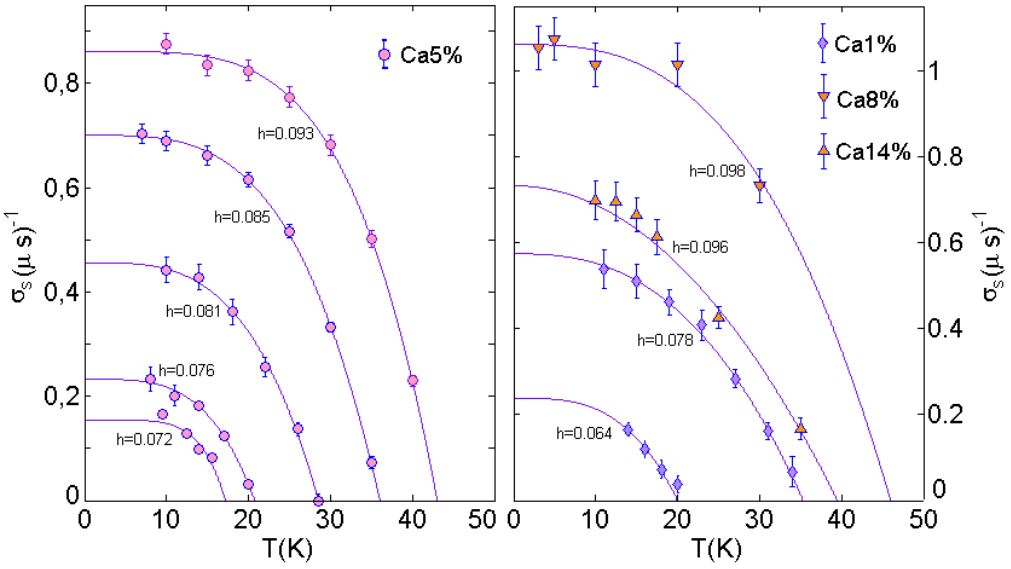

Figure 77: Temperature dependence of σ_s for a number of samples. The best fits follow Eq. 50.

5.5.4.2 The influence of doping and disorder on the incipient superconductor

Fig. 78 plots the reduced critical temperature $T_c/T_{c,max}$ versus h, where $T_{c,max}$ is the maximum transition temperature of each calcium series, at optimum doping [106]. This is a rescaled zoom projection of the 3D plot of Fig. 71 that shows beyond doubts that the onset of superconductivity strongly depends on x, i.e. on disorder. Many authors, starting from [122], assume that cuprates display a universal T_c versus h behaviour and this figure shows that it is definitely not the case. A similar situation was drawn in [123] in $Ca_xLa_{1.25}Ba_{1.75-x}Cu_3O_{6+y}$.

The dependence of T_c on $\sigma_0 \propto n_s/m^*$ is shown in Fig. 79 in the classical lay-out of the Uemura plot (see Sec. 1.5). The plot of the transverse relaxation rate vs. oxygen content,

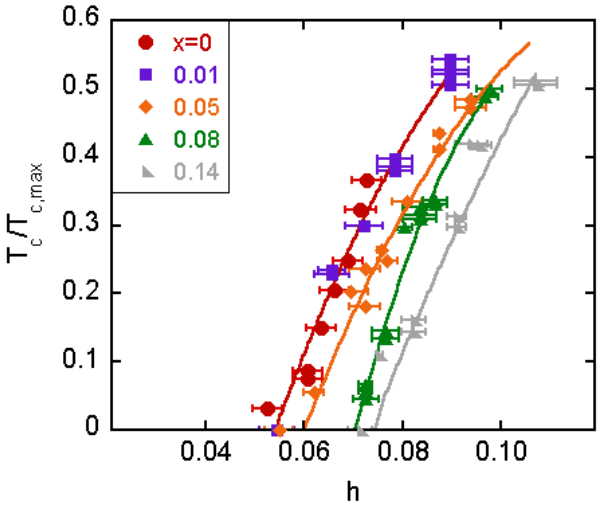

Figure 78: Scaling of transition temperatures with RT total holes (see Sec. 5.3): $T_c/T_{c,max}$ does not scale with total hole content, h. Here $T_{c,max} = 93, 92, 91, 89$ and 87 K, respectively for $x = 0, 0.01, 0.05, 0.08$ and 0.14 are data from [106].

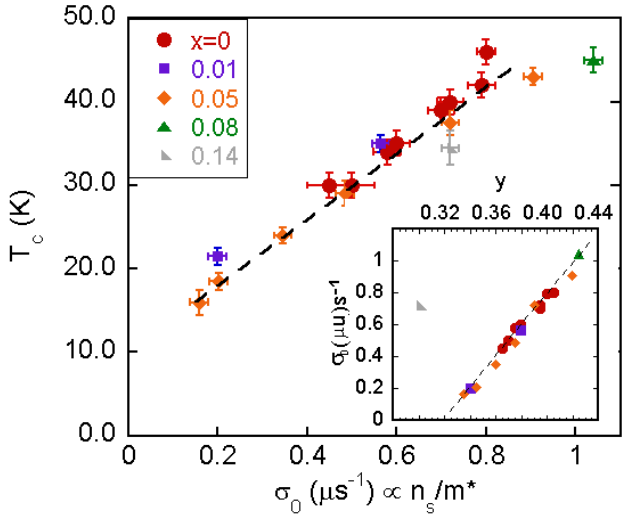

Figure 79: Scaling of transition temperatures with transverse relaxation rate: T_c does scale with the μSR linewidth, σ_0, proportional to the supercarrier density, n_s. Inset: the μSR linewidth vs oxygen content. The samples for $0 < x < 0.08$ collapse on the same line which yields to $\sigma_0 \propto n_s/m* \propto y$ (see text), i.e. only the oxygen hole fraction h_O contribute to the supercarrier density for low calcium content.

$\sigma_0 \propto n_s/m^*$, displayed in the inset of Fig. 79, shows that all samples with calcium content $0 < x < 0.08$ collapse on the same line, i.e. the dependence of n_s on y is linear (by assuming a constant m^* [93]). Since also holes injected by oxygen scale with y (see Fig. 54), the two

linear relations imply that a fraction of holes proportional to $x/2$ per CuO_2 plane does not contribute to superconductivity in this regime.

Chapter 6

Discussion

In the following Sections I discuss the main experimental findings of the previous Chapter. In Sec. 6.1.1 the negligible effect of the Nd and Eu substitutions (as opposed to Ca) on both the magnetic and superconducting behaviour of pure YBCO is remarked, hence in the following three sections the clean limit will be considered first. In Sec. 6.1.2 a debate about the main features of the CGS phase leads its identification with the low temperature magnetic regime of clean limit cuprates that we experimentally determined in the previous chapter, and that we propose to call quenched antiferromagnet (QAF), as opposed to the thermally activated antiferromagnet (TAAF) characteristic of high temperatures. A plausible explanation of the behaviour of such phases upon doping is proposed in Sec. 6.1.3 and Sec. 6.1.4, while in Sec. 6.1.5 the existence of a QCP characteristic of the intrinsic phase diagram is underlined. Finally, in Sec. 6.2 the dirty limit case is analyzed, pointing out the specific role of the Coulomb potential on the high temperature orders, both AF and SC.

6.1 Toward the clean limit

6.1.1 Influence of isovalent disordered substitutions

In order to disentangle structural and Coulomb disorder we compare isovalent (Eu,Nd) and heterovalent (Ca) substitutions. Based on the ionic radii [124] - Y^{3+} (101.9 pm), Eu^{3+} (106.6 pm), Nd^{3+} (110.9 pm), Ca^{2+} (112 pm) - we evaluate the cation mismatch via the radius standard deviation, $\sigma_r = 1.3, 2.4, 2.2$ pm for Eu8%, Nd7.5% and Ca5%, respectively. Our data show that the Néel and superconducting transitions of the Nd and Eu substituted samples are identical within experimental error to those of the pure compound (Fig. 69), whereas Ca5%, with the same σ_r as Nd7.5%, displays a markedly different behaviour, as we shown in [47, 96] and in Sec. 6.2 in a more complete and exhaustive fashion.

We conclude that, for dilute Y replacements, isovalent disorder is by far less effective than

heterovalent disorder. As a consequence the three families Y100%, Eu8% and Nd7.5% equivalently identify the cuprate system closest to the clean limit, and in the discussion of the following sections we shall refer generically to them as the YBCO system.

6.1.2 Quenched and thermally activated AF

Our data establish a coherent and systematic picture of the AF YBCO phase which is characterized by two distinct regimes, re-entrant and thermally activated, in agreement with previous indications [30] on the magnetic behavior of $La_{2-x}Sr_xCuO_4$.
A first feature of the low temperature re-entrant regime is the recovery of the full 2DHAF moment, μ_{2D}, as it is shown in Fig. 67c (m_R, solid curve). This finding agrees with the increasing of the elastic neutron scattering at low temperatures [29]. In $La_{2-x}Sr_xCuO_4$ the incommensurate peaks [33] observed above $h_c = 0.02$ are tentatively interpreted in terms of a spiral spin state [31]. In $YBa_2Cu_3O_{6+y}$ the experimental evidence of incommensurate order is missing, but similar magnetic correlations are detected [45]. Stripes or spiral spin structures are locally collinear, in-plane and staggered, hence they satify also the conditions imposed by the muon results (Sec. 5.5.1) and they can provide the large local moments that we detect.

Another feature of the re-entrant state is the narrow width of the observed moment distribution Δm_R, that reaches the value 0.4 only close to the critical point h_{cR}, as shown in Fig. 67d. Notice that narrow widths and staggered in-plane collinearity extend also to the CSG phase coexisting with superconductivity, for $h_c \leq h \leq h_{cR}$. This is not what is expected of a canonical spin glass, where muons typically [125] measure $\Delta m \approx 1$ and randomly oriented local fields.

The main signature of the so called CSG phase is the change from a rather large slope of the transition temperature, dT_N/dh, below h_c, to a very modest slope dT_g/dh above. Notice that T_A, the activation temperature defined by Eq. 64, shares this same modest slope, and the two temperatures, T_A and T_g follow the same curve in Fig. 70. This may be simply understood in terms of the disappearance of the high temperature, activated regime, above the critical density h_c, while the magnetic ground state detected in the re-entrant regime survives as shown by the continuous behavior of $m_R(h)$ and $\Delta m_R(h)$ across h_c, Fig. 67 (c and d). This leads us to identify *the same ground state* in the CSG phase coexisting with superconductivity ($h_c \leq h \leq h_{cR}$) and in the re-entrant regime of the antiferromagnet, a common state that we propose to dub quenched antiferromagnet (QAF), in contrast with the thermally activated antiferromagnet, henceforth TAAF, established only above the crossover temperature, for $h < h_c$.

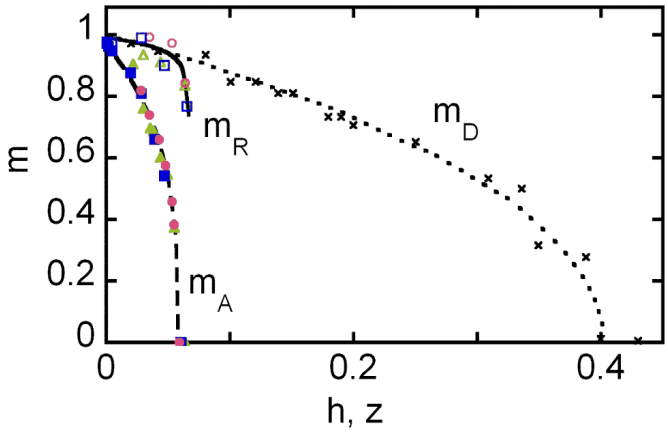

Figure 80: Reduced moments m_R and m_A (same as Fig. 67c) compared with theory [126] (dotted line) and experiments [127] on $La_{2-x}Sr_xCu_{1-z}Zn_zO_4$ (crosses).

6.1.3 QAF: magnetic site dilution

Insight on the nature of the QAF state is provided by Fig. 80 which shows that m_R is actually following the initial slope typical of magnetic site dilution in cuprates [126] (dotted line). A similar conclusion can be derived from recent low temperature muon results [120] in $Ca_xLa_{1.25}Ba_{1.75-x}Cu_3O_{6+y}$. One way to look at this is to suppose that in the re-entrant regime holes are localized, and each of them in first approximation cancels one Cu spin, leading to magnetic dilution with $z = h$.

The dilution theory has recently found [126] excellent agreement with available $La_{2-x}Sr_x$-$Cu_{1-z}Zn_zO_4$ data [127,128,129] (crosses in Fig. 80), by taking into consideration a small additional frustrating effect of the local Zn impurity that slightly reduces the effective coupling. Also localized holes give rise to a frustration, [130] in this case of dipolar nature, that is often indicated as the cause of the dramatic reduction of $T_N(h)$. Our $m_R(h)$ data in Fig. 80, however, follow very closely the dotted curve of [126] until the magnetic component disappears, showing that the leading phenomenon at low temperature is moment dilution and not frustration. This result indicates that holes, either by incoherent freezing or by self-organization, produce only a rather moderate frustration in the AF background of the QAF state.

6.1.4 TAAF: frustration or finite-size reduction

The slope of the thermally activated moment $m_A(h)$ is much steeper than the predictions of the dilution theory, even at extremely low doping, as the dashed and dotted curves show in Fig. 80. It is noteworthy that the vanishing of m_A, the divergence of Δm_A (Fig. 67c and d) and the suppression of T_N (Fig. 69), all occur at the same critical density h_c, thus linking all these properties to the specific TAAF phase alone.

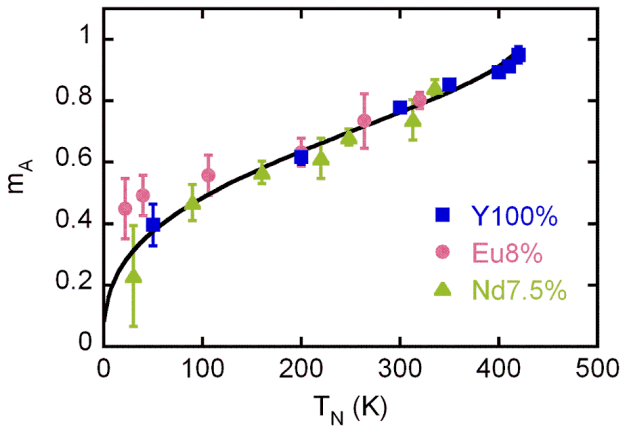

Figure 81: Scaling of the reduced moment in the activated regime, m_A, with T_N (for the solid line see the text).

Figure 81 shows that the activated moment $m_A(h)$ and $T_N(h)$ scale roughly linearly with each other over a large range of h (the solid line is obtained by plotting the previously defined functions $m_A(h,\infty)$ vs. $T_N(h)$ with h as an implicit parameter). It implies that both m_A and T_N scale with an effective exchange coupling $J_{eff}(h)$, strongly reduced by the activated process, either by finite-size effects [30] or by a very large frustration, [26, 131] much larger than that present in the re-entrant regime.

The reduced moment in the TAAF state follows the phenomenological fit of Eq. 64. Nominally, this fit justifies the low temperature regime in terms of hole localization. Here the muon is directly sensitive only to spin dynamics, hence we cannot actually prove *directly* that charges freeze as well. Freezing processes with similar low energy scales are detected also by T_1^{-1} relaxations in μSR [19, 35] and in NQR [38, 132] (the latter being sensitive also to charge dynamics) in $La_{2-x}Sr_xCuO_4$ and in $YBa_2Cu_3O_{6+y}$ as well.

Direct evidence that thermal activation regards also charge degrees of freedom comes from transport, where low temperature variable range hopping [15, 133] is detected both in dirty $La_{2-x}Sr_xCuO_4$ and in clean $YBa_2Cu_3O_{6+y}$, even at very low hole densities [40]. The energy scale of charge activation is comparable to the one we observe here (resistivity at the lowest doping in [40], $T_N = 380$ K, shows a low temperature divergence starting below 70 K). Transport experiments determine also that the mean free path ℓ is extremely short, much shorter than the inverse Fermi wave vector k_F^{-1}, but samples still display a metallic transport character [15] even at very low hole densities, which sounds like a paradox. The relation $k_F^{-1}\ell \sim 1$ defines the Mott-Ioffe-Regel limit, below which a metal insulator transition should occur. This is a long standing open issue in high-T_c cuprates. Our data simply show that the onset of metallic transport coincides with the moment reduction which consolidates the association of thermal activation with charge carriers implied by Eq. 64.

To conclude this section I wish to discuss qualitatively the connection between either spiral states or stripes and the reduction of $T_N(h)$.

If thermally activated holes determine directly the reduction of m in the TAAF state they must be responsible of a much larger frustration than independently localized holes. Such a view could be reconciled with recent extensions of the spiral model [31], where increasing hole localization lengths, κ^{-1}, are shown to reduce the staggered moment very effectively. The same approach successfully accounts for activated hole transport [134, 135], i.e. for the effect of spin texture on carrier mobility, but none has yet taken in due consideration the reverse effect of hole motion on spin texture, which is very relevant, as we show.

The two-regime-behavior of Fig. 68 would then suggest that the localization length is not temperature independent in cuprates: while a rather large length κ^{-1} (cfr. the value of 100 pm quoted in [31] for $La_{2-x}Sr_xCuO_4$) is appropriate for the thermally activated regime, a smaller length would be characteristic of the QAF state. Such a temperature-dependent localization scale suggests that at very low temperature the effects of charge localization in a lightly doped Mott-Hubbard insulator are not fully captured by the standard impurity model of doped semiconductors investigated so far in the literature.

However, as we have noted below Eq. 64, the fit of the muon measurements to this function by itself does not rule out alternative stripe based ideas. For instance a similar connection with thermally activated hole density could emerge considering stripe domains of finite length and with rather large $d = 1/2h$ separation [136] at the low densities considered here. In these conditions metallic 1D stripes would not percolate across the domains, whereas the antiferromagnetic regions would. Thermally activated hopping would then switch the system to the opposite condition of percolation for transport and separation of independent magnetic clusters, at the same time. This process is already favoured by the reduced effective exchange across the metallic 1D stripe, and it would lead to finite-size reduction of both m and T_N.

Summarizing, both spirals and stripes could qualitatively justify the YBCO μSR results, but only further theoretical work can determine if either of these hypotheses reproduces the observed crossover and the associated large change in the static local moment.

6.1.5 A Quantum Critical Point

Another important result of the present work is that the critical value, $h_c = 0.056(2)$, found for the suppression of $T_N(h)$ and $m_A(h)$, coincides with the critical value for the onset of $T_c(h)$, $h_s = 0.056(2)$. Both values agree within our errorbars with a recent very careful single crystal determinations [137] of $h_s = 0.0539(1)$. According to our data also $T_N(h)$, in the YBCO clean limit, follows a parabolic behavior analogous to that of $T_c(h)$ [138, 110], and very different from theoretical predictions [131]. Notice that older systematic results, [27, 28] reported only vs. oxygen content, without hole doping calibration, could not provide such

information. Therefore our results indicate that if superconductivity and the TAAF state were the only competing orders, $h_c = h_s$ would represent a true quantum critical point (QCP). The critical density is rather lower than that more often indicated for a QCP in cuprates [139], but other authors [140] have considered a similar additional location. The real-world system however does not develop the QCP, because it switches instead to the QAF ground state throughout a wide doping range, from $h \approx 0$ to well past the onset of superconductivity. Additional evidence on this point comes from the Ca work discussed in the next section.

6.2 Dirty-limit effects on the QAF, TAAF and SC states

The projection of the three dimensional phase diagram displayed in Fig. 71 reveals a broad green insulating QAF region, spanning from the parent compound to the so called cluster spin glass. In the QAF, doping acts mostly as simple magnetic-site dilution. The finite temperature linear boundary of this region is common to all samples, dirty and clean, independent of whether it marks the crossover to the ordered TAAF phase or the disappearance of any magnetic order. Small deviations from the linear $T_g(h)$ consist in an extension to higher doping of the magnetic phase for the most disordered samples. This is in agreement with theoretical predictions [121] indicating that disorder stabilizes magnetism coexisting with superconductivity.

In Sec. 6.1.2 we already identified a unique QAF magnetic state in the clean compounds. This identification *extends therefore to the CSG state characteristic of the dirty compounds.* This state is not a spin glass, as it is indicated by the clear low temperature oscillation observed at low, intermediate and high doping in Fig. 72. Such oscillation with a reduced damping $\Delta B/B \leq 0.3$ are characteristic of well ordered phases, in contrast with typical spin glasses, where overdamping is due to a very broad distribution of local fields [125], with $\Delta B/B \gtrsim 1$ (i.e. width comparable to the mean value). We propose to abandon the spin glass terminology for cuprates, recognizing that earlier reports [33,42,44,130,140,141,142] identify an inhomogeneous, but not truly glassy magnetic state.

The common boundary marks the transition from the insulating QAF to a bad metal state (Sec. 6.1.4) as determined by transport measurements [15, 143]. Note that the high temperature metallic-like behavior is common to the whole doping range (antiferromagnetic, paramagnetic as well as superconducting samples). The distinction between insulating QAF and bad metal TAAF shows up also in the behaviour of the magnetic moment that we have presented in Fig. 74 for two cross sections of the phase diagram at constant doping ($h \approx 0.03$ and $h \approx 0.04$). The moment m_R in the low temperature regime is constant vs. x (in each panel, b, d), and very weakly h-dependent (across the two panels), in agreement with the

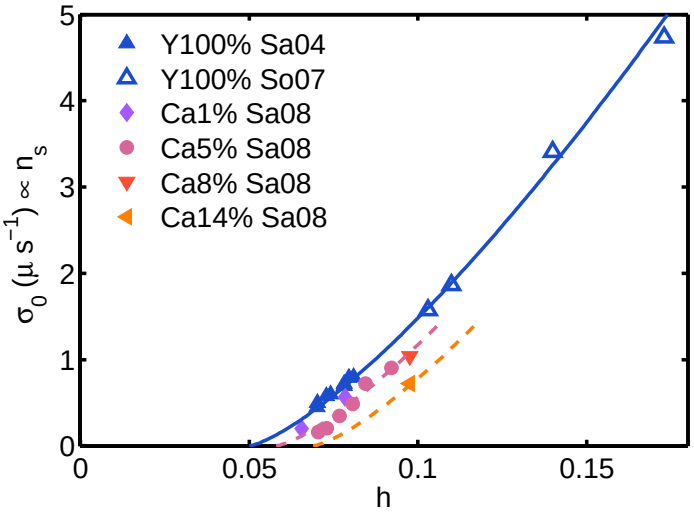

Figure 82: Dependence on hole doping of the $T = 0$ μSR relaxation rate $\sigma \propto n_s$ from TF-μSR data of Refs. [12, 47, 144], respectively for Sa04, Sa08, So07. Solid curve from Fig. 8 of Ref. [144]; dashed curves rigidly shifted.

magnetic-site dilution regime 6.1.3 appropriate for this truely insulating, localized-moment state, as in clean $YBa_2Cu_3O_{6+y}$.

A totally different conclusion applies to the TAAF regime, where the moment m_A is strongly dependent both on x and h, due to the peculiar topology of spin and mobile holes in the TAAF, as discussed in Sec. 6.1.4. Disorder appears to enhance the suppression of the TAAF order, amplifying the disruptive effect of thermal activation. Accordingly, the behaviour of the widths is respectively disorder dependent for Δm_A and independent for Δm_R.

Let me now consider the effect of disorder on the superconducting side. Our results show that in heavily underdoped compounds additional holes transferred from Ca participate to the RT thermopower (Fig. 54b) with $h_{Ca} \propto x$. The inset in Fig. 79 however shows that their contribution disappears from coherent conduction at low temperatures: whereas holes transferred from Cu(1)O chains contribute both to RT transport (above the threshold concentration $y_t \approx 0.15$ $h_O \propto y - y_t$) and to superconducting properties (above the critical concentration $y_c = 0.3$, $n_s \propto \sigma_s \propto Tc \approx k(y - y_c)$), the Ca holes do not take part in the latter. Since pair-breaking does not account for this effect, Ca-doped holes behave *as if* they were thermally quenched.

Before concluding, we briefly recall that in the phase diagram to the right of the QCP, disorder raises the threshold $h_s(x)$ for the onset of a superconducting condensate n_s. This quantity is proportional to the relaxation rate σ_0 measured in transverse field (TF) μSR, which is shown in Fig. 82, that summarizes our measurements in a field of 20 mT on the

same samples we have investigated in [47]. The open symbols and the solid line represent the $YBa_2Cu_3O_{6+y}$ data and their interpolation from Ref. [144](Sonier 2007), rescaled to polycrystalline values [93] and to low fields (Fig. 6 of Ref. [144]). The Y100% data fall on the same curve. For larger values of x the data and their dashed interpolation shift to the right, indicating that Coulomb disorder suppresses both T_c and the superconducting order parameter $n_s \propto \sigma_0$ by reducing the hole density available for superconductivity.

This is a (nearly) symmetric effect to the suppression of T_N and of the related magnetic order parameter m_A on the left of the QCP, where the first order transition induced by disorder precipitates all cuprates from the bad-metal TAAF regime into the underlying QAF insulating state, at a Ca dependent hole density $h_c(x)$ (See Fig. 74c). In this sector of the phase diagram the main effect of the increasing disorder appears to be a lowering of the threshold $h_c(x)$ for the suppression of TAAF magnetism. Disorder seems to be simply unveiling the intrinsic QAF behaviour, by pushing aside the metallic AF and SC states from the hidden QCP. Notice that whereas disorder suppresses both order parameters, it does not modify the metallic character of high temperature transport [15].
The boundary of the QAF phase in Fig. 71b is the same for all x values, at least up to $h = 0.075$, indicating that most of this phase is quite insensitive to disorder. This is an argument against a cluster spin glass introduced by disorder [16]. The unique $T_g(h)$ and the related $T_A(h)$ rather indicate an intrinsic origin, connected to the thermally activated crossover [95] in the self organized charge and spin fabric (spin spirals [145] and/or stripes [116]) of the doped Mott-Hubbard system.

Summarizing, the behaviour in the whole phase diagram agrees with the following simple notions, referred to Fig. 71b. Charge localization characterizes the green region of the phase diagram, where the insulating QAF magnetism is just diluted by doping and almost insensitive to disorder. The remaining regions correspond to a bad metal state, where the TAAF and the SC compete. The bad metal appears by thermal activation on the left of the QCP, but it is one of the two $T = 0$ ground state on the right, where SC sets in. The bad metal is very sensitive to charged impurity disorder, leading to the suppression of both its competing order parameters, but not of its bad metal character. We finally notice that a line of first order transitions $h_c(x)$ terminates from the left in a second order QCP. The steeper $h_s(x)$ curve represents the onset of superconductivity in the regime of (nanoscopic) phase separation, hence a corresponding first order transition line may exist farther to the right. This simple description of the interplay between disorder and doping, with two first order lines terminating at the same QCP, awaits a full theoretical justification.

Conclusions

I conclude my thesis by summarizing the main results for the clean and dirty limit cuprates.

First of all we have extensively investigated YBCO in the antiferromagnetic low doping region as a model for the clean limit cuprates. Since the influence of disorder induced by Nd and Eu is found to be negligible, we extract the parameters of the low temperature re-entrant and of the thermally activated regimes from the whole set of data. The crossover between these two regimes is undoubtedly associated with the thermal activation of both spin and charge degrees of freedom. This is implemented in a single phenomenological model for the temperature and doping dependence of the reduced moment $m(h,T)$, which fits our data throughout the entire investigated range.

Our analysis leads to the identification of a common ground state for very different doping regimes at the two sides of the metal-insulator transition, the re-entrant antiferromagnetic phase (on the left) and the so-called cluster spin glass phase coexisting with superconductivity (on the right). Since this unique ground state shows characteristics of a well ordered phase, not distinctive of a disordered spin glass, we dub this unique state a quenched antiferromagnet (QAF).

In the QAF state the ordered magnetic moment is subject to negligible frustration and it follows the same trend of magnetic site dilution. Conversely the fast drop of $T_N(h)$ and of the staggered moment, $m_A(h)$ are characteristic of the thermally activated antiferromagnetic phase (TAAF). Since the AF superexchange itself is not reduced by doping this indicates that a mechanism leading to strong frustration must be present. I have presented a qualitative discussion of the possible connection between the frustration in the TAAF state and either spiral states or stripes.

Furthermore, we indicate that the main boundaries in the clean-limit phase diagram, describing the two main order parameters, magnetic and superconducting, both follow parabolic curves, sharing a zero temperature intersection at $h = h_c = h_s$. This behaviour identifies at $h_c = 0.056$ a quantum critical point for the cuprates clean limit. The QCP is then superseded by the QAF behavior of the real-world compound at low temperatures.

The dirty limit case is defined by the Coulomb perturbation due to the controlled Ca sub-

stitutions in the proximity of the CuO_2 layers. Here the identification of the low temperature magnetic states with the QAF extends to the window of pure CSG state characteristic of the dirty compounds. This state is unique, and common to both the clean and dirty limits, and is characterized by charge localization and a magnetism just diluted by doping and almost insensitive to disorder.

On the contrary the high temperature states, i.e. the TAAF and SC regimes, are strongly influenced by the Coulomb-impurity-driven disorder introduced by Ca, that progressively unveils the underlying QAF. On the left side of the QCP, the suppression of the TAAF state appears to be enhanced by disorder, that amplifies the disruptive effect of thermal activation. It suddenly falls the TAAF state into the underlying QAF via a first order transition, pushing aside the relative critical hole concentration $h_c(x)$ proportionally to x.

On the right side of the QPC the effect of disorder appears to be nearly symmetric. It raises the threshold $h_s(x)$ for the onset of a superconducting condensate n_s, by reducing the hole density available for superconductivity. However all the holes injected in the system contribute to the room temperature properties, indicating again some form of charge carriers temperature activation, hidden to resistivity measurements by the superconductor.

It is interesting to note that whereas disorder suppresses both TAAF and SC, it does not modify the metallic character of high temperature transport, corresponding to the so called bad metal state. This state appears by thermal activation on the left of the QCP, but it is one of the two $T = 0$ ground states on the right, where SC sets in. For low temperatures the bad metal is very sensitive to charged impurity disorder, leading to the suppression of both its competing AF and SC order parameters, but not of its bad metal character.

We have therefore produced a 3D-phase diagram, where the additional Coulomb disorder axis x, disentangled from doping, is shown to be a fundamental ingredient in the description of such complex systems.

Bibliogrphy

[1] J.G. Bednorz and K.A. Müller. *Z.Phys.B*, 64(189), 1986.

[2] Y. J Gavaler. "Superconductivity in NB-Ge films above 22 K". *Appl. Phys. Lett. 23, 480*, 23:105, 1973.

[3] H. Shaked, P.M Keane, J.C. Rodriguez, F.F. Owen, R.L. Hitterman, and J.D. Jorgensen. *"Crystal Structures of the High-T_c Superconducting Copper-Oxides"*. Elsevier Science B.V., 1994.

[4] C. N. R. Rao, P. Ganguly, A. K. Raychaudhuri, R. A. Mohan Ram, and K. Sreedhar. "Identification of the phase responsible for high-temperature superconductivity in YBaCu oxides". *Nature*, 326:856 – 857, 1987.

[5] M. K. Wu, J. R. Ashburn, C. J. Torng, P. H. Hor, R. L. Meng, L. Gao, Z. J. Huang, Y. Q. Wang, and C. W. Chu. "Superconductivity at 93 K in a new mixed-phase Y-Ba-Cu-O compound system at ambient pressure". *Phys. Rev. Lett.*, 58(9):908–910, Mar 1987.

[6] Masatoshi Imada, Atsushi Fujimori, and Yoshinori Tokura. "Metal-insulator transitions". *Rev. Mod. Phys.*, 70(4):1039–1263, Oct 1998.

[7] Masao Ogata and Hidetoshi Fukuyama. "The tJ model for the oxide high-Tc superconductors". *Reports on Progress in Physics*, 71(3):036501, 2008.

[8] F. C. Zhang and T. M. Rice. "Effective Hamiltonian for the superconducting Cu oxides". *Physical Review B*, 37:3759–3761, 1988.

[9] D. N. Basov and T. Timusk. "Electrodynamics of high-T_c superconductors". *Rev. Mod. Phys.*, 77(2):721–779, Aug 2005.

[10] V. J Emery, S. A Kivelson, and H. Q Lin. "Phase separation in the t-J model". *Phys. Rev. Lett.*, 64(4):475–478, 1990.

[11] J. M. Tranquada, B. J. Sternlieb, J. D. Axe, Y. Nakamura, and S. Uchida. "Evidence for stripe correlations of spins and holes in copper oxide superconductors". *Nature London*, 375:561–563, 1995.

[12] S. Sanna, G. Allodi, G. Concas, A. D. Hillier, and R. De Renzi. "Nanoscopic Coexistence of Magnetism and Superconductivity in $YBa_2Cu_3O_{6+x}$ Detected by Muon Spin Rotation". *Phys. Rev. Lett.*, 93(20):207001, Nov 2004.

[13] A. Weidinger, Ch. Niedermayer, A. Golnik, R. Simon, E. Recknagel, J. I. Budnick, B. Chamberland, and C. Baines. "Observation of magnetic ordering in superconducting $La_{2-x}Srx CuO_4$ by muon spin rotation". *Physical Review Letters*, 62(1):102–105, 1989.

[14] A. T Savici, Y. Fudamoto, I. M Gat, T. Ito, M. I Larkin, Y. J Uemura, G. M Luke, K. M Kojima, Y. S Lee, M. A Kastner, R. J Birgeneau, and K. Yamada. "Muon spin relaxation studies of incommensurate magnetism and superconductivity in stage-4 La_2CuO_4.11 and $La_{1.88}Sr_{0.12}CuO_4$". *Phys. Rev. B*, 66(1):014524, July 2002.

[15] Yoichi Ando, A. N. Lavrov, Seiki Komiya, Kouji Segawa, and X. F. Sun. "Mobility of the Doped Holes and the Antiferromagnetic Correlations in Underdoped High-Tc Cuprates". *Physical Review Letters*, 87(1):017001, 2001.

[16] Elbio Dagotto. "Complexity in Strongly Correlated Electronic Systems". *Science*, 309(5732):257–262, 2005.

[17] G. Alvarez, M. Mayr, A. Moreo, and E. Dagotto. "Areas of superconductivity and giant proximity effects in underdoped cuprates". *Physical Review B*, 71(1):014514–7, 2005.

[18] H. Alloul, J. Bobroff, M. Gabay, and P. J. Hirschfeld. "defects in correlated metals and superconductors". *Reviews of Modern Physics*, 81(1):45–64, 2009.

[19] C.H. Niedermayer, C. Bernhard, T. Blasius, A. Golnik, A. Moodenbaugh, and J.I. Budnick. "Common Phase Diagram for Antiferromagnetism in $La_{2-x}Sr_xCuO_4$ and $Y_{1-x}Ca_xBa_2Cu_3O_{6+y}$ as Seen by Muon Spin Rotation". *Phys. Rev. Lett.*, 80:3843–3846, April 1998.

[20] Y. Endoh, K. Yamada, R. J. Birgeneau, D. R. Gabbe, H. P. Jenssen, M. A. Kastner, C. J. Peters, P. J. Picone, T. R. Thurston, J. M. Tranquada, G. Shirane, Y. Hidaka, M. Oda, Y. Enomoto, M. Suzuki, and T. Murakami. "Static and dynamic spin correlations in pure and doped La_2CuO_4". *Physical Review B*, 37(13):7443, 1988.

[21] R. J. Birgeneau, H. J. Guggenheim, and G. Shirane. "Neutron Scattering Investigation of Phase Transitions and Magnetic Correlations in the Two-Dimensional Antiferromagnets K_2NiF_4, Rb_2MnF_4, Rb_2FeF_4". *Physical Review B*, 1(5):2211, 1970.

[22] N. D. Mermin and H. Wagner. "Absence of Ferromagnetism or Antiferromagnetism in One- or Two-Dimensional Isotropic Heisenberg Models". *Phys. Rev. Lett.*, 17(22):1133–1136, Nov 1966.

[23] Sudip Chakravarty, Bertrand I. Halperin, and David R. Nelson. "Low-temperature behavior of two-dimensional quantum antiferromagnets". *Physical Review Letters*, 60(11):1057, 1988.

[24] Rajiv R. P. Singh. "Thermodynamic parameters of the T=0, spin-1/2 square-lattice Heisenberg antiferromagnet". *Physical Review B*, 39(13):9760, May 1989.

[25] B. Keimer, N. Belk, R. J. Birgeneau, A. Cassanho, C. Y. Chen, M. Greven, M. A. Kastner, A. Aharony, Y. Endoh, R. W. Erwin, and G. Shirane. "Magnetic excitations in pure, lightly doped, and weakly metallic La_2CuO_4". *Physical Review B*, 46(21):14034, 1992.

[26] Amnon Aharony, R. J. Birgeneau, A. Coniglio, M. A. Kastner, and H. E. Stanley. "Magnetic phase diagram and magnetic pairing in doped La_2CuO_4". *Physical Review Letters*, 60(13):1330, 1988.

[27] J. H. Brewer, E. J. Ansaldo, J. F. Carolan, A. C. D. Chaklader, W. N. Hardy, D. R. Harshman, M. E. Hayden, M. Ishikawa, N. Kaplan, R. Keitel, J. Kempton, R. F. Kief, W. J. Kossler, S. R. Kreitzman, A. Kulpa, Y. Kuno, G. M. Luke, H. Miyatake, K. Nagamine, Y. Nakazawa, N. Nishida, K. Nishiyama, S. Ohkuma, T. M. Riseman, G. Roehmer, P. Schleger, D. Shimada, C. E. Stronach, T. Takabatake, Y. J. Uemura, Y. Watanabe, D. Ll. Williams, T. Yamazaki, and B. Yang. "Antiferromagnetism and superconductivity in oxygen-deficient $YBa_2Cu_3O_{6+x}$". *Physical Review Letters*, 60(11), 1988.

[28] J. Rossat-Mignod, L.P. Regnault, M.J. Jurgens, C. Vettier, P. Burlet, J.Y. Henry, and G. Lapertot. "Neutron scattering study of $YBa_2Cu_3O_{6+x}$ single crystals". *Physica B*, 163, 1990.

[29] J. M. Tranquada, G. Shirane, B. Keimer, S. Shamoto, and M. Sato. "Neutron scattering study of magnetic excitations in $YBa_2Cu_3O_{6+x}$". *Physical Review B*, 40(7):4503, 1989.

[30] F. Borsa, P. Carretta, J. H Cho, F. C Chou, Q. Hu, D. C Johnston, A. Lascialfari, D. R Torgeson, R. J Gooding, N. M Salem, and K. J. E Vos. "Staggered magnetization in $La_{2-x}Sr_xCuO_4$ from ^{139}La NQR and $\mu-$SR: Effects of Sr doping in the range $0 \leq x \leq 0.02$". *Physical Review B*, 52(10):7334, September 1995.

[31] A. Luscher, A. I. Milstein, and O. P. Sushkov. "Structure of the Spin-Glass State of $La_{2-x}Sr_xCuO_4$: The Spiral Theory". *Physical Review Letters*, 98(3):037001, 2007.

[32] O. P. Sushkov. "Spin spirals in underdoped $La_{2-x}Sr_xCuO_4$ $YBa_2Cu_3O_{6+y}$: Differences and similarities". *Physical Review B*, 79(17):174519–7, 2009.

[33] M. Matsuda, M. Fujita, K. Yamada, R. J. Birgeneau, Y. Endoh, and G. Shirane. "Electronic phase separation in lightly doped $La_{2-x}Sr_xCuO_4$". *Physical Review B*, 65(13):134515, 2002.

[34] Oleg P. Sushkov and Valeri N. Kotov. "Theory of Incommensurate Magnetic Correlations Across the Insulator-Superconductor Transition of Underdoped $La_{2-x}Sr_xCuO_4$". *Phys. Rev. Lett.*, 94(9):097005, Mar 2005.

[35] S. Sanna, G. Allodi, and R. De Renzi. "The freezing of spin and charge at low temperature in $YBa_2Cu_3O_{6+x}$". *Solid State Communications*, 126, 2003.

[36] C. Bucci, R. De Renzi, G. Guidi, G. Allodi, and F. Licci. "Phase separation in antiferromagnetic $YBa_2Cu_3O_{6+x}$". *Hyperfine Interactions*, 105:71–76, 1997.

[37] Francesco Coneri, Giorgio Concas, Sean Giblin, Americo Rigoldi, Samuele Sanna, and Roberto De Renzi. "Effect of the double doping mechanism on the phase diagram of $Y_{1-x}Ca_xBa_2Cu_3O_{6+y}$". *Physica B*, 404(5-7):706–709, 2009.

[38] M.H. Julien, F. Borsa, P. Carretta, M. Horvatia, C. Berthier, and C. T. Lin. "Charge Segregation, Cluster Spin Glass, and Superconductivityin $La_{1.94}Sr_{0.06}CuO_4$". *Physical Review Letters*, 83(3):604, 1999.

[39] M. A. Kastner, R. J. Birgeneau, G. Shirane, and Y. Endoh. "Magnetic, transport, and optical properties of monolayer copper oxides". *Reviews of Modern Physics*, 70(3):897, 1998.

[40] Y. Wang and N.P. Ong. "Particle-hole symmetry in the antiferromagnetic state of the cuprates". *PNAS*, 98:11091–11096, 2001.

[41] J. Lorenzana, G. Seibold, and R. Coldea. "Sum rules and missing spectral weight in magnetic neutron scattering in the cuprates". *Physical Review B*, 72(22):224511, 2005.

[42] F. C. Chou, F. Borsa, J. H. Cho, D. C. Johnston, A. Lascialfari, D. R. Torgeson, and J. Ziolo. "Magnetic phase diagram of lightly doped $La_{2-x}Sr_xCuO_4$ from ^{139}La nuclear quadrupole resonance". *Physical Review Letters*, 71(14):2323, 1993.

[43] F. C. Chou, N. R. Belk, M. A. Kastner, R. J. Birgeneau, and Amnon Aharony. "Spin-Glass Behavior in $La_{1.96}Sr_{0.04}CuO_4$". *Physical Review Letters*, 75(11):2204, 1995.

[44] M. H. Julien. "Magnetic Order and Superconductivity in $La_{2-x}Sr_xCuO_4$:a review". *Physica B*, pages 329–333, 2003.

[45] C. Stock, W. J. L. Buyers, Z. Yamani, Z. Tun, R. J. Birgeneau, R. Liang, D. Bonn, and W. N. Hardy. "Spin dynamics near the critical doping in weakly superconducting underdoped $YBa_2Cu_3O_{6.35}$ (Tc=18 K)". *Physical Review B*, 77(10):104513–20, March 2008.

[46] S. Wakimoto, S. Ueki, Y. Endoh, and K. Yamada. "Systematic study of short-range antiferromagnetic order and the spin-glass state in lightly doped $La_{2-x}Sr_xCuO_4$". *Physical Review B*, 62(5):3547, 2000.

[47] S. Sanna, F. Coneri, A. Rigoldi, G. Concas, and R. De Renzi. "Experimental evidence of two distinct charge carriers in underdoped cuprate superconductos". *Phys. Rev. B*, 77:224511–224514, 2008.

[48] F. Rullier-Albenque, H. Alloul, F. Balakirev, and C. Proust4. "Disorder, metal-insulator crossover and phase diagram in high-Tc cuprates". *European Physics Letter*, 81:37008, 2008.

[49] Michel Cyrot, Davor Pavuna. *"Introduction to superconductivity and high-Tc materials"*. World Scientific Publishing Co .Pte.Ltd., August 1992.

[50] H. F. Hess, R. B. Robinson, R. C. Dynes, J. M. Valles, and J. V. Waszczak. "Scanning-Tunneling-Microscope Observation of the Abrikosov Flux Lattice and the Density of States near and inside a Fluxoid". *Phys. Rev. Lett.*, 62(2):214–216, Jan 1989.

[51] Y. J. Uemura, V. J. Emery, A. R. Moodenbaugh, M. Suenaga, D. C. Johnston, A. J. Jacobson, J. T. Lewandowski, J. H. Brewer, R. F. Kiefl, S. R. Kreitzman, G. M. Luke, T. Riseman, C. E. Stronach, W. J. Kossler, J. R. Kempton, X. H. Yu, D. Opie, and H. E. Schone. "Systematic variation of magnetic-field penetration depth in high-T_c superconductors studied by muon-spin relaxation". *Phys. Rev. B*, 38(1):909–912, Jul 1988.

[52] Y. J Uemura. "Universal correlations, pseudo-gaps and condensation mechanism in high-T_c superconductors". *Hyperfine Interactions*, 105:35–47, 1997.

[53] Y. J. Uemura, G. M. Luke, B. J. Sternlieb, J. H. Brewer, J. F. Carolan, W. N. Hardy, R. Kadono, J. R. Kempton, R. F. Kiefl, S. R. Kreitzman, P. Mulhern, T. M. Riseman, D. Ll. Williams, B. X. Yang, S. Uchida, H. Takagi, J. Gopalakrishnan, A. W. Sleight, M. A. Subramanian, C. L. Chien, M. Z. Cieplak, Gang Xiao, V. Y. Lee, B. W. Statt, C. E. Stronach, W. J. Kossler, and X. H. Yu. "Universal Correlations between Tc and ns/m* (Carrier Density over Effective Mass in High-Tc Cuprate Superconductors". *Physical Review Letters*, 62(19):2317, May 1989.

[54] Charles Kittel. *"Introduzione alla Fisica dello Stato Solido"*. Bollati Boringhieri, 2001.

[55] D. Viterbo E. Scordari G. Gilli et al C. Giacovazzo, H.L. Monaco. *"Fundamentals of Crystallography"*. Oxford University Press, Inc, 198 madison Avenue, 10016 New York, 2002.

[56] B.D. Cullitt. *"Elements of X-ray Diffraction"*. Addison Weley Publishing Company, Reading, Massachussets, 1967.

[57] J.B. Cohen. *"Diffraction Methods in Material Science"*. MacMillan Series in Material Science, London, 1966.

[58] W. L Bragg. *Proc. Cambridge phil. Soc. 43*, 1913.

[59] R. Jenkis and R. L. Snyder. *"Introduction to X-ray Powder Diffractometery"*. John Wiley and Sons, 1996.

[60] E. W. Nuffield. *"X-ray diffraction methods"*. John Wiley and Sons, 1966.

[61] D.E. Moore and R.C. Reynolds. *"X-ray Diffraction and the Identification and Analysis of Clay Materials"*. Oxford University Press, Inc, 198 madison Avenue, 10016 New York, 1997.

[62] P. Debye and P. Sherrer. *Physikalische Zeitschrift*, 18:291–301,, 1917.

[63] W. Parrish and Philips Natuurkundig Laboratorium. *"Advances in X-ray Diffractometry and X-ray Spectrography, Contribution n. 188"* . W. Parrish editions, Centrex Publishing Company, Eindhoven, 1962.

[64] Allen C. Larson and Robert B. Von Dreele. Los Alamos National Laboratory (LANL), CCP14: Collaborative Computational Project n.14, 1985. Website http://ccp14ac.uk.

[65] H. M. Rietveld. "Line Profiles of Neutron Powder-diffraction Peaks for Structure Refinement". *Acta Crystallogr.*, 22:151–152, 1967.

[66] H. M. Rietveld. "A Profile Refinement Method for Nuclear and Magnetic Structures". *J. Appl. Crystallogr.*, 2:65–71, 1969.

[67] E. Prince et. *al*. R.A. Young, Hugo M. Rietveld. *"The Rietveld Method"*. International Union of Crystallography, Oxford University Press, 1995.

[68] M. Ashcroft and N.D. Mermin. *"Solid State Physics"*. HRW International Editions, Philadelphia, 1976.

[69] A. Barone and G. Paternò. *"Phisics and Applications of the Josephson Effect"*. Wiley-Interscience Publication. John Wiley and Sons, Inc, New York, Chicester, Brisbane, Toronto, Singapore, 1982.

[70] Quantum Design Inc. "MPMS MultiVu Application User's Manual, SQUID Detection System, 1014-110C". November 2004.

[71] S. Li Mc. Elfresh and R. Sager. "Effects of magnetic field uniformity on the measurement of superconducting samples". MPMS Application note, Quantum Design Inc, 2002.

[72] P. L. Taylor. "Comment on Seebeck Coefficient at the Curie Temperature: Specific Heat of Charge Carriers in Ferromagnets". *Phys. Rev. B*, 7(3):1197–1198, Feb 1973.

[73] J. L. Tallon, C. Bernhard, H. Shaked, R. L. Hitterman, and J. D. Jorgensen. "Generic superconducting phase behavior in high-Tc cuprates: Tc variation with hole concentration in $YBa_2Cu_3O_{7-\delta}$". *Phys. Rev. B*, 51(18):12911–12914, May 1995.

[74] T. Honma, P. H. Hor, H. H. Hsieh, and M. Tanimoto. "Universal intrinsic scale of the hole concentration in high-Tc cuprates". *Phys. Rev. B*, 70(21):214517, Dec 2004.

[75] S. D. Obertelli, J. R. Cooper, and J. L. Tallon. "Systematics in the thermoelectric power of high-T_c oxides". *Phys. Rev. B*, 46(22):14928–14931, Dec 1992.

[76] P. and A. Mascioli E. Ippoliti, C. Zeggio. *"Analisi chimica quantitativa"*. Edizioni Angelo Signorelli, 1985.

[77] D.C. Harris. *"Chimica analitica quantitativa"*. Edizioni Zanichelli, Bologna, 1991.

[78] E.H. Appelman, L.R. Morss, A.M. Kini, U. Geiser, G.W. Crabtree A. Umezawa, and K.D. Carlson. "Oxigen content of superconducting Perovskites, $La_{2-x}Sr_xCuO_y$ and $YBa_2Cu_3O_y$". *Inorganic Chemistry*, 26:3237–3239, 1987.

[79] A.I. Nazzal, V.Y. Lee, E.M Engler, R.D. Jacowitz, Y. Tokura, and J.B. Torrance. "New procedure for deretmination of $(Cu\text{-}O)^{+p}$ charge and oxygen content in high-t_c copper oxides".

[80] Y. Maeno, H. Teraoka, K. Matsukuma, K. Yoshida, K. Sugiyama, F. Nakamura, and T. Fujita. "Simple and high reliable method for determination of oxygen content in high-Tc cuprates". *Physica C*, 185-189:587, 1991.

[81] A. Knizhnik, Y. Direktovich, D. Goldschmidt, and Y. Eckstein. "Determination of oxygen stoichiometry in a small mass of cuprate superconductor by iodometric microtitration". *Supercond. Sci. Technol.*, 6:209, 1993.

[82] A. Schenck. "Muon Spin Rotation Spectroscopy: Principles and Applications in Solid State Physics", 1985.

[83] Jess Brewer. "Muon spin Rotation Relaxation Resonance". *Encyclopedie of Applied Physics*, 11, 1994.

[84] A. Abragam. *"Principles of Nuclear Magnetism"*. Oxford Science Publications, New York, 1961.

[85] C. P. Slichter. *"Principles of Magnetic Resonance"*, volume 1 of *Springer Series in Solid-State Sciences*. Springer Verlag, 1989.

[86] R. Kubo and T. Toyabe. *"Magnetic resonance and relaxation"*. R. Blinc, North-Holland Phisycs Publishing, Amsterdam, 1967.

[87] R. S. Hayano, Y. J. Uemura, J. Imazato, N. Nishida, T. Yamazaki, and R. Kubo. "Zero-and low-field spin relaxation studied by positive muons". *Phys. Rev. B*, 20(3):850–859, Aug 1979.

[88] N. Bloembergen, E. M. Purcell, and R. V. Pound. "Relaxation Effects in Nuclear Magnetic Resonance Absorption". *Phys. Rev.*, 73(7):679–712, Apr 1948.

[89] S. L. Lee, S. H. Kilcoyne, and R. Cywinski, editors. *"MUON SCIENCE: muons in Physics, Chemistry and Materials"*. SUSSP and Publications and Institute of Physics Publishing, University of Edinburgh, January 1999.

[90] H. Brandt. "Magnetic field density of perfect and imperfect flux line lattices in type II superconductors. Application of periodic solutions". *Journal of Low Temperature Physics*, 73:355–390, 1988.

[91] M. Tinkhamm. "Introduction to Superconductivity", 1996.

[92] T. M. Riesman, J. H. Brewer, K. H. Chow, W. N. Hardy, R. F. Kiefl, S. R. Kreitzman, R. Liang, W. A. MacFarlane, P. Mendels, G. D. Morris, J. Rammer, J. W. Schneider, C. Niedermayer, and S. L. Lee. "Ginzburg-Landau parameter in $YBa_2Cu_3O_{6.95}$ below the irreversibility temperature as measured by μ^+-SR in high magnetic fields". *Phys. Rev. B*, 52(14):10569–10580, Oct 1995.

[93] W. Barford and J.M.F. Gunn. "The theory of the measurement of the London penetration depth in uniaxial type II superconductors by muon spin rotation.". *Physica C*, 156:515, 1988.

[94] F. James and A. Roos. "MINUIT, Function Minimization and Analysis of the Parameter Errors and Correlations". *Comput. Phys. Commun.*, 10:343, 1975.

[95] F. Coneri, S. Sanna, K. Zheng, J. Lord, and R. De Renzi. "The magnetic states of lightly hole-doped cuprates in the clean limit". arXiv:0911.5488v1 cond-mat.supr-con, Nov 2009.

[96] S. Sanna, F. Coneri, A. Rigoldi, S. Giblin, G. Concas, and R. DeRenzi. "The Quantum Crytical Point beneath cuprates explored by tuning disorder in $Y_{1-x}Ca_xBa_2Cu_3O_{6+y}$". *arXiv*, 2010.

[97] K.C. Goretta, Ira Blooma, Nan Chena, G.T. Goudeya, M.C. Hasha, G. Klassena, M.T. Lanagana, R.B. Poeppela, J.P. Singha, Donglu Shia, U. Balachandrana, J.T. Duseka, and D.W. Capone. "Calcination of $YBa_2Cu_3O_{7-x}$ powder". *Materials Letters*, 7:161, 1988.

[98] R.B. Poeppel, B.K. Flandmeyer, J.T. Dusek, and I.D. Bloom. *"Chemistry of High Temperature Superconductors"*. American Chemical Society, 1987.

[99] Variuos Authors. Several papers. *Advanced Ceramic Materials*, 2:327709, 1987.

[100] U. Balachandran, R.B. Poeppel, J.E. Emerson, S.A. Johnson, M.T. Lanagan, C.A. Youngdahl, Donglu Shi, K.C. Goretta, and N.G. Eror. ''Synthesis of a phase-pure orthorhombic $YBa_2Cu_3O_x$ under low oxygen pressure". *Materials Letters*, 61:2859–2861, 2007.

[101] P. Manca, S. Sanna, G. Calestani, V.E. Zubkus, S. Lapinskas, and E. E. Tornau. "Orthorhombic low-temperature superstructures in $YBa_2Cu_3O_{6+x}$". *Phys. Rev. B*, 46:134512, 2001.

[102] H. Fjellvig, H. Karen, P. Kjekus, A. Kofstad, and P. Norby. Acta Chem. Scand., 1988. A42 178.

[103] B. Fisher, J. Genossar, C. G. Kuper, L. Patlagan, G. M. Reisner, and A. Knizhnik. "Effects of substituting calcium for yttrium on the properties of $YBa_2Cu_3O_{7-\delta}$". *Phys. Rev. B*, 47(10):6054–6059, Mar 1993.

[104] H. Lütgemeier, S. Schmenn, P. Meuffels, O. Storz, R. Schöllhorn, Ch. Niedermayer, I. Heinmaa, and Yu. Baikov. "A different type of oxygen order in $REBa_2Cu_3O_{6+x}$ HTc superconductors with different RE ionic radii". *Physica C*, 267(3-4):191–203, 1996.

[105] K. Zheng, S.Sanna, F.Coneri, and R.DeRenzi. private communication.

[106] C. Bernhard and J.L. Tallon. "Thermoelectric power of $Y_{1-x}Ca_xBa_2Cu_3O_{7-\delta}$: Contributions from CuO_2 planes and CuO chains". *Phys. Rev. B*, 54(14):10201–10209, Oct 1996.

[107] G. V. Uimin, V. F. Gantmakherb, A. M. Neminskyb, L. A. Novomlinskyb, D. V. Shovkunb, and P. Brüllc. "Dependence of Tc on the oxygen distribution in the Cu-O chains in the high temperature ù superconductors $YBa_2Cu_3O_{6+x}$". *Physica C*, 192:481–490, 1992.

[108] R.J Cava, A.W Heawat, and Heawat E.A. "Structural anomalies, oxygen ordering and superconductivity in oxygen deficient YBa_2Cu_3O7-δ".

[109] J. R. Cooper, B. Alavi, L-W. Zhou, W. P. Beyermann, and G. Grüner. "Thermoelectric power of some high-Tc oxides". *Phys. Rev. B*, 35(16):8794–8796, Jun 1987.

[110] R. Liang, D.A. Bonn, and W.N. Hardy. "Evaluation of CuO_2 plane hole doping in $YBa_2Cu_3O_{6+y}$ single crystals". *Phys. Rev. B*, 73:180505, 2006.

[111] J. H. Brewer. private communication.

[112] H. Glückler, A. Weidinger, A. Golnik, Ch. Niedermayer, M. Rauer, R. Simon, E. Recknagel, J.I. Budnick, W. Paulus, and R. Schöllhorn. "Dependence of the magnetic ordering in $H_xYBa_2Cu_3O_y$ on the oxygen and hydrogen concentration". *Physica C 162-164*, page 149, 1989.

[113] N. Nishida and H. Miyatake. "Positive muon sites and possibility of anyons in the $YBa_2Cu_3O_x$ system". *Hyp. Int.*, 63:183–198, 1990.

[114] M. Weber, P. Birrer, F. N. Gygax, B. Hitti, E. Lippelt, H. Maletta, and A. Schenck. "Identification of μ^+-sites in the 1-2-3 compound". *Hyperfine Interactions*, 63:207–212, 1990.

[115] M. Pinkpank, A. Amato, D. Andreica, F.N. Gygax, H.R. Ott, and A. Schenck. "The effect of oxygen reduction on the magnetic properties of RE-$Ba_2Cu_3O_{6+x}$". *Physica C*, 317-318:299–303, 1999.

[116] Jan Zaanen and Olle Gunnarsson. "Charged magnetic domain lines and the magnetism of high-Tc oxides". *Phys. Rev. B*, 40(10):7391–7394, Oct 1989.

[117] D. Poilblanc and T. M. Rice. "Charged solitons in the Hartree-Fock approximation to the large-U Hubbard model". *Physical Review B*, 39(13):9749, 1989.

[118] R. I. Miller, R. F. Kiefl, J. H. Brewer, F. D. Callaghan, J. E. Sonier, R. Liang, D. A. Bonn, and W. Hardy. "Coexistence of magnetism and superconductivity in ultraclean underdoped $YBa_2Cu_3O_{6.37}$". *Physical Review B*, 73(14):144509, 2006.

[119] H. Alloul, P. Mendels, H. Casalta, J. F. Marucco, and J. Arabski. "Correlations between magnetic and superconducting properties of Zn-substituted $YBa_2Cu_3O_{6+x}$". *Physical Review Letters*, 67(22):3140, November 1991.

[120] Rinat Ofer, Amit Keren, Omar Chmaissem, and Alex Amato. "Universal doping dependence of the ground-state staggered magnetization of cuprate superconductors". *Physical Review B*, 78(14):140508–4, October 2008.

[121] Brian M. Andersen and P. J. Hirschfeld. "Breakdown of Universal Transport in Correlated d-Wave Superconductors". *Physical Review Letters*, 100(25):257003–4, June 2008.

[122] R. G. Buckley R. S. Liu M. R. Presland, J. L. Tallon and N. E. Flower. "General trends in oxygen stoichiometry effects on Tc in Bi and Tl superconductors". *Physica C*, 176:95–105, 1991.

[123] Amit Keren, Amit Kanigel, and Galina Bazalitsky. "Evidence for two fluids in cuprate superconductors from a nuclear resonance study of $(Ca_xLa_{1-x})(Ba_{1.75-x}La_{0.25+x})Cu_3O_y$". *Phys. Rev. B*, 74(17):172506, Nov 2006.

[124] R.D. Shannon. "Revised effective ionic radii and systematic studies of interatomic distances in halides and chalcogenides", 1976.

[125] Y. J. Uemura, T. Yamazaki, D. R. Harshman, M. Senba, and E. J. Ansaldo. "Muon-spin relaxation in AuFe and CuMn spin glasses". *Physical Review B*, 31(1):546, 1985.

[126] C.W. Liu, S. Liu, Y.J. Kao, A. L. Chernyshev, and A. W. Sandvik. "Impurity-Induced Frustration in Correlated Oxides". *Physical Review Letters*, 102(16):167201–4, 2009.

[127] P. Carretta, A. Rigamonti, and R. Sala. "Spin dynamics in a two-dimensional disordered S=1/2 Heisenberg paramagnetfrom ^{63}Cu NQR relaxation in Zn-doped La_2CuO_4". *Physical Review B*, 55(6):3734, 1997.

[128] O. P. Vajk, P. K. Mang, M. Greven, P. M. Gehring, and J.W. Lynn. "Quantum Impurities in the Two-Dimensional Spin One-Half Heisenberg Antiferromagnet". *Science*, 295(5560):1691–1695, March 2002.

[129] O. P. Vajk, M. Greven, P. K. Mang, and J. W. Lynn. "Neutron scattering, magnetometry, and quantum Monte Carlo study of the randomly diluted spin-1/2 square-lattice Heisenberg antiferromagnet". *Solid State Communications*, 126(1-2):93–101, 2003.

[130] N. Hasselmann, A. H. Castro Neto, and C. Morais Smith. "Spin-glass phase of cuprates". *Physical Review B*, 69(1):014424, 2004.

[131] V. Cherepanov, I.Y. Korenblit, A. Aharony, and O. E. Wohlman. "Suppression of antiferromagnetic correlations by quenched dipole-type impurities". *The European Physical Journal B*, 8(4):511–523, 1999.

[132] B. J. Suh, P. C. Hammel, Y. Yoshinari, J. D. Thompson, J. L. Sarrao, and Z. Fisk. "Suppression of Antiferromagnetic Order by Light Hole Doping in $La_2Cu_{1-x}Li_xO_4$: A ^{139}La NQR Study". *Physical Review Letters*, 81(13):2791, 1998.

[133] X. F. Sun, Kouji Segawa, and Yoichi Ando. "Metal-to-Insulator Crossover in $YBa_2Cu_3O_{6+y}$ Probed by Low-Temperature Quasiparticle Heat Transport". *Physical Review Letters*, 93(10):107001, 2004.

[134] V. Juricic, L. Benfatto, A. O. Caldeira, and C. Morais Smith. "Dynamics of Topological Defects in a Spiral: A Scenario for the Spin-Glass Phase of Cuprates". *Physical Review Letters*, 92(13):137202, April 2004.

[135] V. Juricic, L. Benfatto, A. O. Caldeira, and C. Morais Smith. "Dissipative dynamics of topological defects in frustrated Heisenberg spin systems". *Physical Review B*, 71(6):064421, February 2005.

[136] J. Lorenzana and G. Seibold. "Metallic Mean-Field Stripes, Incommensurability, and Chemical Potential in Cuprates". *Phys. Rev. Lett.*, 89(13):136401, Sep 2002.

[137] D. M. Broun, W. A. Huttema, P. J. Turner, S. Ozcan, B. Morgan, Ruixing Liang, W. N. Hardy, and D. A. Bonn. "Superfluid Density in a Highly Underdoped $YBa_2Cu_3O_{6+y}$ Superconductor". *Physical Review Letters*, 99(23):237003–4, December 2007.

[138] J. B. Torrance, A. Bezinge, A. I. Nazzal, T. C. Huang, S. S. P. Parkin, D. T. Keane, S. J. LaPlaca, P. M. Horn, and G. A. Held. "Properties that change as superconductivity disappears at high-doping concentrations in $La_{2-x}Sr_xCuO_4$". *Physical Review B*, 40(13):8872, 1989.

[139] Subir Sachdev. "Colloquium: Order and quantum phase transitions in the cuprate superconductors". *Rev. Mod. Phys.*, 75(3):913–932, Jul 2003.

[140] C. Panagopoulos and V. Dobrosavljevic. "Self-generated electronic heterogeneity and quantum glassiness in the high-temperature superconductors". *Phys. Rev. B*, 72(1):014536, Jul 2005.

[141] A. N. Lavrov, Yoichi Ando, Seiki Komiya, and I. Tsukada. "Unusual Magnetic Susceptibility Anisotropy in Untwinned $La_{2-x}Sr_xCuO_4$ Single Crystals in the Lightly Doped Region". *Physical Review Letters*, 87(1):017007, 2001.

[142] I. RaiCevic, J. Jaroszynski, Dragana Popovic, C. Panagopoulos, and T. Sasagawa. "Evidence for Charge Glasslike Behavior in Lightly Doped $La_{2-x}Sr_xCuO_4$ at Low Temperatures". *Physical Review Letters*, 101(17):177004–4, October 2008.

[143] Yoichi Ando. "Implication of the Mott-limit violation in high-Tc cuprates". *Journal of Physics and Chemistry of Solids*, 69(12):3195–3198, December 2008.

[144] J. E. Sonier, S. A. Sabok-Sayr, F. D. Callaghan, C. V. Kaiser, V. Pacradouni, J. H. Brewer, S. L. Stubbs, W. N. Hardy, D. A. Bonn, R. Liang, and W. A. Atkinson. "Hole-doping dependence of the magnetic penetration depth and vortex core size in $YBa_2Cu_3O_y$: Evidence for stripe correlations near (1/8) hole doping". *Physical Review B*, 76(13):134518–11, October 2007.

[145] Boris I. Shraiman and Eric D. Siggia. "Spiral phase of a doped quantum antiferromagnet". *Physical Review Letters*, 62(13):1564, 1989.

[146] P. W. Anderson. "The Resonating Valence Bond State in La_2CuO_4 and Superconductivity". *Science*, 235(4793):1196–1198, 1987.

[147] F. Carmona B. Ropers and S. Flandrois. "Screening properties of superconducting random composites". *Physica C*, 204:72–72, 1995.

[148] C. Bernhard, Ch. Niedermayer, U. Binninger, A. Hofer, Ch. Wenger, J. L. Tallon, G. V. M. Williams, E. J. Ansaldo, J. I. Budnick, C. E. Stronach, D. R. Noakes, and M. A. Blankson-Mills. "Magnetic penetration depth and condensate density of cuprate high-Tc superconductors determined by muon-spin-rotation experiments". *Phys. Rev. B*, 52(14):10488–10498, Oct 1995.

[149] C. Bernhard, J. L. Tallon, Th. Blasius, A. Golnik, and Ch. Niedermayer. "Anomalous Peak in the Superconducting Condensate Density of Cuprate High-Tc Superconductors at a Unique Doping State". *Physical Review Letters*, 86(8):1614–1617, 2001.

[150] J. Blundell. "Spin-polarized muons in condensed matter physics". *Contemporary Physics*, 40:175–192, 1999.

[151] F. Carmona, B. Ropers, and S. Flandrois. "Phenomenological approach to the resistive transition of YBaCuO-Ag superconducting random composites". *Physica C*, 204:72–72, 1992.

[152] R.J. Cava, A.W. Hewat, E.A. Hewat, B. Batlogg, M. Marezio, K.M. Rabe, J.J. Krajewski, W.F. Peck Jr., and L.W. Rupp Jr. "Structural anomalies, oxygen ordering and superconductivity in oxygen deficient YBa_2Cu_3O7-δ". *Physica C*, 165:419–433, 1990.

[153] J. Chappert and R.I. Grynzpan. *"Muons and Pions in Materials Research"*. North-Holland Physics Publishing, Amsterdam, 1984.

[154] B. Dabrowski, Z. Wang, K. Rogacki, J. D. Jorgensen, R. L. Hitterman, J. L. Wagner, B. A. Hunter, P. G. Radaelli, and D. G. Hinks. "Dependence of Superconducting Transition Temperature on Doping and Structural Distortion of the CuO_2 Planes in $La_{2-x}M_xCuO_4$, (M = Nd, Ca, Sr)". *Physical Review Letters*, 76(8):1348, 1996.

[155] F. James and M. Roos. "MINUIT, a System for Function Minimization and Analysis of the Parameter Errors and Correlations". *Comput. Phys. Commun.*, page 343, 1975.

[156] T. A. Friedmann, M. W. Rabin, J. Giapintzakis, J. P. Rice, and D. M. Ginsberg. "Direct measurement of the anisotropy of the resistivity in the a-b plane of twin-free, single-crystal, superconducting $YBa_2Cu_3O_{7-\delta}$". *Phys. Rev. B*, 42(10):6217–6221, Oct 1990.

[157] G. Jenks, S.S. Sadeghiz, J.P. Wikswo Jr. *"Encyclopedia of Applied Physics: SQUIDS for non-destructive evaluation"*, volume 30. VCH Publishers, Inc, 1997.

[158] R. J. Gooding. "Skyrmion ground states in the presence of localizing potentials in weakly doped CuO_2 planes". *Physical Review Letters*, 66(17):2266, 1991.

[159] Application Software Group. "MINUIT, Function Minimization and Error Analysis". *MINUIT Reference Manual*, 1992.

[160] C. C. Homes, S. V. Dordevic, M. Strongin, D. A. Bonn, Ruixing Liang, W. N. Hardy, Seiki Komiya, Yoichi Ando, G. Yu, N. Kaneko, X. Zhao, M. Greven, D. N. Basov, and T. Timusk. "A universal scaling relation in high-temperature superconductors". *Nature*, 430(6999):539–541, July 2004.

[161] H.H. Klauss, W. Wagener, M. Hillberg, W. Kopmann, H. Walf, F. J. Litterst, M. Hucker, and B. Buchner. "From Antiferromagnetic Order to Static Magnetic Stripes: The Phase Diagram of $(La, Eu)_{2-x}Sr_xCuO_4$". *Physical Review Letters*, 85(21):4590–4593, 2000.

[162] P.P. Klug and L.E. Alexander. *"X-ray diffraction procedures for polycristalline and amorphous materials"*. John Wiley and Sons, secon edition, New York, 1974.

[163] W. L. McMillan. "Transition Temperature of Strong-Coupled Superconductors". *Phys. Rev.*, 167(2):331–344, Mar 1968.

[164] W. J. Padilla, Y. S. Lee, M. Dumm, G. Blumberg, S. Ono, Kouji Segawa, Seiki Komiya, Yoichi Ando, and D. N. Basov. "Constant effective mass across the phase diagram of high-Tc cuprates". *Phys. Rev. B*, 72(6):060511, Aug 2005.

[165] C. Phillips. *"Physics of High-T_C Superconductors"*. Academic Press, INC. London, 1989.

[166] R. DeRenzi in:. *"MUON SCIENCE: muons in Physics, Chemistry and Materials"*. SUSSP and Publications and Institute of Physics Publishing, University of Edinburgh, January 1999.

[167] J.L. Tallon C. Panagopulos S.H. Naquib, J.R. Cooper. "Temperature dependence of electrical resistivity of high-T_c cuprates from pseudogap to overdoped regions". *Physica C*, 387:365–372, 2003.

[168] R.D. Shannon. "Revised effective ionic radii and systematic studies of interatomic distances in halides and chalcogenides". *Acta Cryst*, A32:751–767, 1976.

[169] R. Vaglio, C. Attanasio, L. Maritato, and A. Ruosi. "Explanation of the resistance-peak anomaly in non homogeneous superconductors". *Phys. Rev. B*, 47(22):15302–15303, Jun 1993.

[170] M. Weber, A. Amato, F. N.Gygax, A. Schenck, H. Maletta, V.N Duginov, V. G. Grebinnik, A. B. Lazarev, V. G. Olshevsky, V. Yu. Pomjakushin, S. N. Shilov, V. A. Zhukov, B. F. Kirillov, A. V. Pirogov, A. N. Ponomarev, V. G. Storchak, S. Kapusta, and J. Bock. "Magnetic-flux distribution and the magnetic penetration depth in superconducting polycrystalline $Bi_2Sr_2Ca_{1-x}Y_xCu_2O_{8+\delta}$ and $Bi_{2-x}Pb_xSr_2CaCu_2O_{8+\delta}$". *Phys. Rev. B*, 48(17):13022–13036, Nov 1993.

Acknowledgements

I gratefully acknowledge Prof. Roberto DeRenzi and Dott. Samuele Sanna for support, confidence, humanity, scientific culture and dedication.

I gratefully acknowledge all of the following persons:

The Chemistry Department: F. Mezzadri, L. Righi and G. Calestani for support in XRD.

The IMEM-CNR Institute: T. Besagni, E.Giglioli and F.Licci for support in samples preparation.

The ISIS (RAL) muon facility: S. Giblin, J. Lord and A. Hillier for support in μSR experiments.

All of my friends: both Nerds and not Nerds.....is there anybody out there? :)

The most grateful acknowledgement is dedicated to my family, Maria and Mario.